Infrasound sources in geosciences

Jelle Assink

Royal Netherlands Meteorological Institute (KNMI)

R&D Seismology and Acoustics

Sources of Infrasound

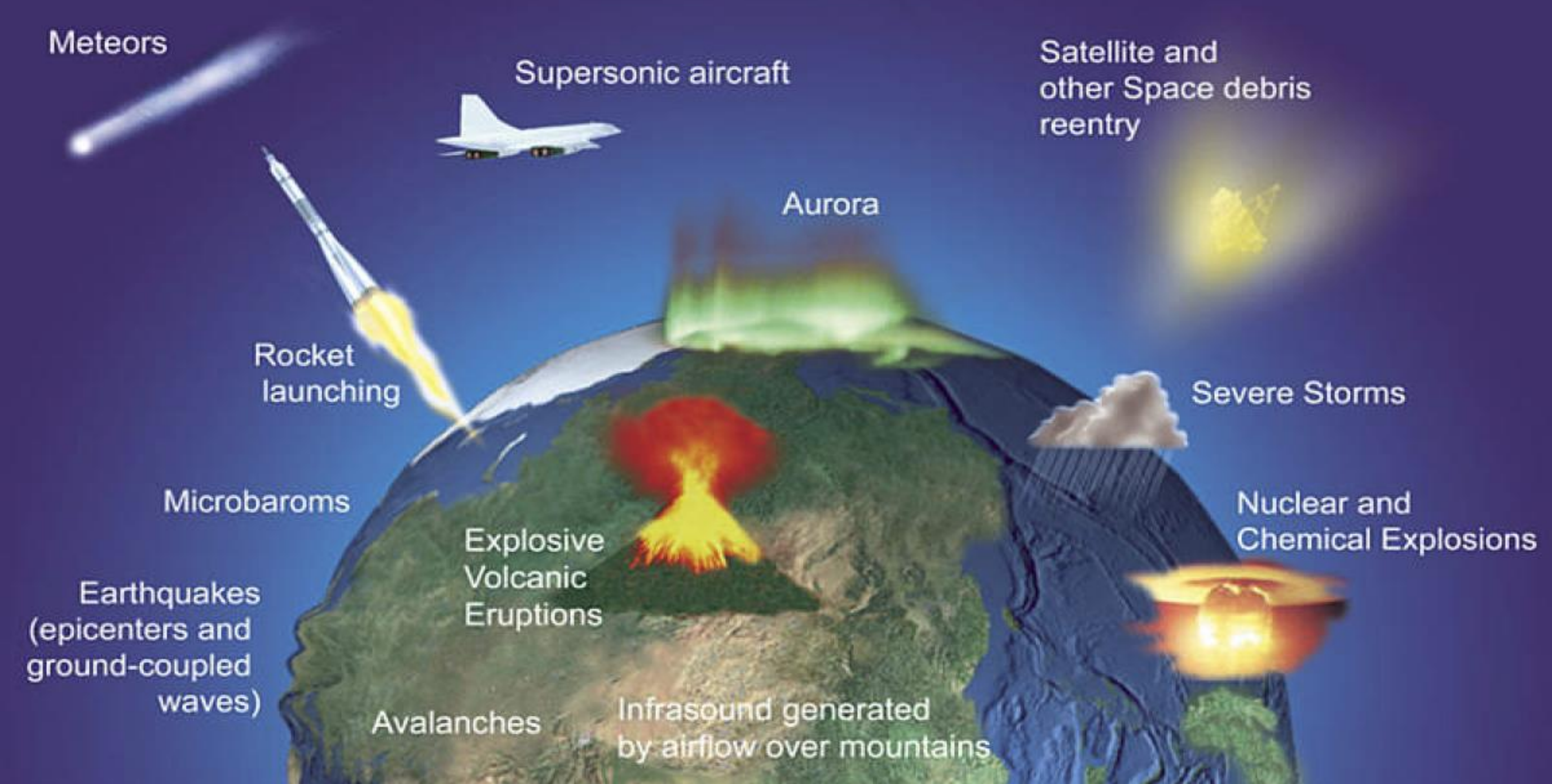

INTERNATIONAL MONITORING SYSTEM

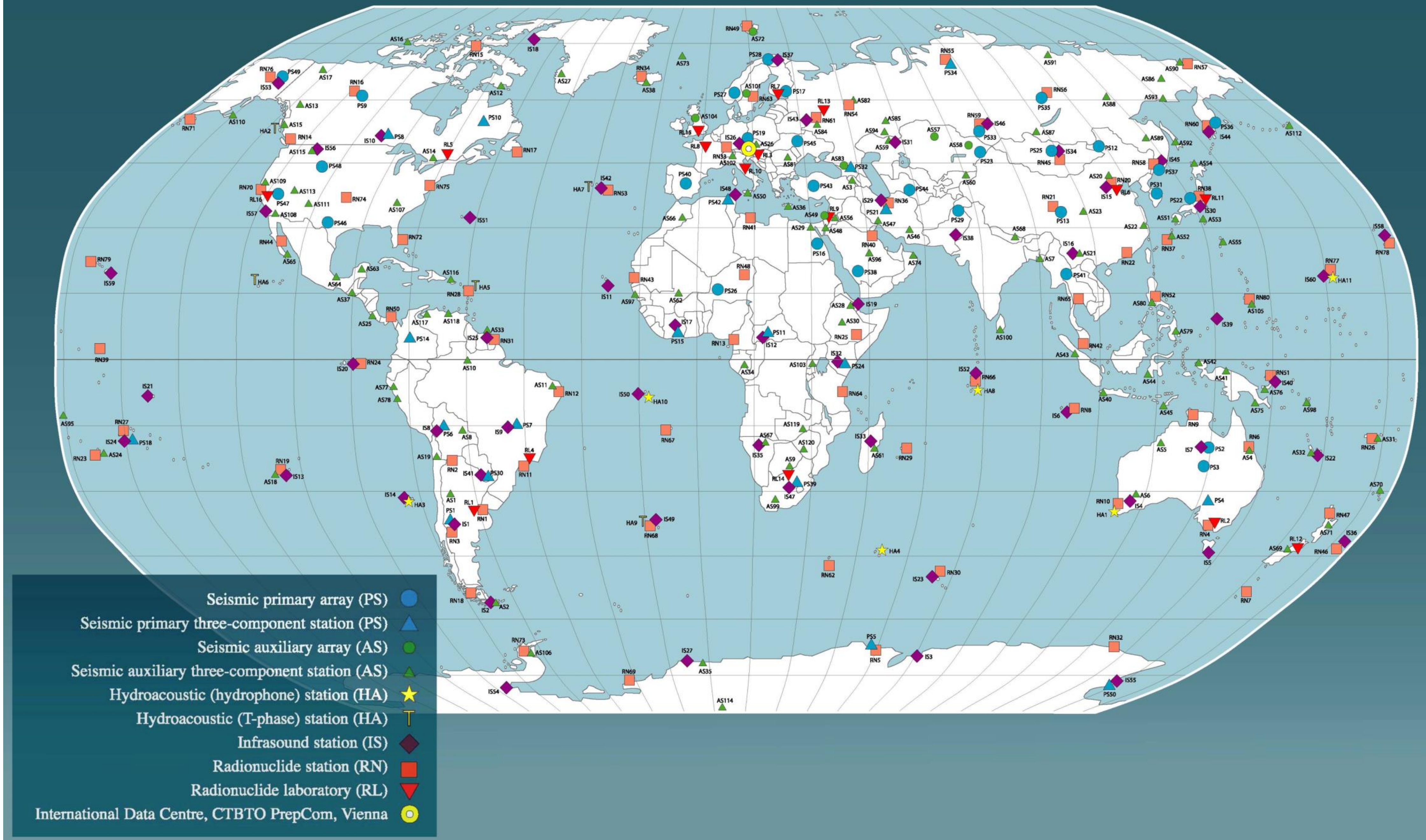

Global infrasound network

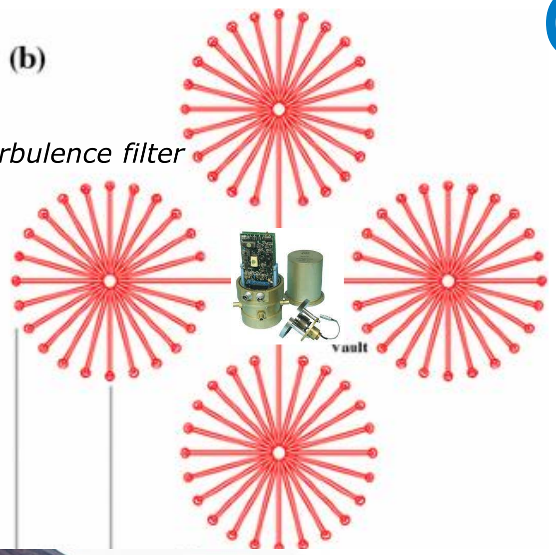

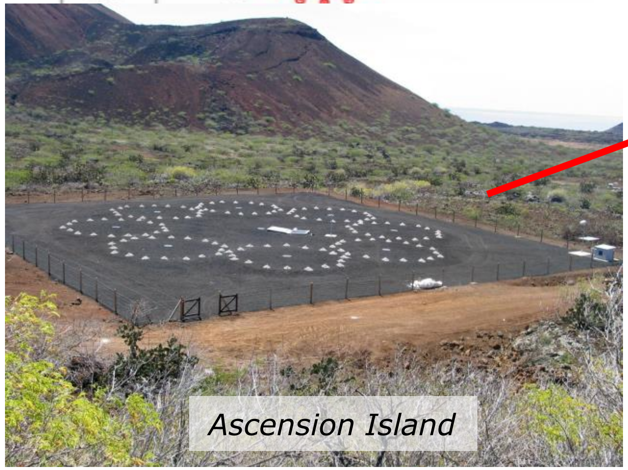

Ascension Island

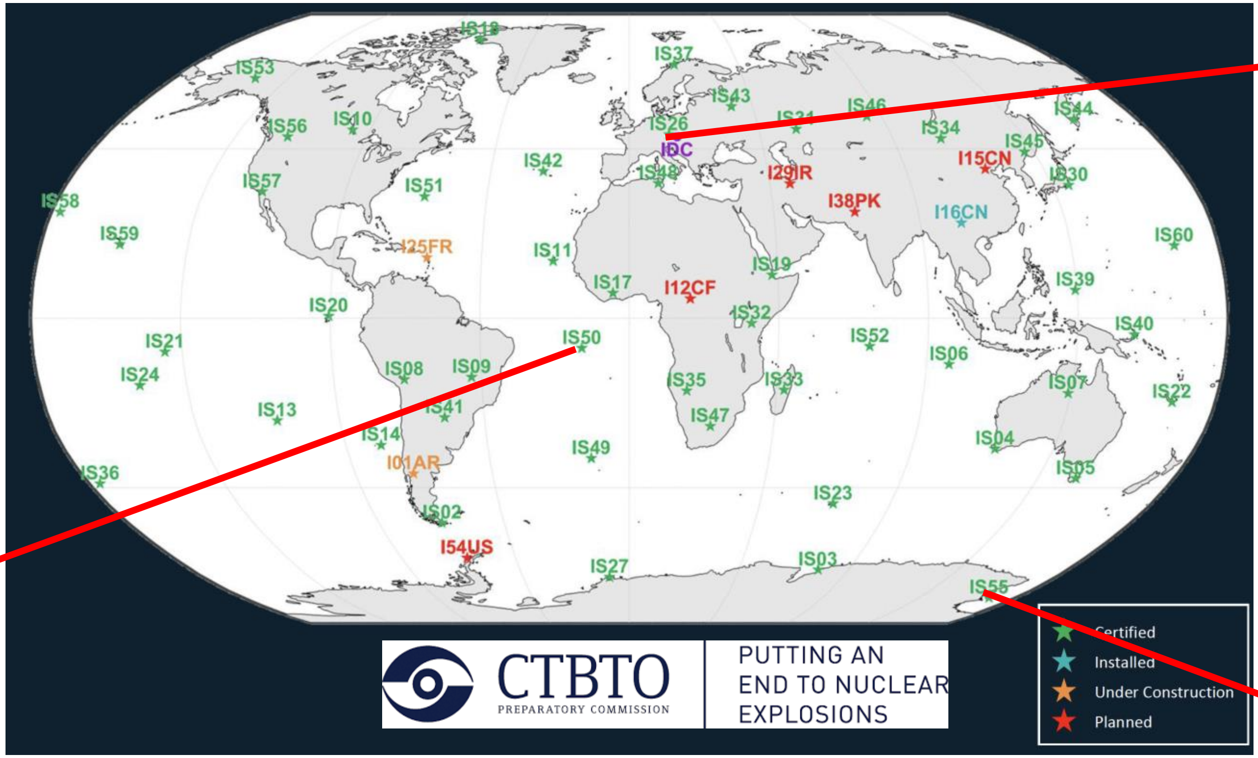

Bavaria, SE Germany

Windless Bight, Antarctica

Infrasound stations are deployed as multi-sensor stations (arrays) to be able to (1) detect coherent waves in a background of incoherent noise and (2) estimate the wavefront directivity

Towards a global, open-access infrasound network

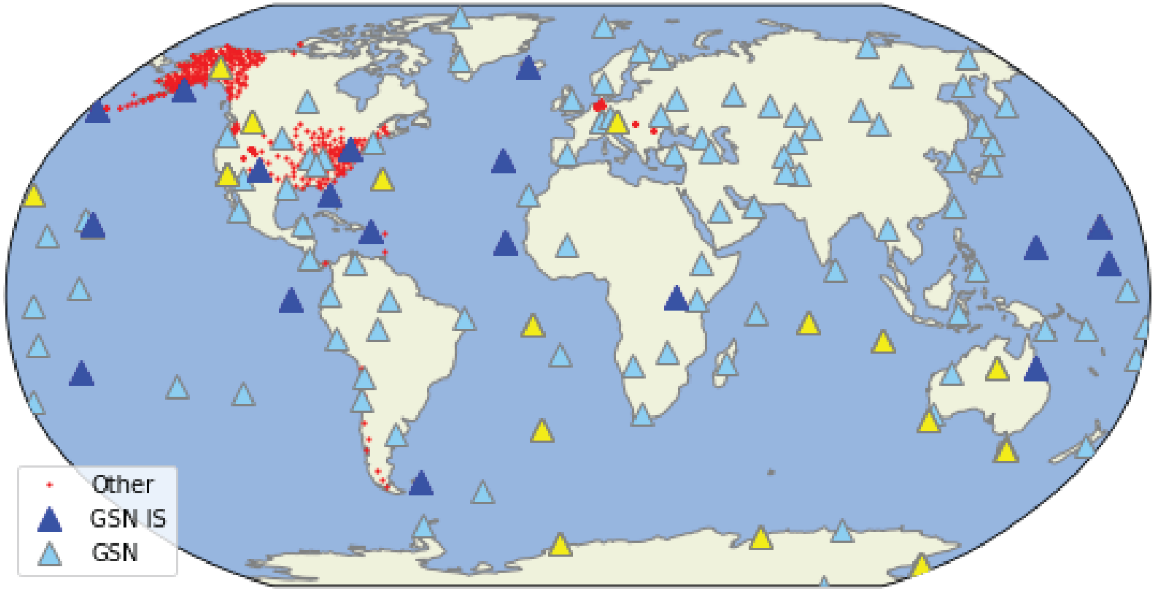

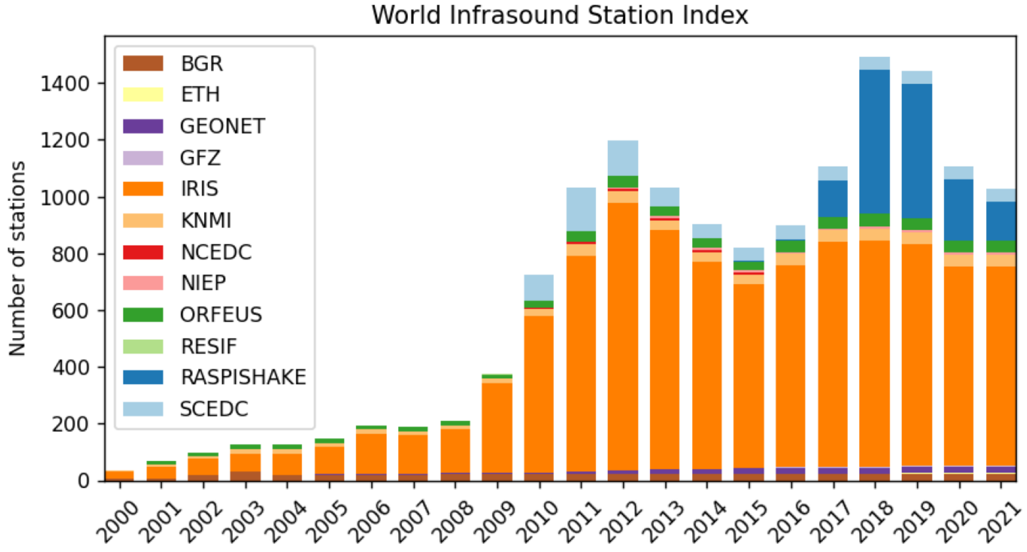

Arrowsmith et al., in prep.

- Some countries allow access to the data of the IMS infrasound arrays they operate, through FDSN webservices
- Some national facilities can be accessed through EIDA nodes
- A growing number of (single) infrasound sensors is installed as part of the Global Seismic Network (GSN)

Access through FDSN webservices and EIDAWSRoutingClient

```
In [1]: from obspy.clients.fdsn import RoutingClient
        from obspy.clients.fdsn import Client as fdsn_client
        from obspy import UTCDateTime

In [2]: #cl = RoutingClient('eida-routing')
        cl = fdsn_client('KNMI')

In [3]: t1 = UTCDateTime()
        t0 = t1 - 24*3600

        invselect = dict(network='*', station='*',
                         location='*', channel='*DF',
                         starttime=t0, endtime=t1)

        inv = cl.get_stations(**invselect, level='channel')

In [4]: print(inv)

        Inventory created at 2021-11-09T10:32:26.753412Z
                Sending institution: SeisComP3 (KNMI)
                Contains:
                        Networks (1):
                                NL
                        Stations (31):
                                NL.CIA01 (Cabauw Infrasound Array)
                                NL.CIA02 (Cabauw Infrasound Array)
                                NL.CIA03 (Cabauw Infrasound Array)
                                NL.CIA04 (Cabauw Infrasound Array)
                                NL.CIA05 (Cabauw Infrasound Array)
                                NL.CIA06 (Cabauw Infrasound Array)
                                NL.CIA07 (Cabauw Infrasound Array)
                                NL.CIA08 (Cabauw Infrasound Array)
                                NL.CIA09 (Cabauw Infrasound Array)
                                NL.CIA10 (Cabauw Infrasound Array)
                                NL.DBN01 (De Bilt Infrasound Array)
                                NL.DBN02 (De Bilt Infrasound Array)
                                NL.DBN03 (De Bilt Infrasound Array)
```

```
In [1]: from obspy.clients.fdsn import RoutingClient
        from obspy.clients.fdsn import Client as fdsn_client
        from obspy import UTCDateTime

In [2]: cl = RoutingClient('eida-routing')
        #cl = fdsn_client('KNMI')

In [3]: t1 = UTCDateTime()
        t0 = t1 - 24*3600

        invselect = dict(network='*', station='*',
                         location='*', channel='*DF',
                         starttime=t0, endtime=t1)

        inv = cl.get_stations(**invselect, level='channel')

In [4]: print(inv)

        Inventory created at 2021-11-09T10:33:58.861981Z
                Created by: ObsPy 1.2.2
                            https://www.obspy.org
                Sending institution: ObsPy FDSN Routing 1.2.2,SeisComP (BGR,GFZ,NIEP)
                Contains:
                        Networks (3):
                                GR, HN, RO
                        Stations (34):
                                GR.BFO (BGR Station GRSN Station Black Forest Observatory, Germany)
                                GR.HLGM1 (Helgoland AWI guest house microbarom)
                                GR.HLGM2 (Helgoland dune microbarom)
                                GR.I26H1 (BGR Station Infrasound Array CTBTO IS26, Germany)
                                GR.I26H2 (BGR Station Infrasound Array CTBTO IS26, Germany)
                                GR.I26H3 (BGR Station Infrasound Array CTBTO IS26, Germany)
                                GR.I26H4 (BGR Station Infrasound Array CTBTO IS26, Germany)
                                GR.I26H5 (BGR Station Infrasound Array CTBTO IS26, Germany)
                                GR.I26H6 (BGR Station Infrasound Array CTBTO IS26, Germany)
                                GR.I26H7 (BGR Station Infrasound Array CTBTO IS26, Germany)
                                GR.I26H8 (BGR Station Infrasound Array CTBTO IS26, Germany)
```

- Convenient access to data inventory and data is facilitated by scripting languages such as Python
- Infrasound data follows the Seed channel code '*DF' (D = Pressure, F = Infrasound).

Station response and waveform data

```
In [1]: from obspy.clients.fdsn import RoutingClient
        from obspy import UTCDateTime

In [2]: cl = RoutingClient('eida-routing')

In [3]: t0 = UTCDateTime('2022-01-15T18:00:00')
        t1 = t0 + 12*3600

In [4]: invselect = dict(network='GR', station='I26*',
                         location='*', channel='BDF',
                         starttime=t0, endtime=t1)
        inv = cl.get_stations(**invselect, level='response')

In [5]: st = cl.get_waveforms(**invselect)

In [6]: fig = inv[0][0][0].response.plot(1e-3, label=st[0].id)
```

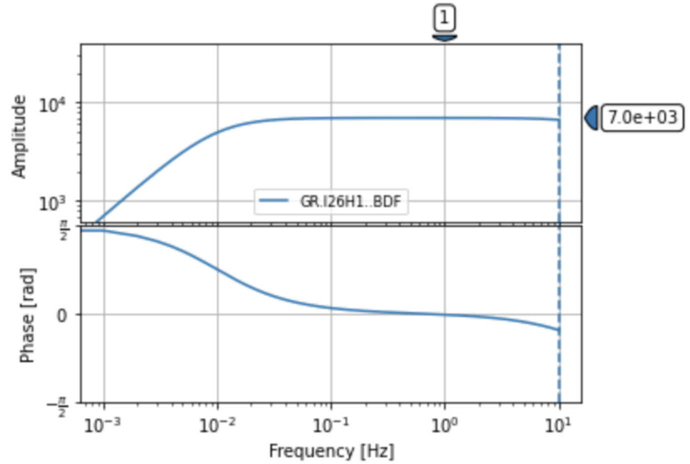

Infrasound array IS26, Bavaria, Germany

```
In [7]: st.attach_response(inv)
        fn = st[0].stats.sampling_rate / 2
        st.remove_response(pre_filt=[5e-5, 1e-4, 0.9*fn, 0.99*fn])

Out[7]: 8 Trace(s) in Stream:
        GR.I26H1..BDF | 2022-01-15T17:59:42.100000Z - 2022-01-16T06:00:13.050000Z | 20.0 Hz, 864620 samples
        GR.I26H2..BDF | 2022-01-15T17:59:46.200000Z - 2022-01-16T06:00:18.800000Z | 20.0 Hz, 864653 samples
        GR.I26H3..BDF | 2022-01-15T17:59:47.550000Z - 2022-01-16T06:00:11.800000Z | 20.0 Hz, 864486 samples
        GR.I26H4..BDF | 2022-01-15T17:59:45.000000Z - 2022-01-16T06:00:00.700000Z | 20.0 Hz, 864315 samples
        GR.I26H5..BDF | 2022-01-15T17:59:55.950000Z - 2022-01-16T06:00:05.500000Z | 20.0 Hz, 864192 samples
        GR.I26H6..BDF | 2022-01-15T17:59:58.750000Z - 2022-01-16T06:00:14.000000Z | 20.0 Hz, 864306 samples
        GR.I26H7..BDF | 2022-01-15T17:59:43.250000Z - 2022-01-16T06:00:06.200000Z | 20.0 Hz, 864460 samples
        GR.I26H8..BDF | 2022-01-15T17:59:46.650000Z - 2022-01-16T06:00:04.850000Z | 20.0 Hz, 864365 samples

In [11]: fig = st.plot()
```

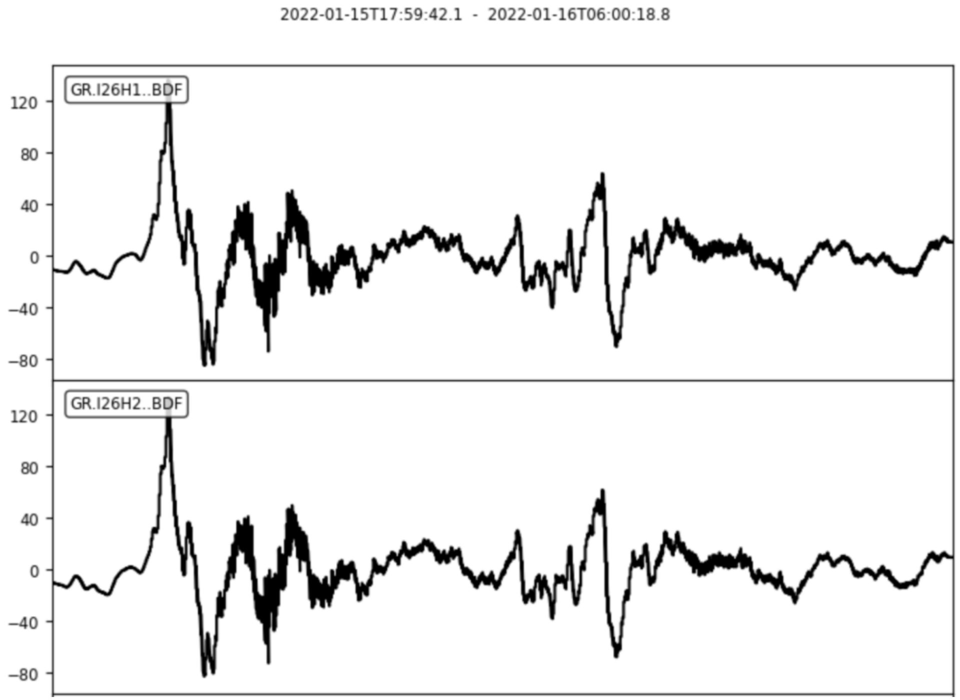

15 January 2022 Hunga Tonga eruption

National networks

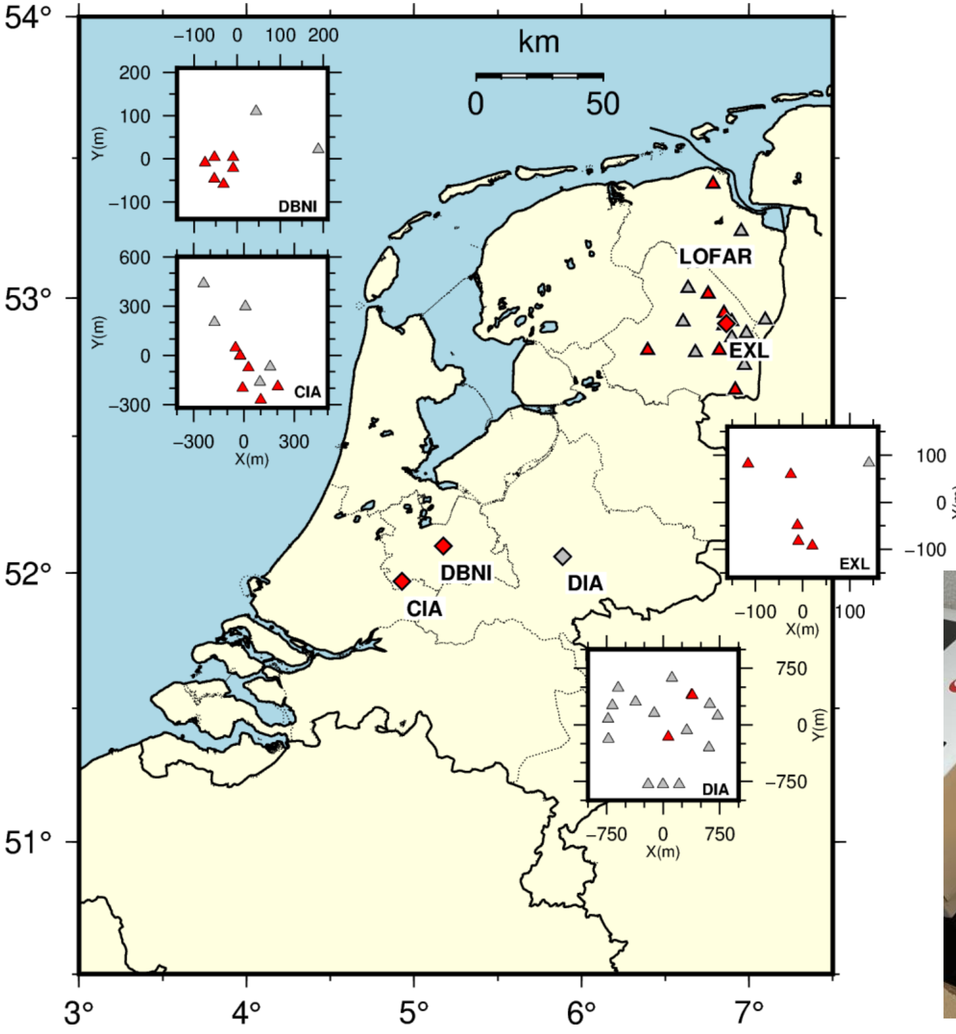

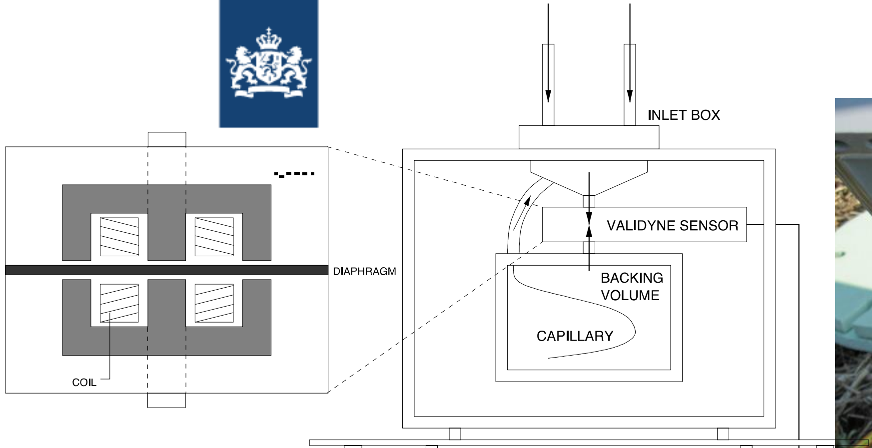

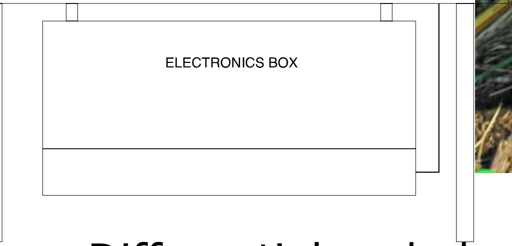

- Differential and absolute pressure sensors
- Initially self-developed by labs around the world
- These days also commercially available

Miniature / MEMS sensor technology is a recent trend

The boundary layer and infrasound detectability

- Boundary layer conditions determine the turbulence conditions near an infrasound microbarometer and therefore the detectability

- Turbulence-turbulence, turbulence-mean shear and stagnation pressure

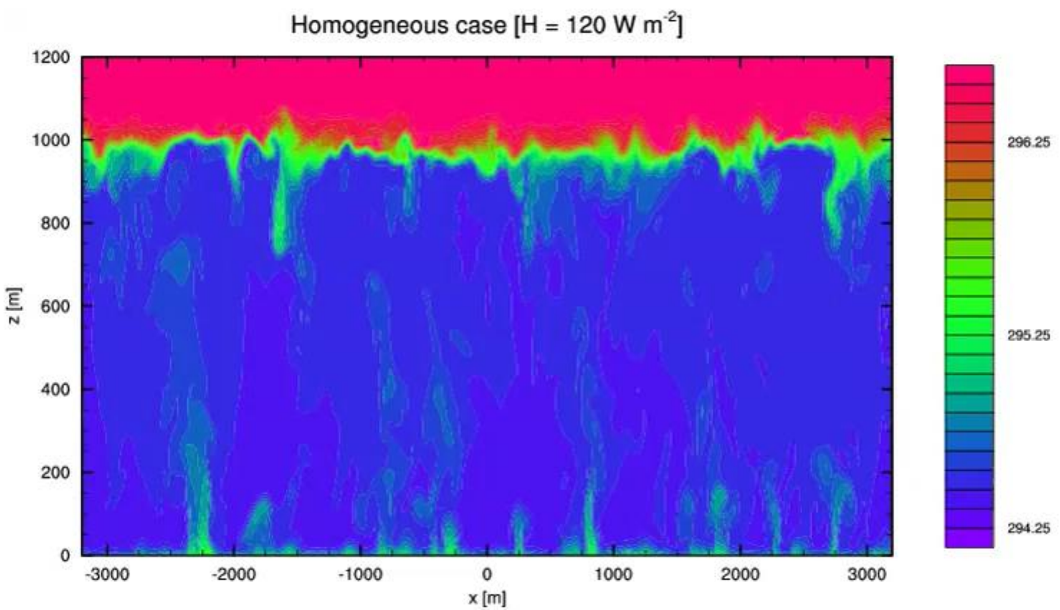

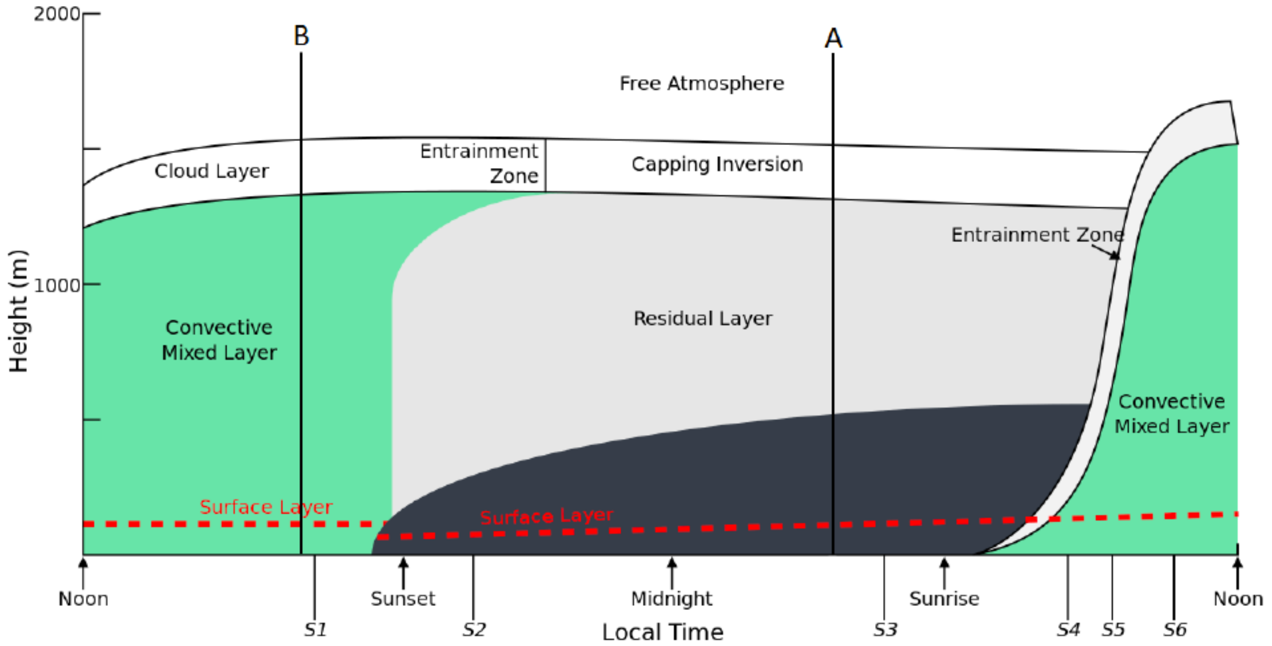

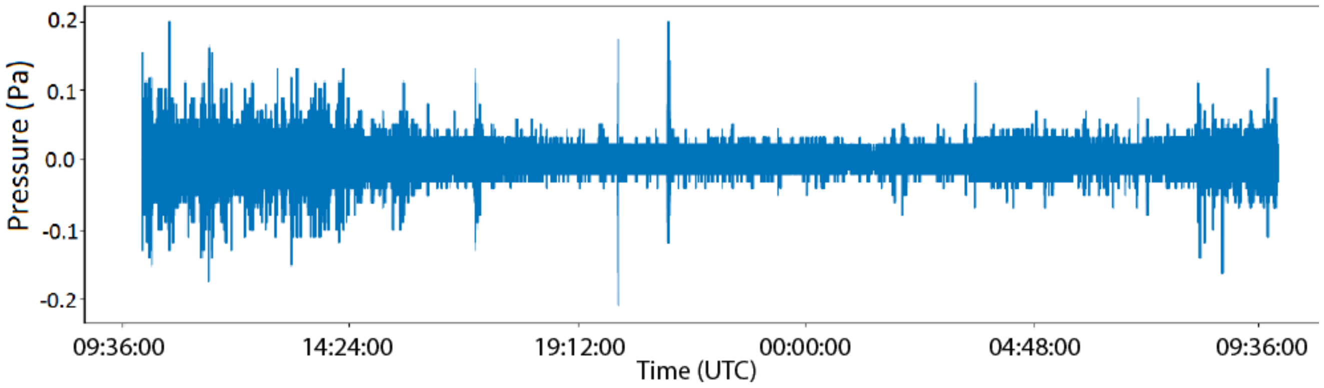

Measuring up to 200 m

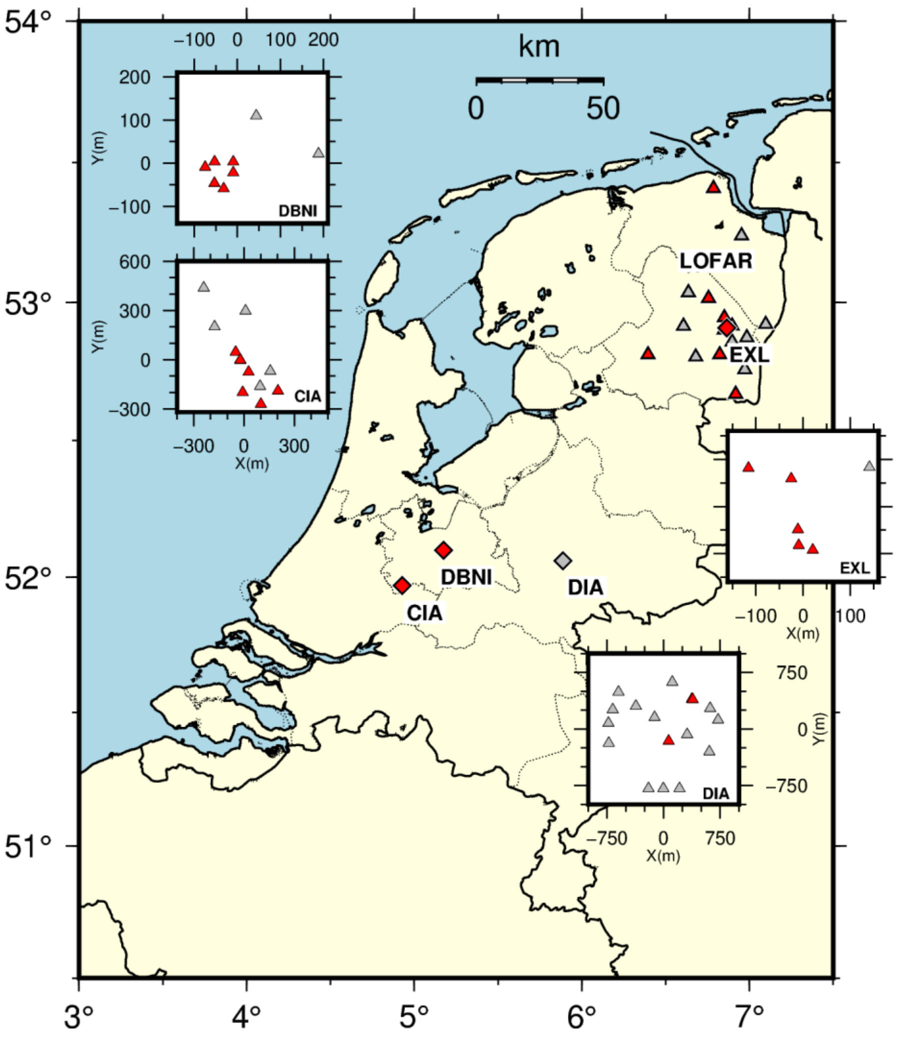

Tower

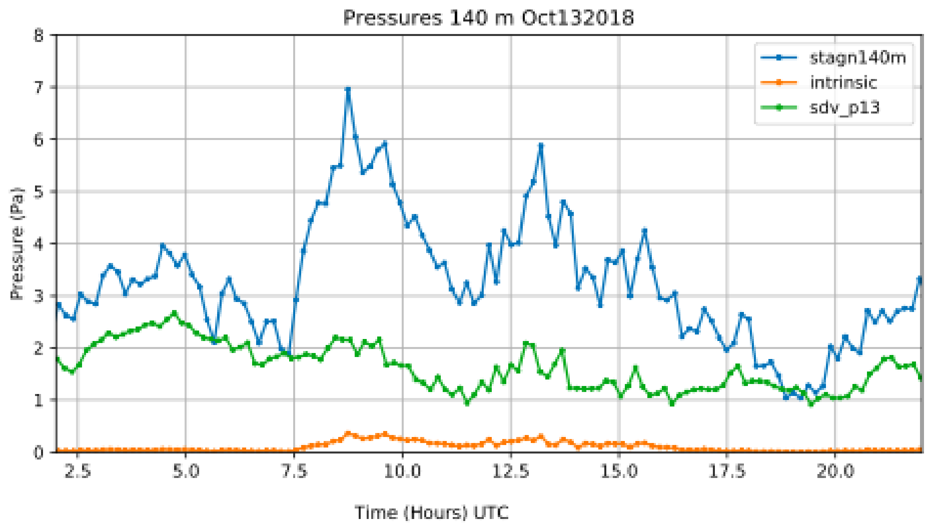

Ground

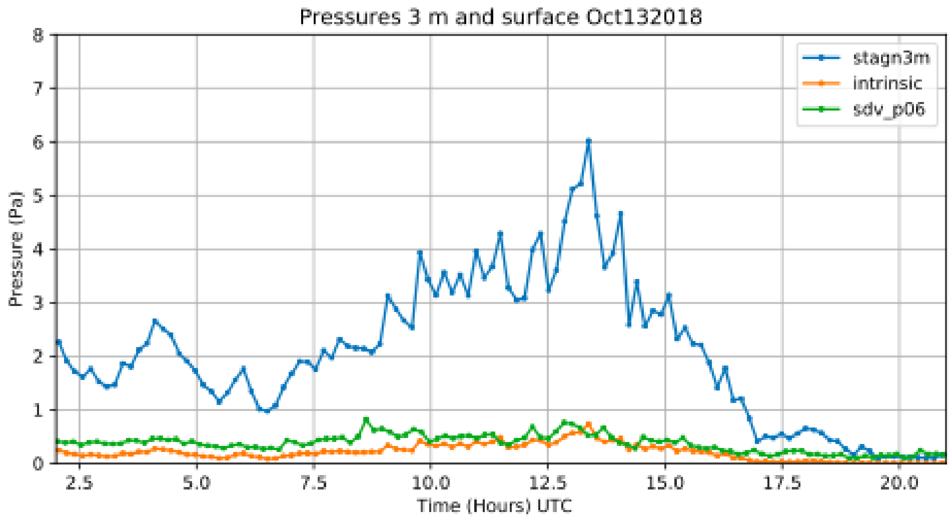

The boundary layer and infrasound detectability

- Estimating intrinsic pressure from turbulence pressure Poisson equation (e.g. George et al. 1984)

$$\frac{1}{\rho}\nabla^2 P_{\mathrm{intr}} = -\frac{\partial u_i \partial u_j}{\partial x_i \partial x_j}$$

Away from the surface, the standard deviation in intrinsic noise can be estimated:

$$\boxed{\sigma_{\mathrm{Pintr}} \approx \rho \sigma_u^2}$$

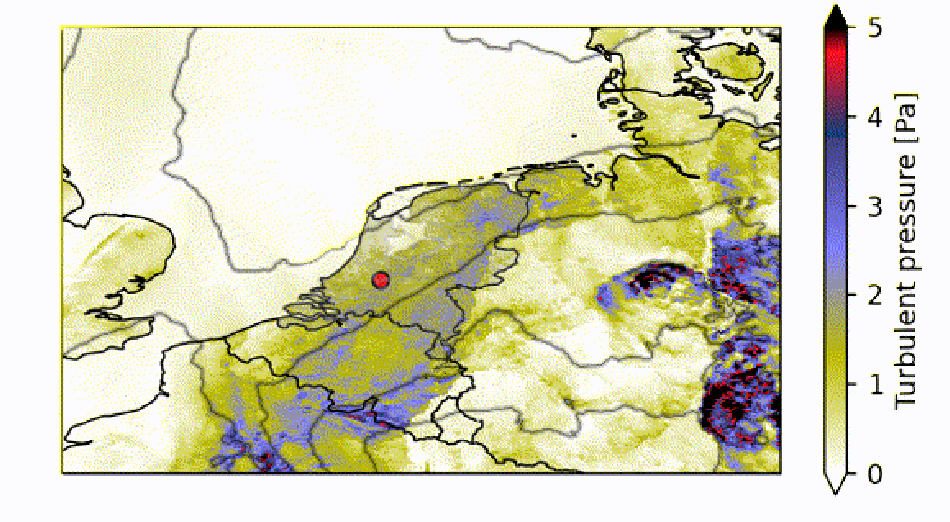

Smink et al., 2019

Observed (blue) and modeled (red) turbulence in the 0.05-5 Hz band

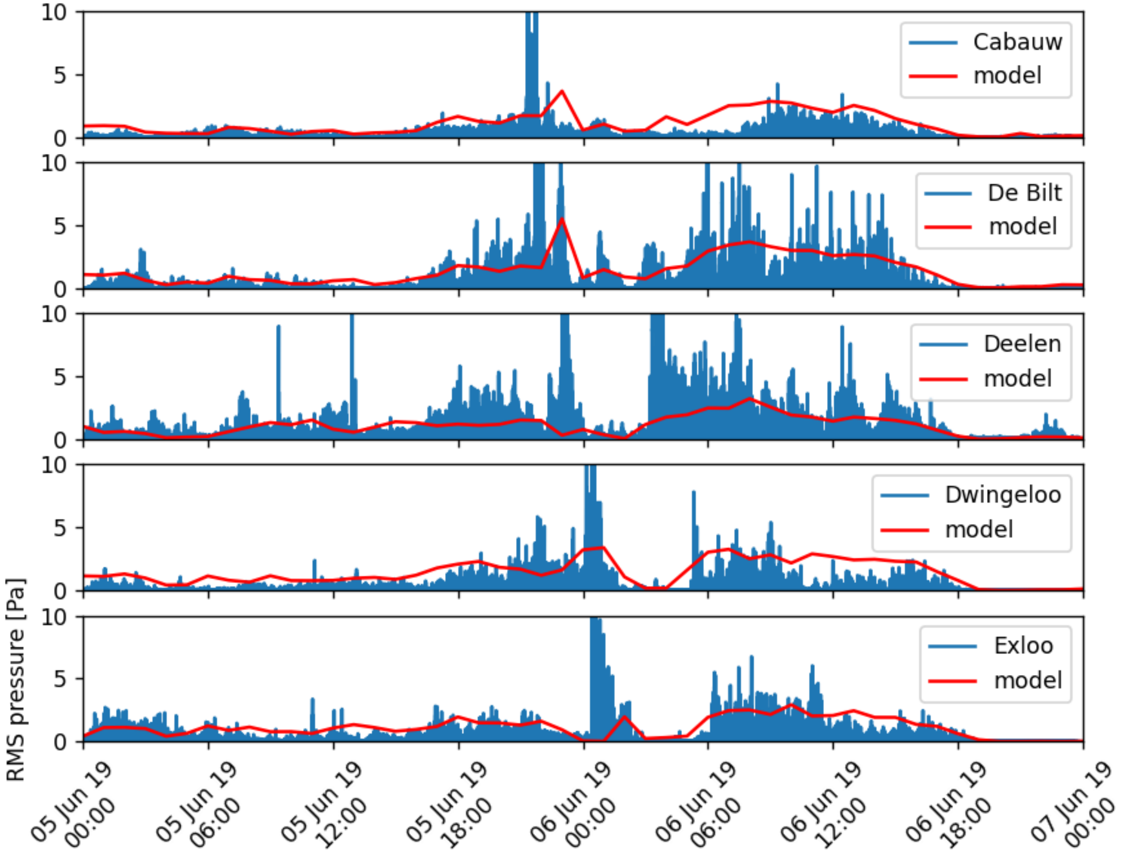

Wind screens

- Vault installation to ensure stable ambient conditions
- Wind noise can mask infrasound even at moderate wind speeds
- Porous hoses are currently used as wind screen / wind noise filter
  - + Cheap
  - + Effective at reducing wind noise by spatial averaging
  - - Easily damaged and response is affected by moisture
  - - Attenuates (infra)sound at higher frequencies
- Better solution: hemispherical domes
  - - Waveform fidelity is maintained
  - - Response does not change with time

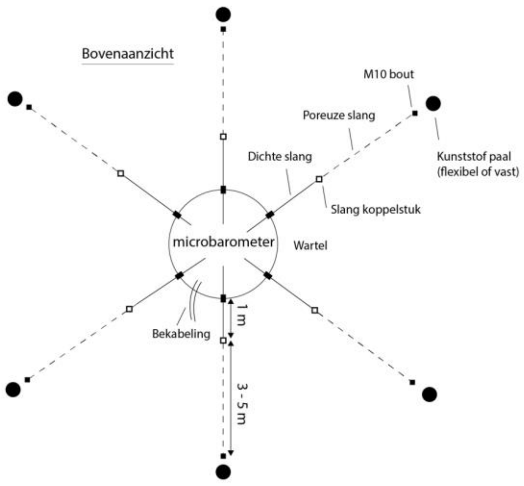

Two months of low-frequency sound measurements

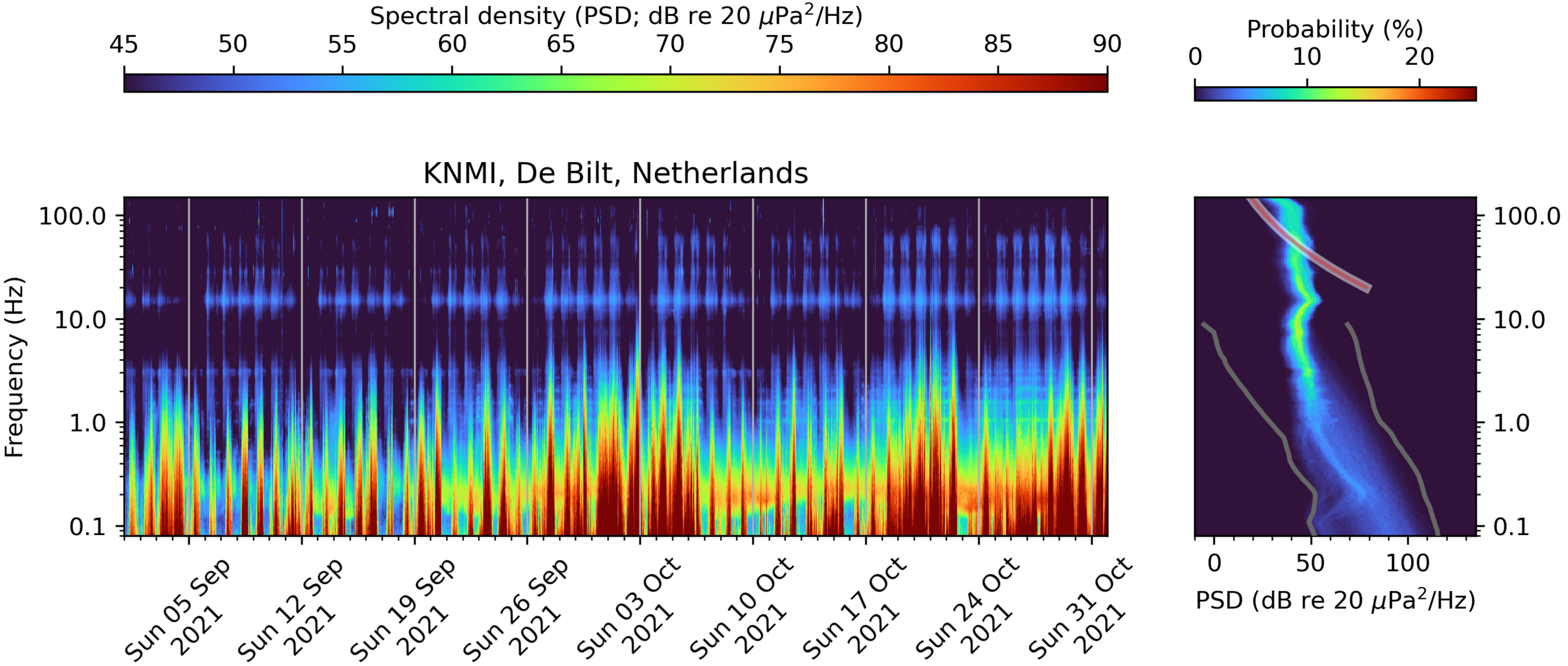

- Microbarom (atmospheric counterpart of microseism) visible around 0.2 Hz
- Vertical bands are wind noise bursts, mainly measured during the day
- Infrasound between 10-20 Hz is interpreted as road noise (day-night pattern; Sunday is quiet)

Sonic boom detection

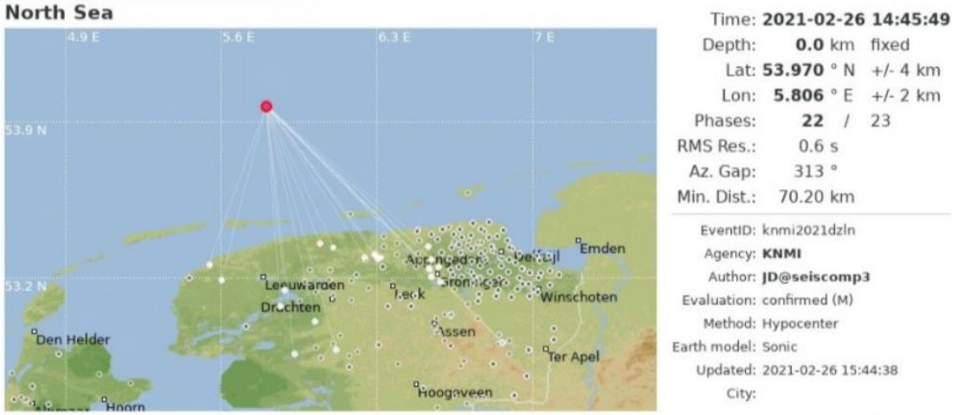

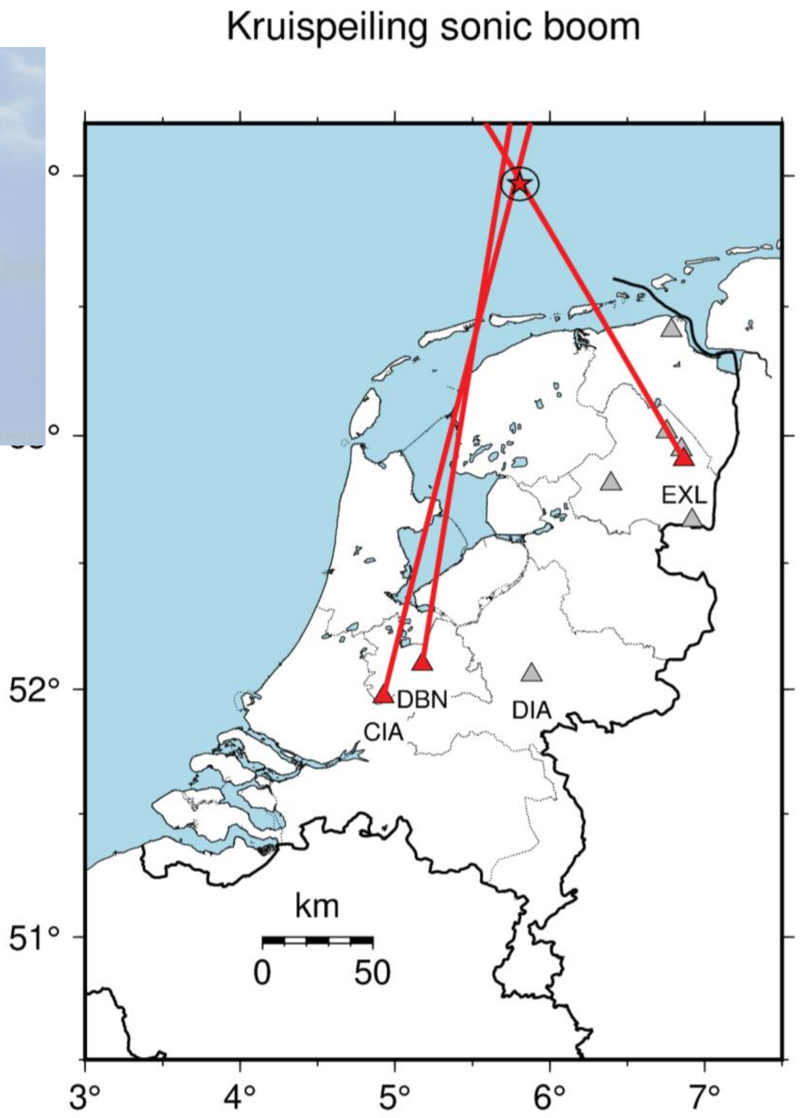

(1) Cross-bearing and (2) time-of-arrival localisation
Method 1 relies on infrasound arrays

Method 2 relies on detection on geophone network

Array processing for detection and parameter estimation

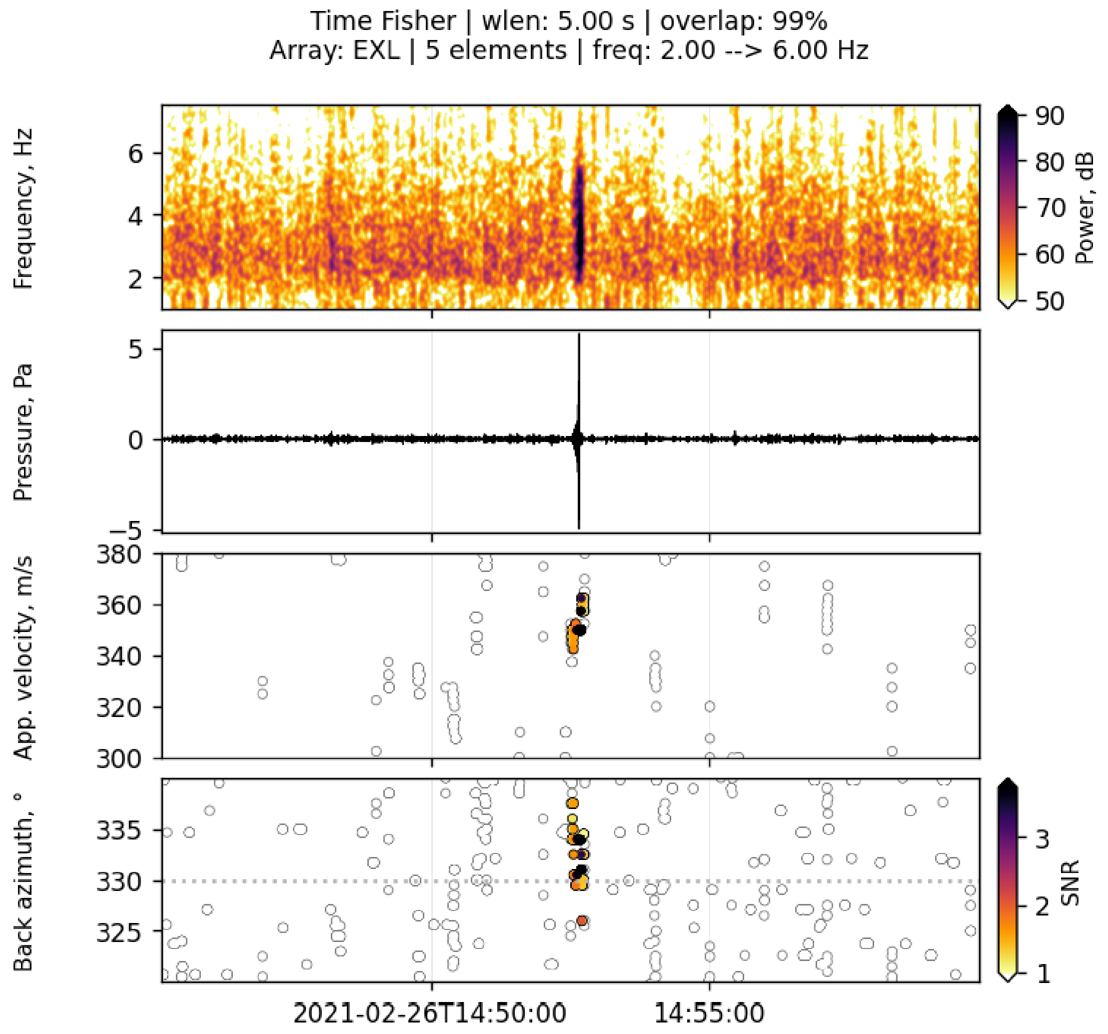

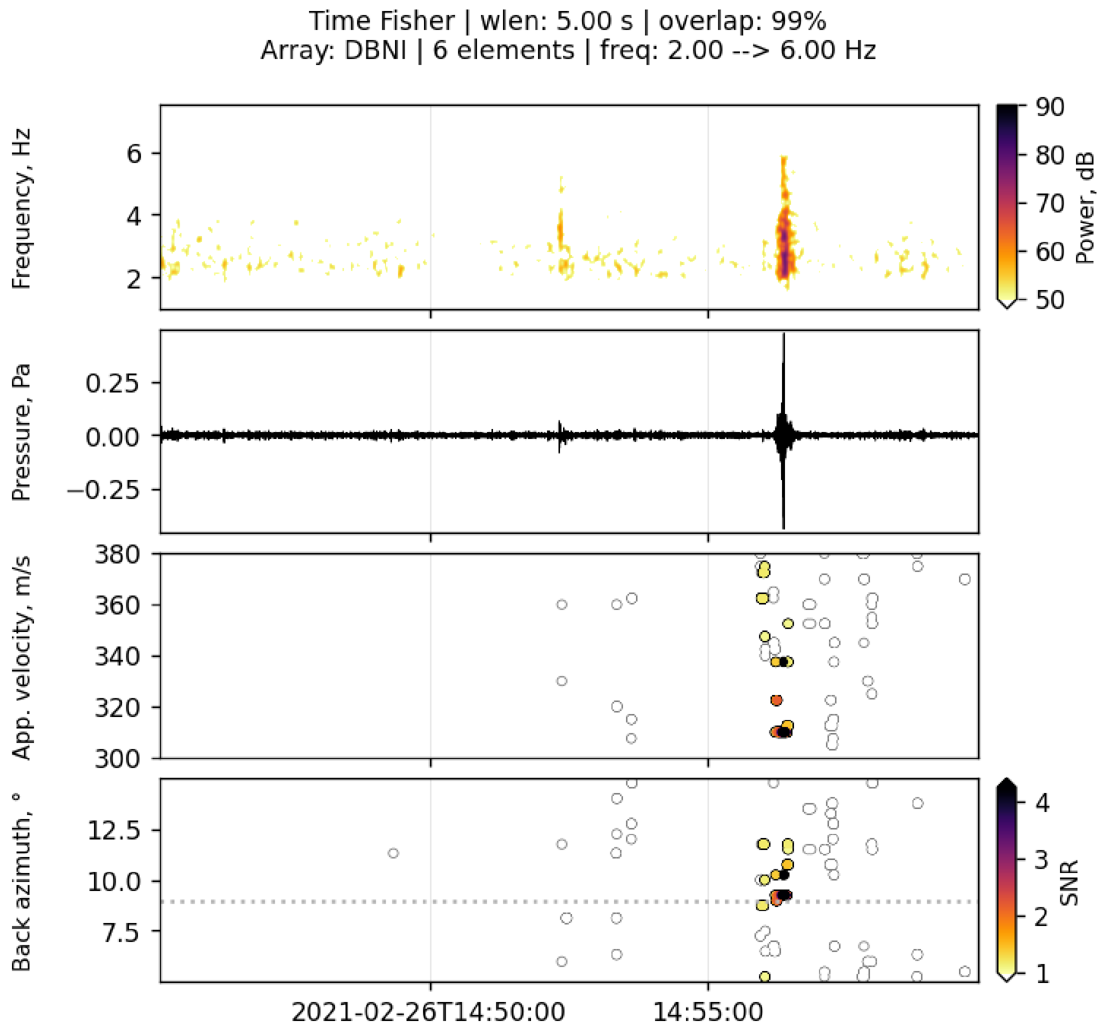

Seismo-acoustic coupling

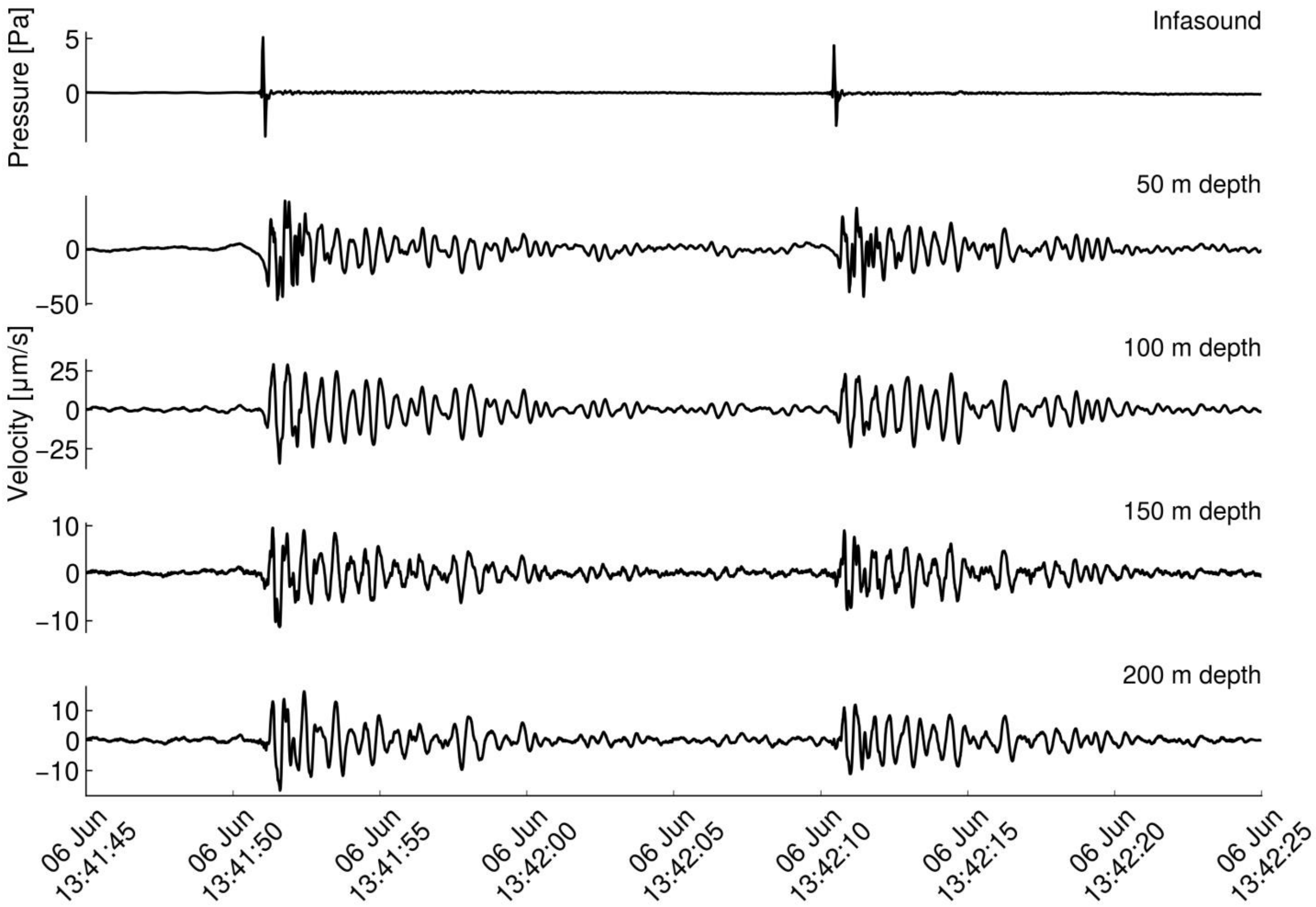

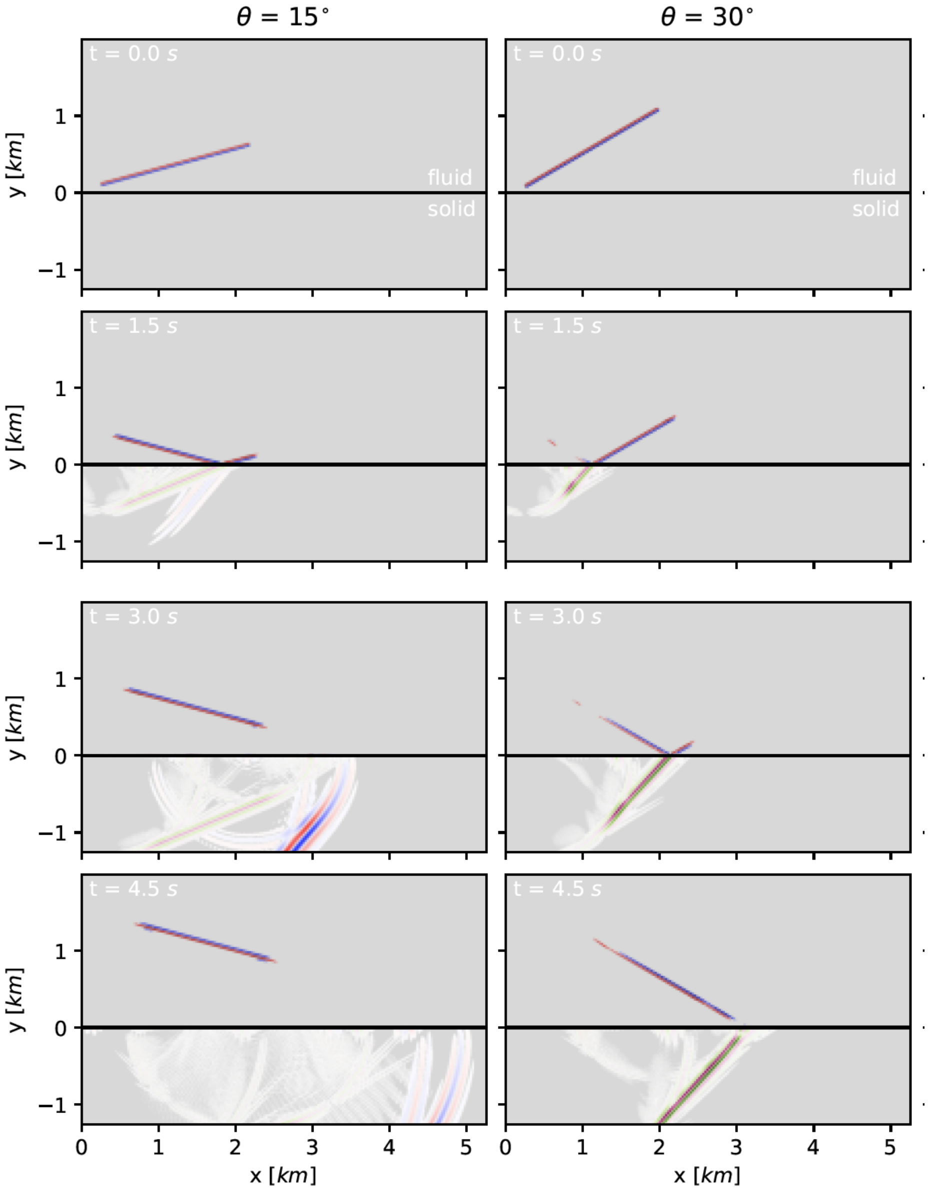

Numerical simulation of seismo-acoustic coupling for two plane waves at diff incidence angles

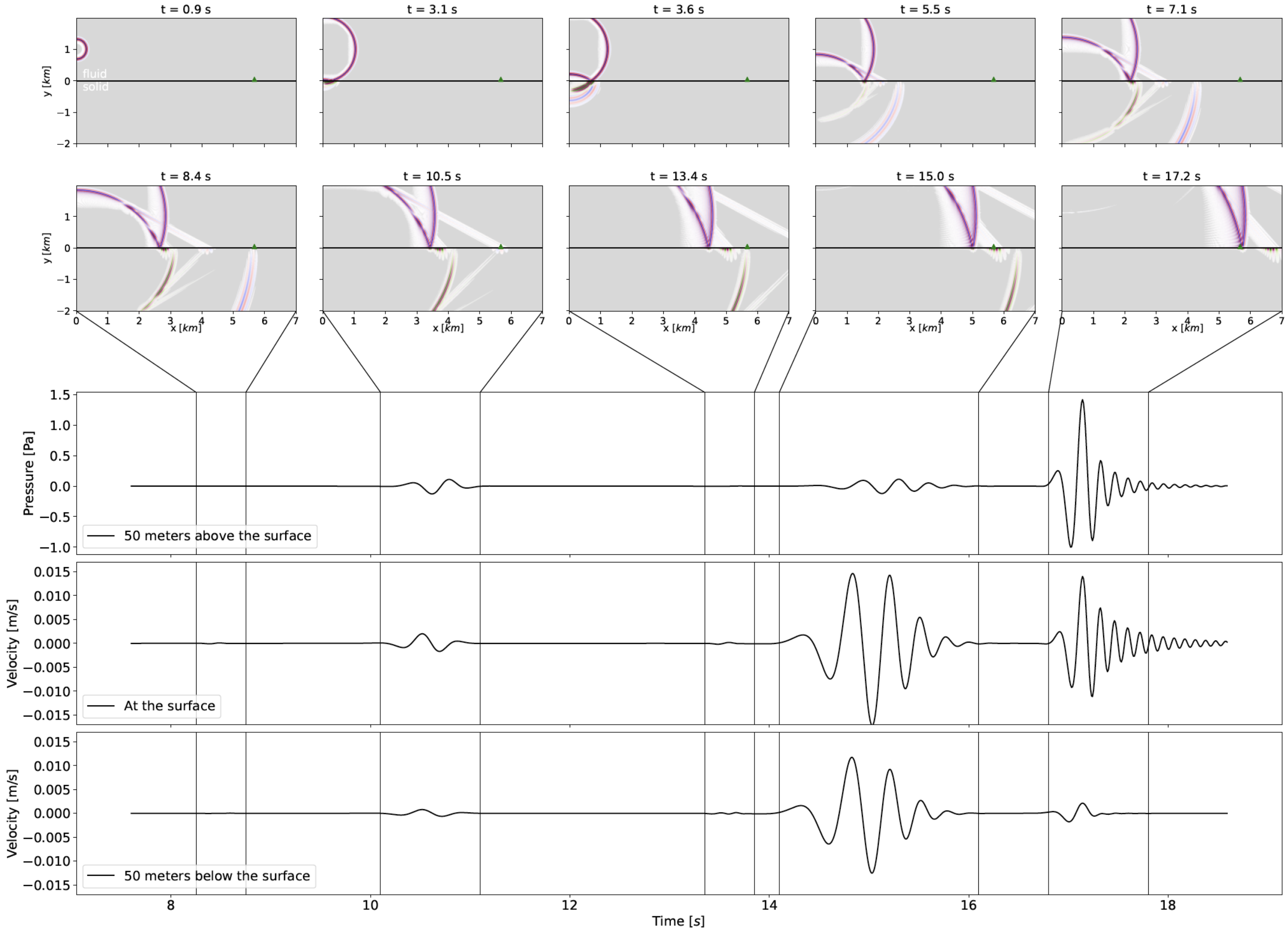

A simple two-layer solid-fluid simulation predicts seismic body waves, surface waves and direct acoustic arrivals

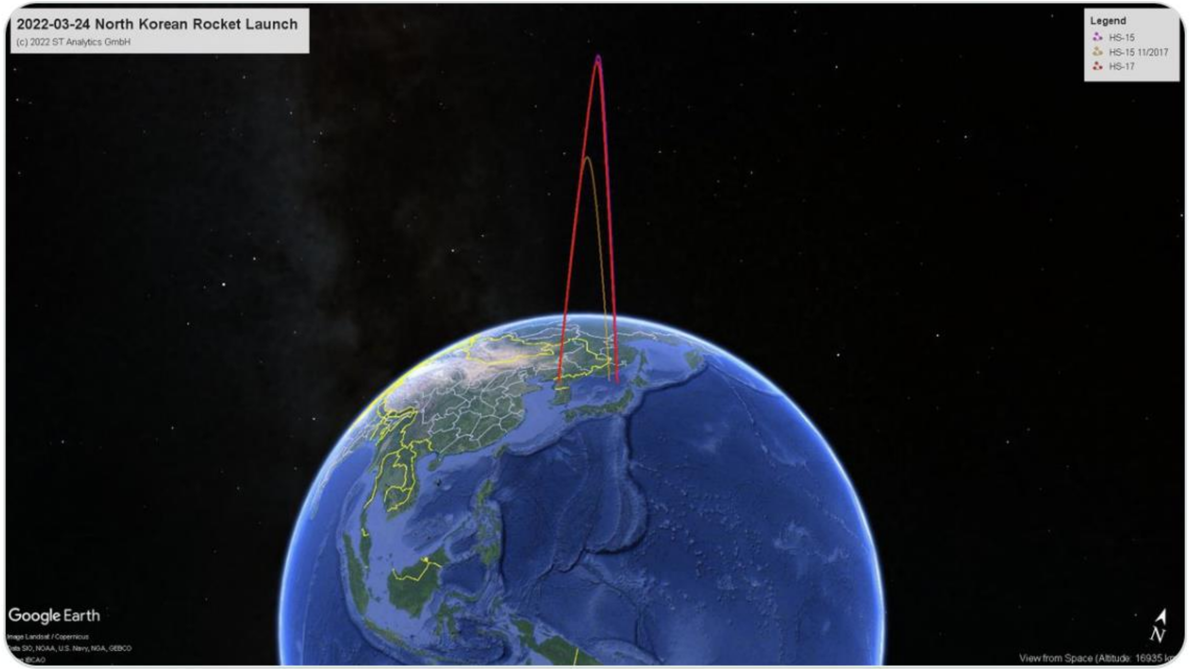

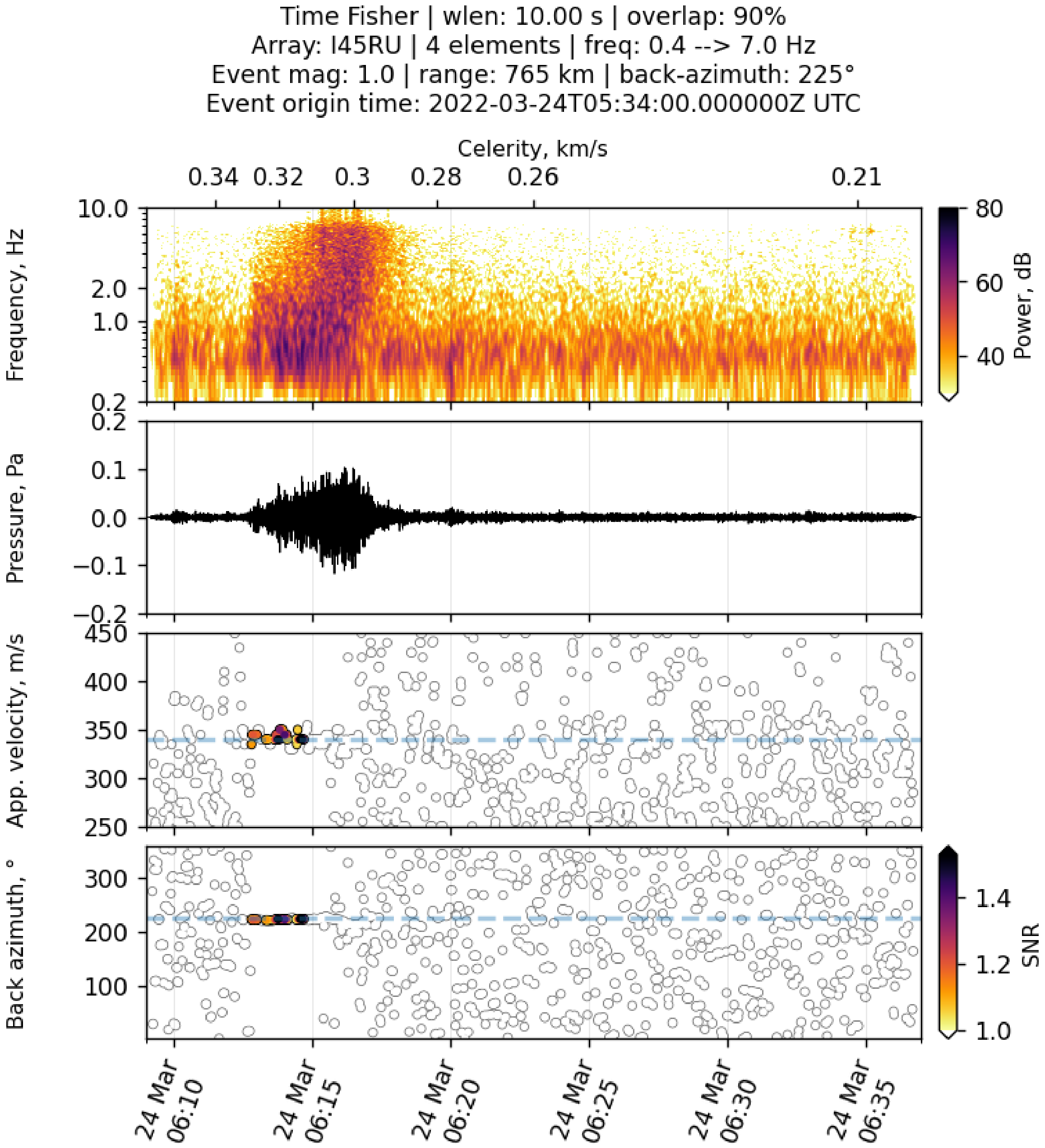

10:12 AM · Mar 24, 2022 · Twitter for iPhone

Markus Schiller
@RocketSchiller

Okay, so according to the recent Japanese MoD data, this is what #NorthKorea just launched a few hours ago (red). Peak is 6000+ km. For comparison, see the only Hwasong-15 ICBM test from November 2017 (orange). ISS orbit altitude currently is 408 km.

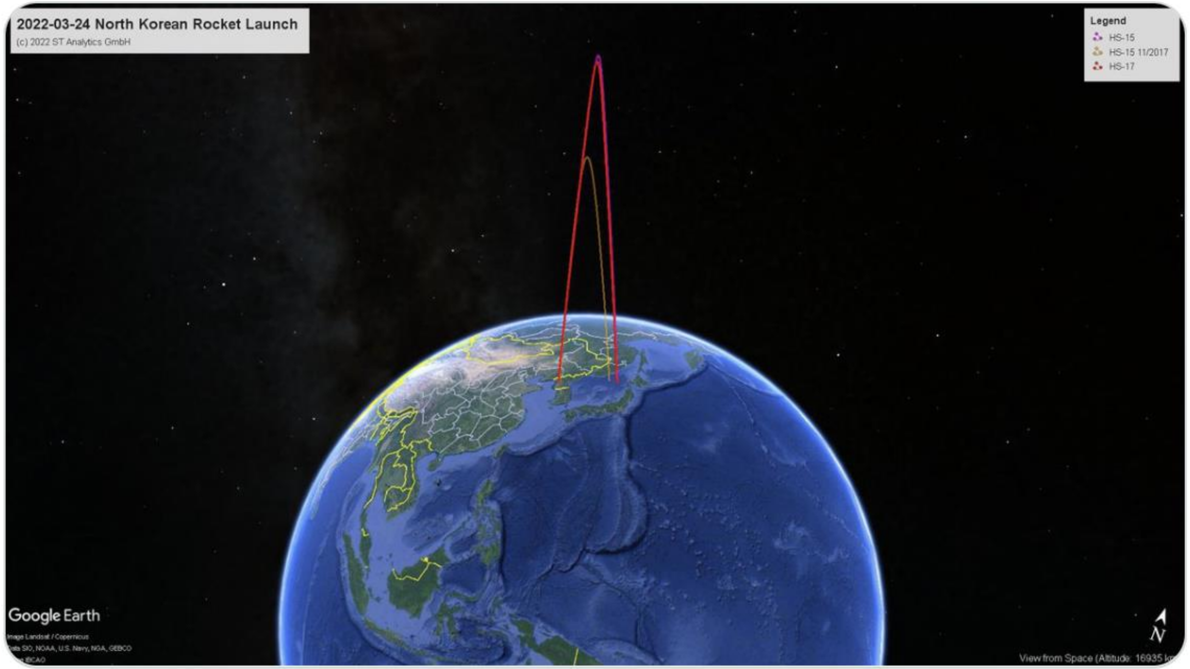

10:12 AM · Mar 24, 2022 · Twitter for iPhone

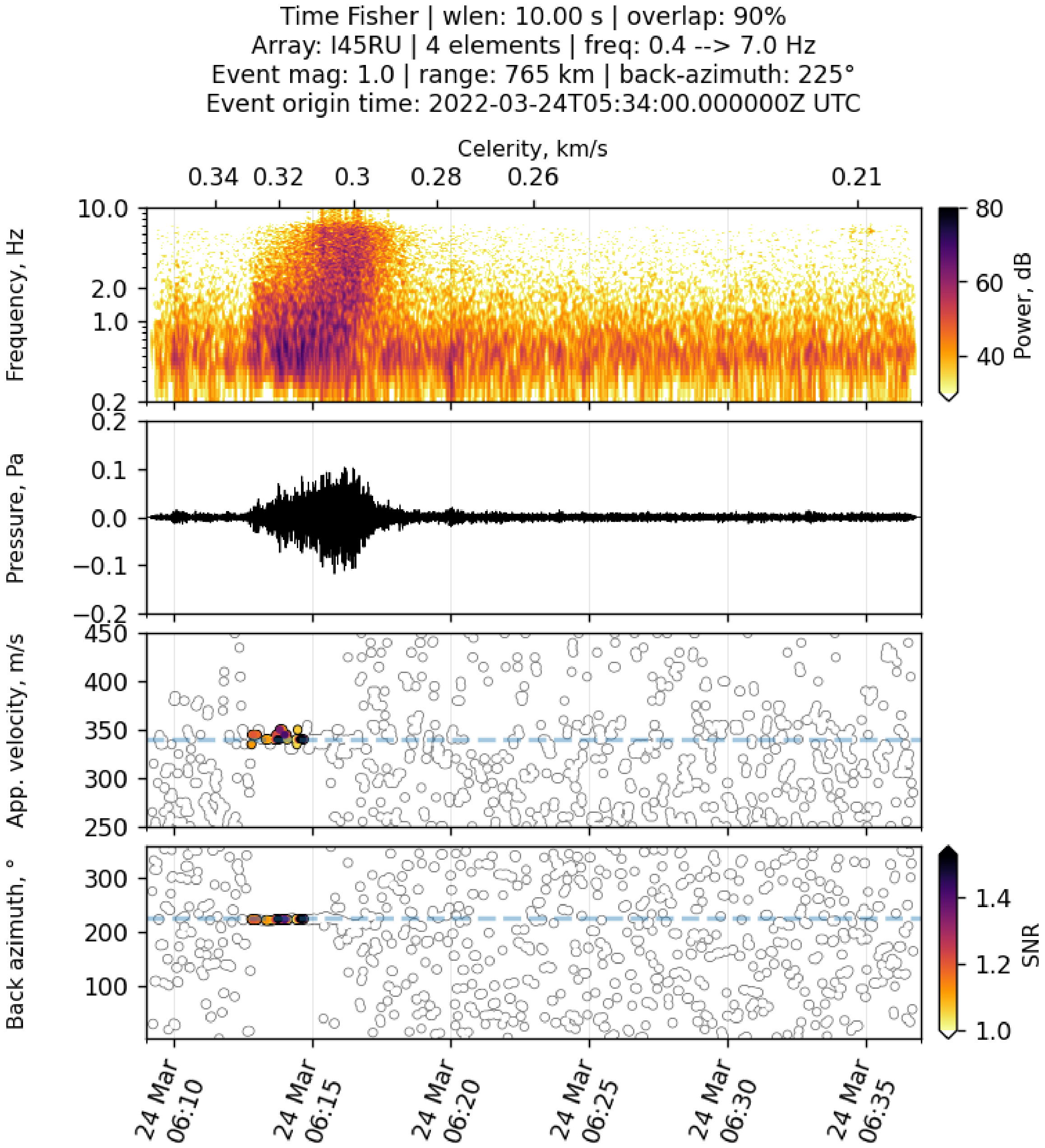

Markus Schiller
@RocketSchiller

Okay, so according to the recent Japanese MoD data, this is what #NorthKorea just launched a few hours ago (red). Peak is 6000+ km. For comparison, see the only Hwasong-15 ICBM test from November 2017 (orange). ISS orbit altitude currently is 408 km.

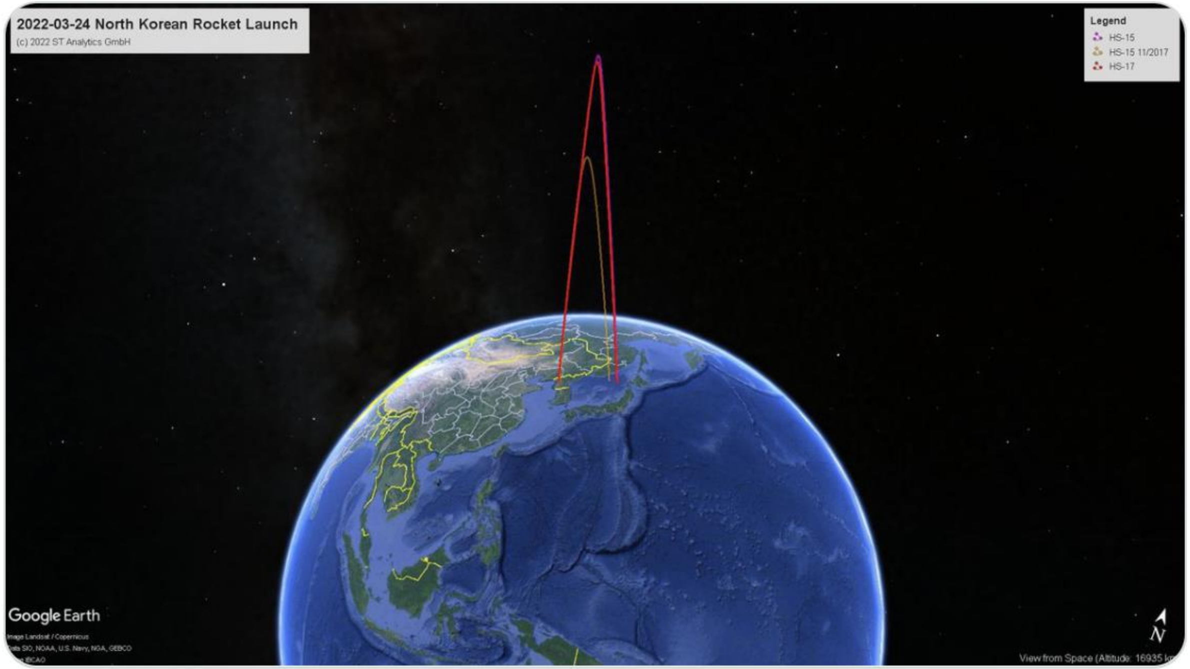

10:12 AM · Mar 24, 2022 · Twitter for iPhone

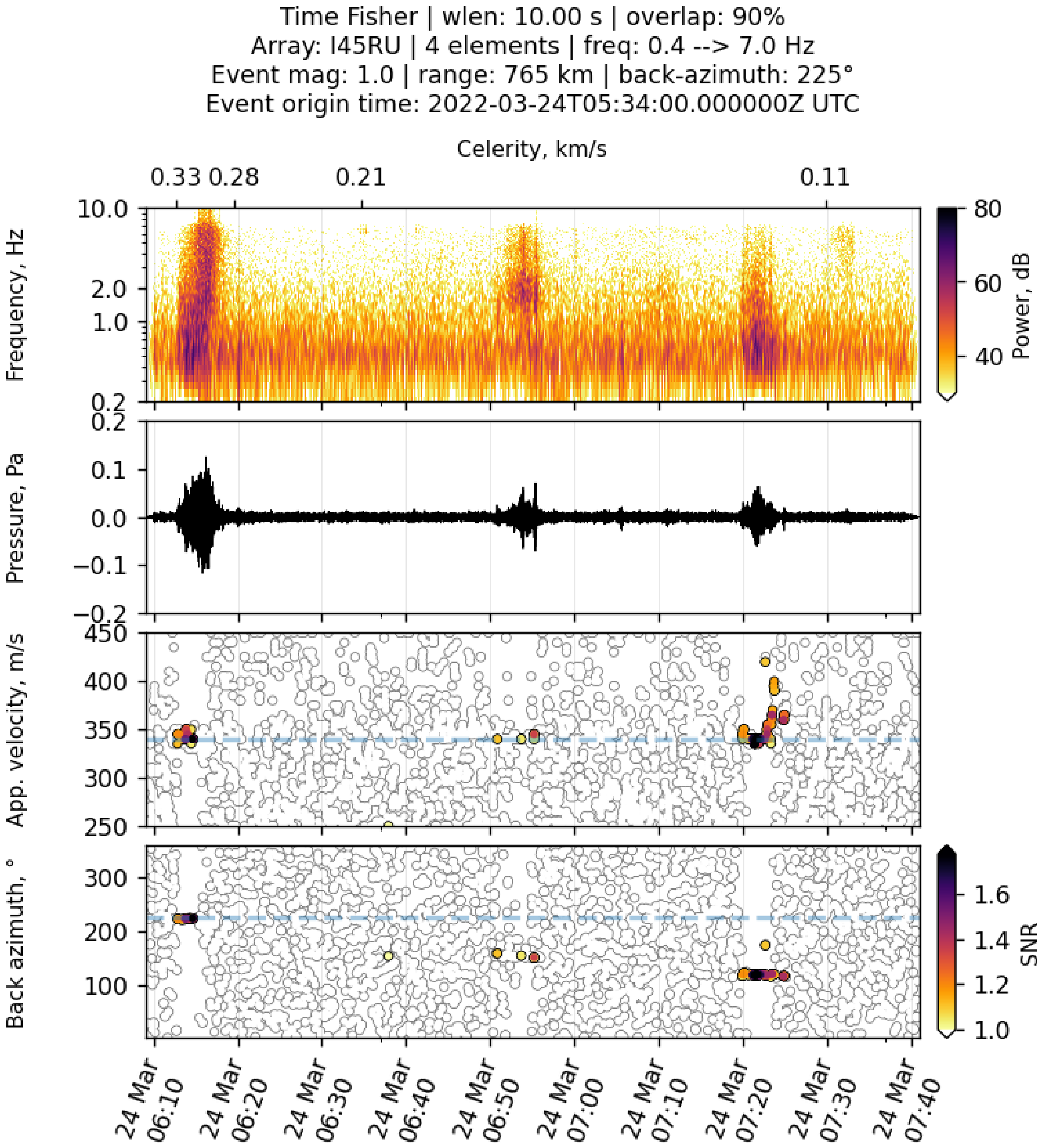

Markus Schiller
@RocketSchiller

Okay, so according to the recent Japanese MoD data, this is what #NorthKorea just launched a few hours ago (red). Peak is 6000+ km. For comparison, see the only Hwasong-15 ICBM test from November 2017 (orange). ISS orbit altitude currently is 408 km.

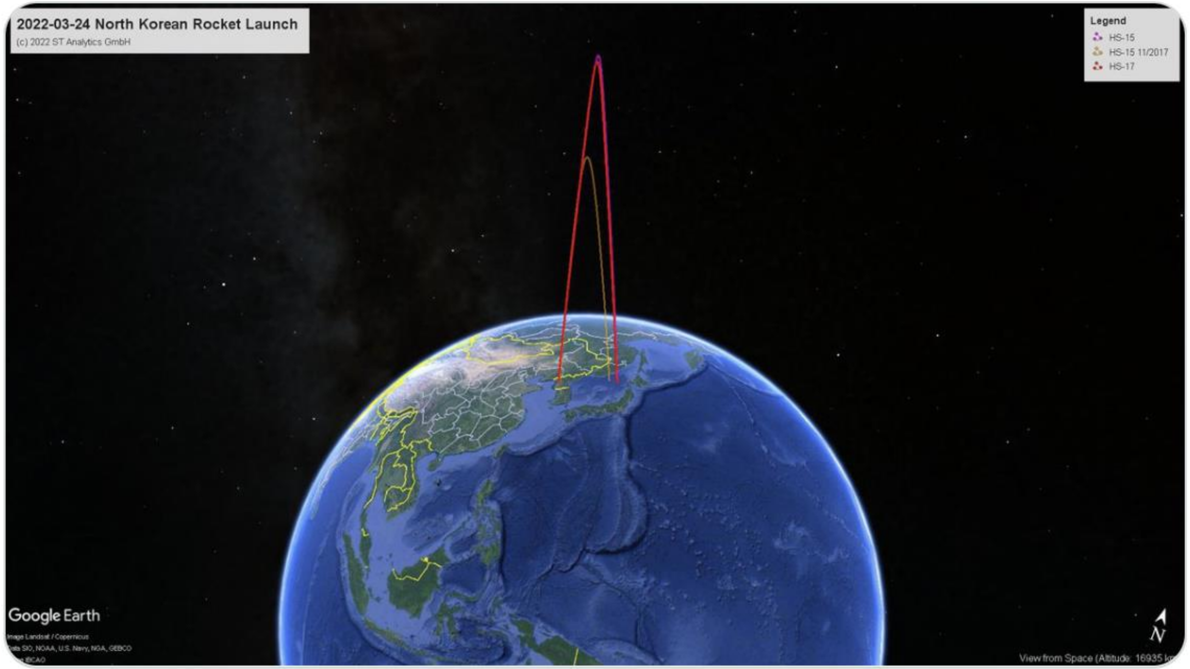

10:12 AM · Mar 24, 2022 · Twitter for iPhone

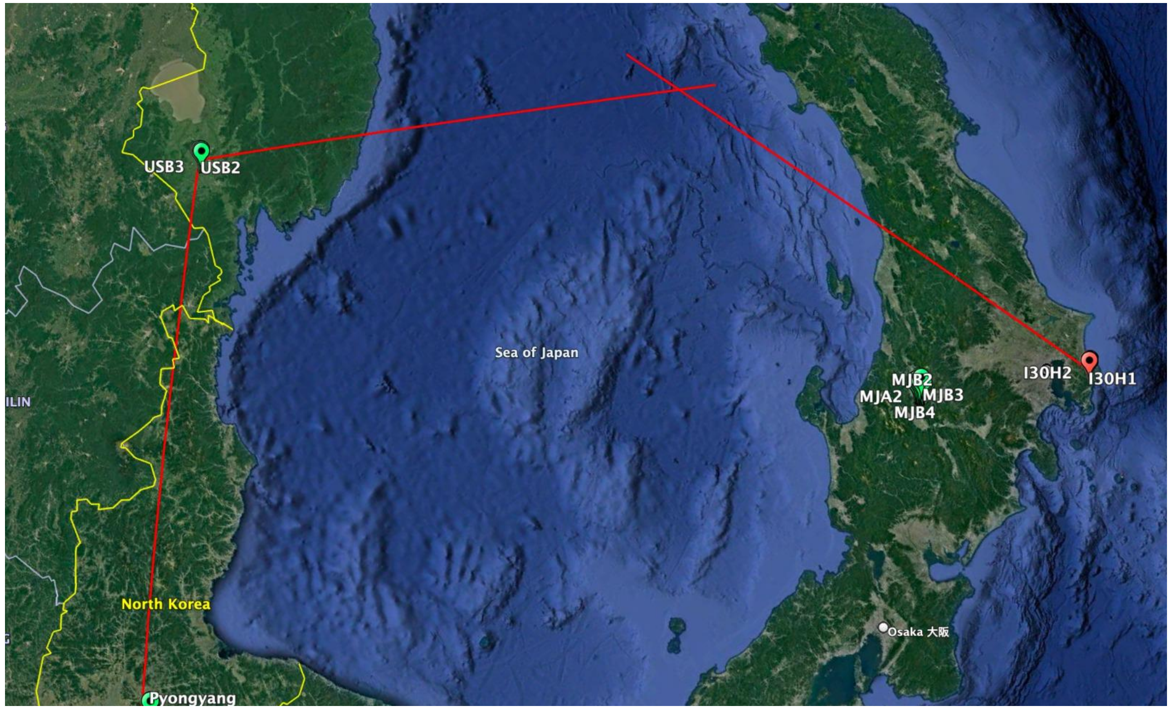

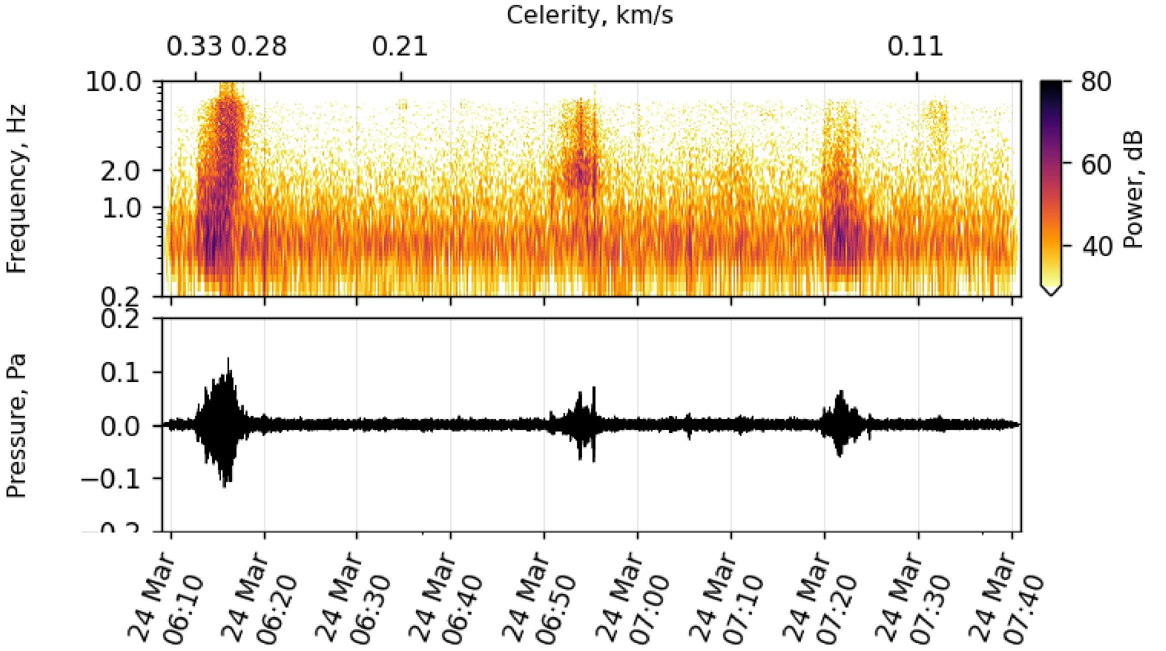

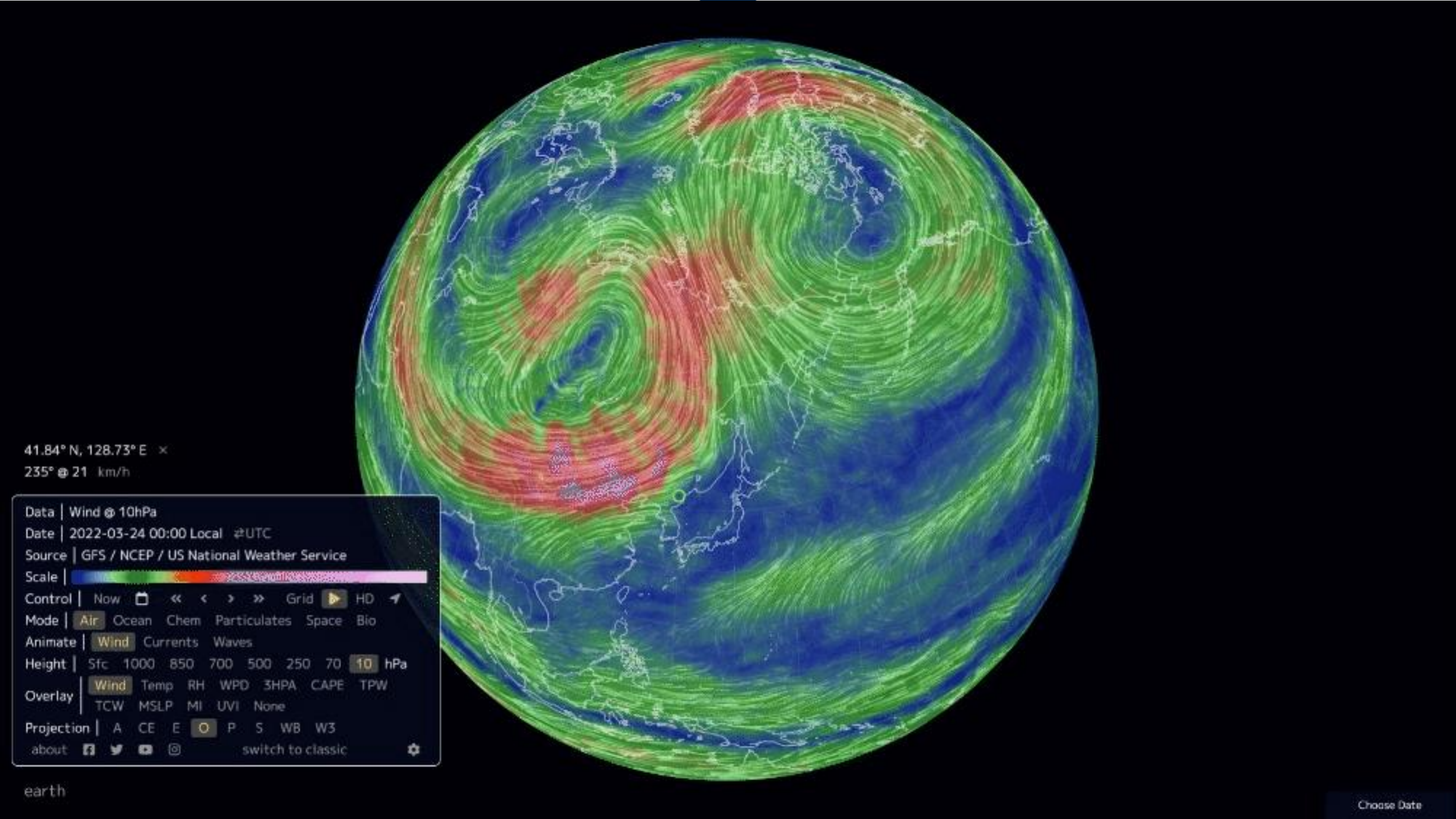

41.84° N, 128.73° E ×
235° @ 21 km/h
Data | Wind @ 10hPa
Date | 2022-03-24 00:00 Local ⇄UTC
Source | GFS / NCEP / US National Weather Service
Scale |
Control | Now « ‹ › » Grid HD
Mode | Air Ocean Chem Particulates Space Bio
Animate | Wind Currents Waves
Height | Sfc 1000 850 700 500 250 70 10 hPa
Overlay | Wind Temp RH WPD 3HPA CAPE TPW
TCW MSLP MI UVI None
Projection | A CE E O P S WB W3
about switch to classic
earth
Choose Date

A Seismo-Acoustic Analysis of the 3 September 2017 event

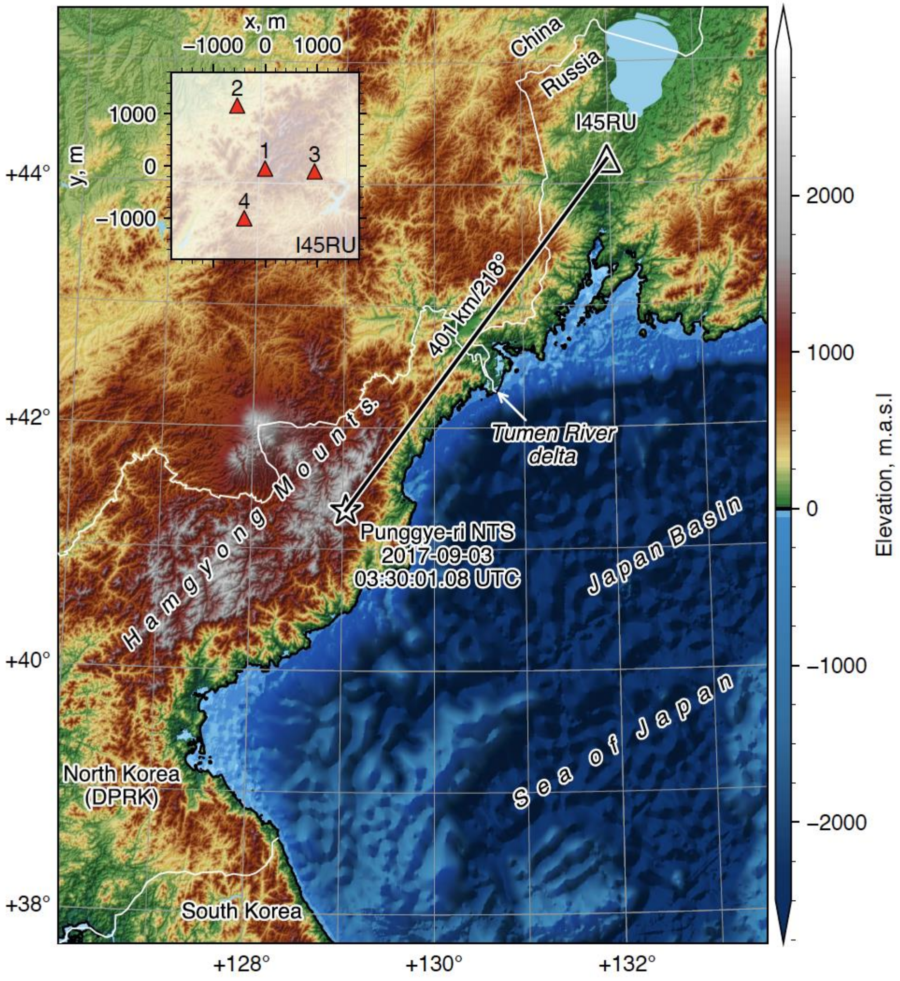

Largest DPRK event till date, estimated seismic magnitude m_b 6.1, estimated yield 200-300 kT TNT.

Collapse of underground cavity 8 minutes later, leading to magnitude m_b 4.1 event

Punggye-ri Test Site is below Mt. Mantap. Complex geology, site consist of granite rock.

Bathymetry in Japan Basin and sedimentary delta appear to be important in this study

Assink et al., Seism. Res. Lett., 2018

Seismo-acoustic coupling

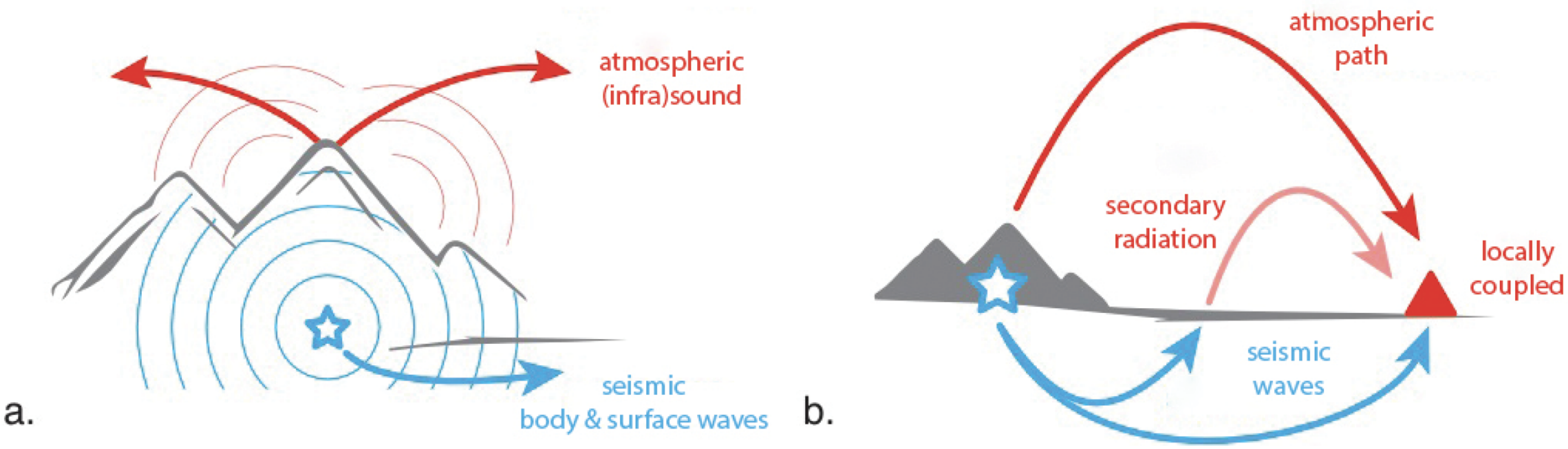

- Infrasound couples from the epicentral region, from distant topography and sedimentary basins as well as directly from below ('local infrasound'). Coupling is sensitive to hypocenter depth.
- The source depth is of particular interest for the estimation of yield but is poorly constrained from seismic data only. A seismo-acoustic analysis can provide additional constraints on this
- Characterizing the acoustic energy to determine source characteristics without having detailed knowledge of the local geology ('calibrating the test-site').

Comparison of seismic arrivals on broadband seismometer and microbarometer from 2017 DPRK nuclear test

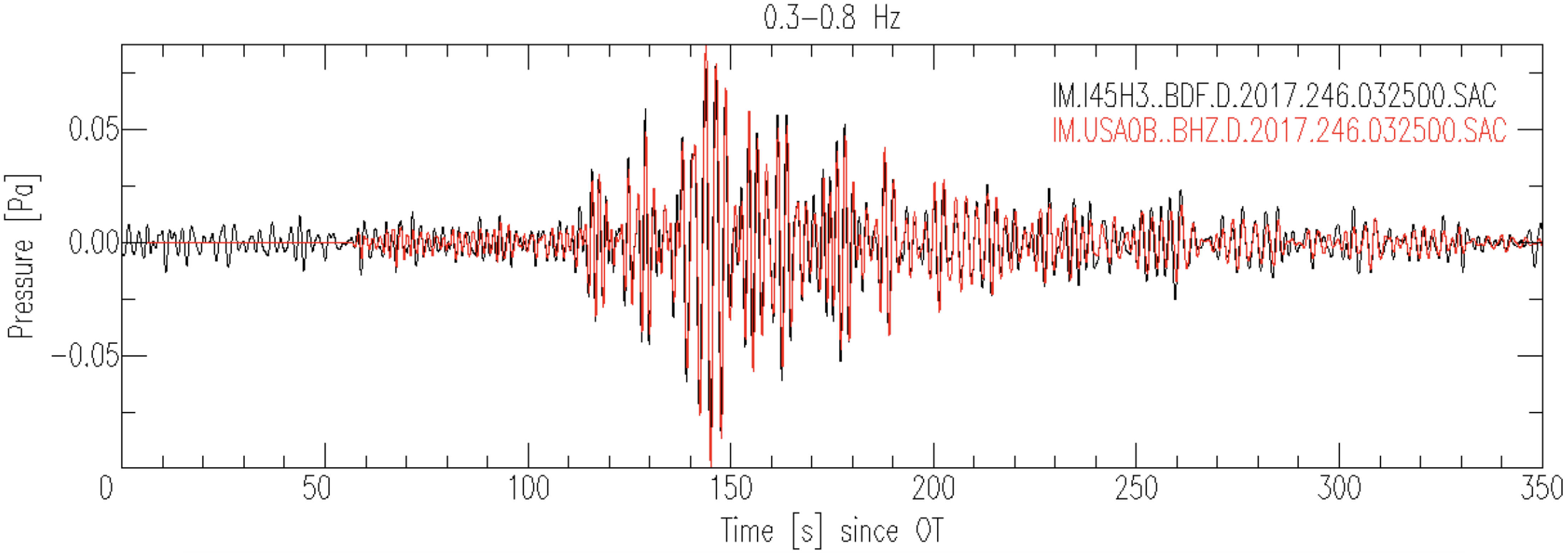

Equivalent pressure p due to ground velocity v: $p = \rho_0 c v \rightarrow p \approx 400v$

Seismo-acoustic coupling

SOUND WAVES IN THE ATMOSPHERE GENERATED BY A SMALL EARTHQUAKE†

By Hugo Benioff, Maurice Ewing and Frank Press

California Institute of Technology and Columbia University*

Communicated July 16, 1951

In previous papers[1–5] theoretical and experimental results on the coupling of atmospheric compressional waves to various types of surface waves in the underlying earth or ocean have been presented. Recently Benioff[6] presented a paper describing a remarkable instance of atmospheric waves received at Pasadena from the earthquake of January 24, 1951, 07-17-01, magnitude 5.6, 33° 07′N., 115° 34′W., $\Delta = 265$ km. The microbarograph

Geophys. J. R. astr. Soc. (1971) **26**, 191–198.

Infrasound Radiated During the Montana Earthquake of 1959 August 18

Richard K. Cook

(Received 1971 July 1)

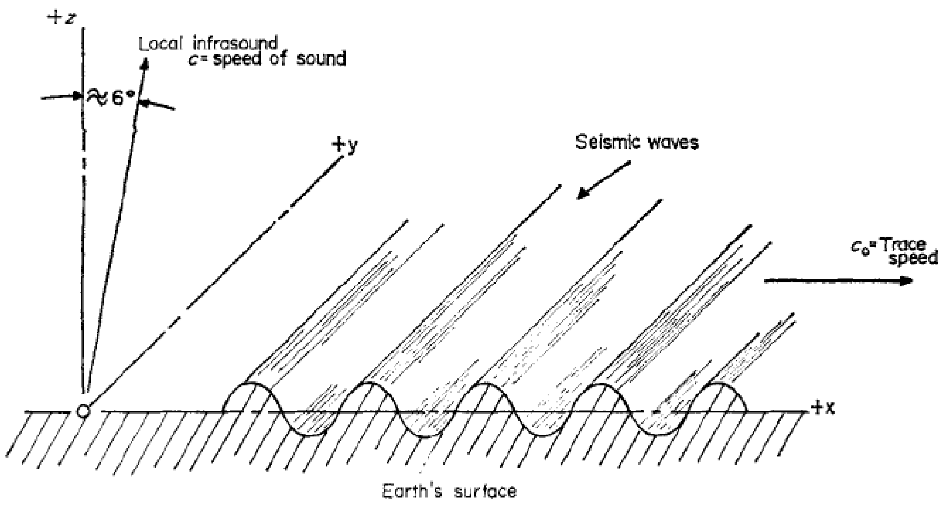

Fig. 1. Radiation of infrasound by surface motion due to a seismic wave.

Far field analysis

In the far field, the perturbations in velocity v_A and pressure p_A can be described as harmonic plane waves:

$$\begin{pmatrix} \mathbf{v}_A(\mathrm{x}, t) \\ p_A(\mathrm{x}, t) \end{pmatrix} = \begin{pmatrix} \hat{\mathrm{v}}_A e^{i(\mathrm{k}\cdot r - \omega t)} \\ \hat{p}_A e^{i(\mathrm{k}\cdot r - \omega t)} \end{pmatrix} \tag{1}$$

Substituting in the Euler equation:

$$\rho_0 \frac{\partial \mathrm{v}_A}{\partial t} = -\nabla p_A \tag{2}$$

leads to:

$$\hat{p}_A = \frac{\omega \rho_0 \hat{\mathrm{v}}_A}{\mathrm{k}} = \frac{\omega \rho_0 \hat{\mathrm{v}}_A \cdot \hat{k}}{\frac{\omega}{c}} = \rho_0 c (\hat{\mathrm{v}}_A \cdot \hat{k}) \tag{3}$$

where $\hat{k}$ represents the normal to the wavefront.

This implies that seismically vertically incident wavefront is in phase with the pressure, scaled by impedance $Z = \rho_0 c$.

Evanescent wave coupling

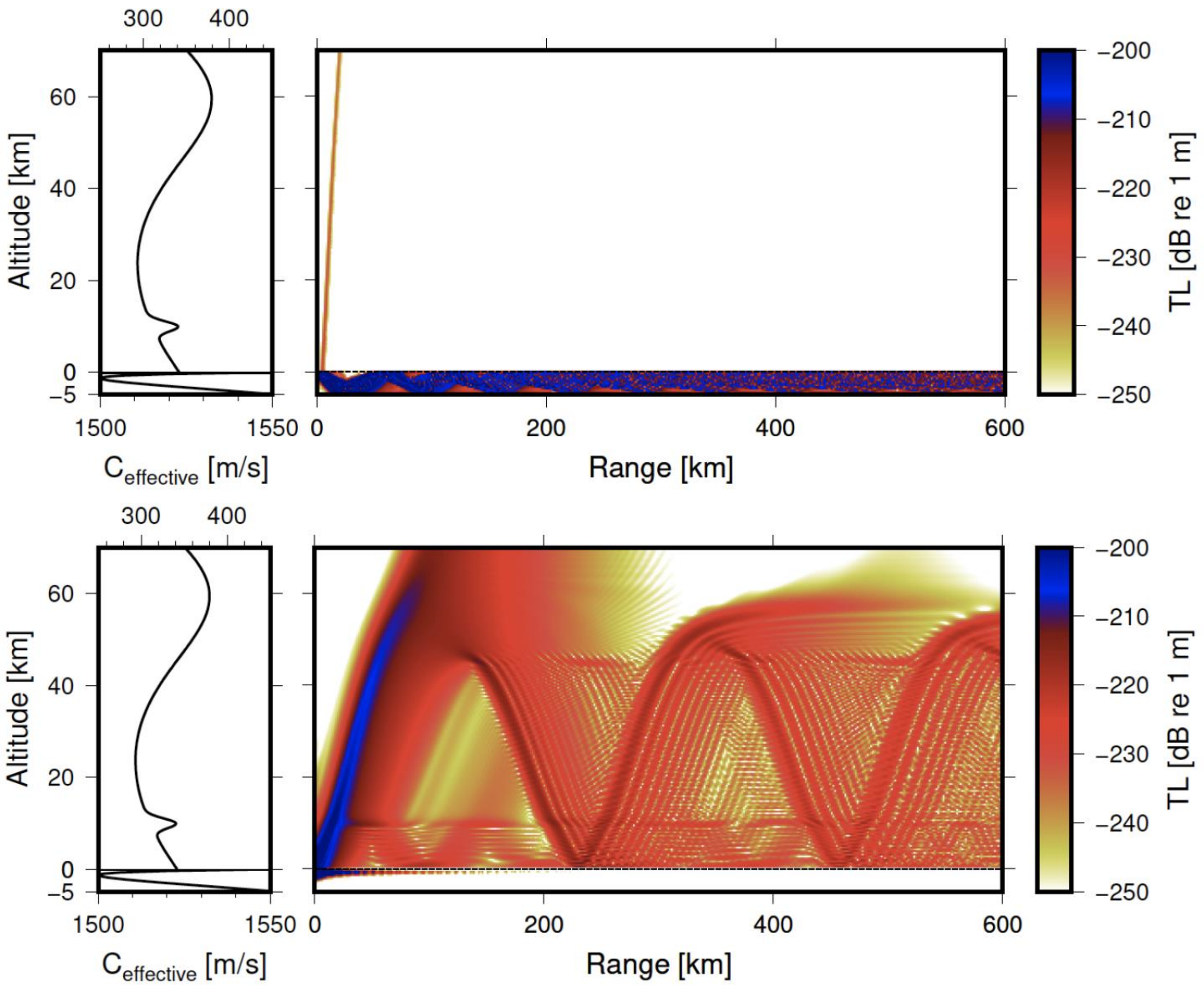

- Geophysical media are intrinsically coupled
- The coupling is pronounced at infrasonic frequencies
- Evanescent energy in oceans/earth can propagate in air
- The impedance contrast and topography play a role
- Figure: Source at 1000 m depth at 50 Hz (top) and 0.5 Hz (bottom)

Seismo-acoustic coupling

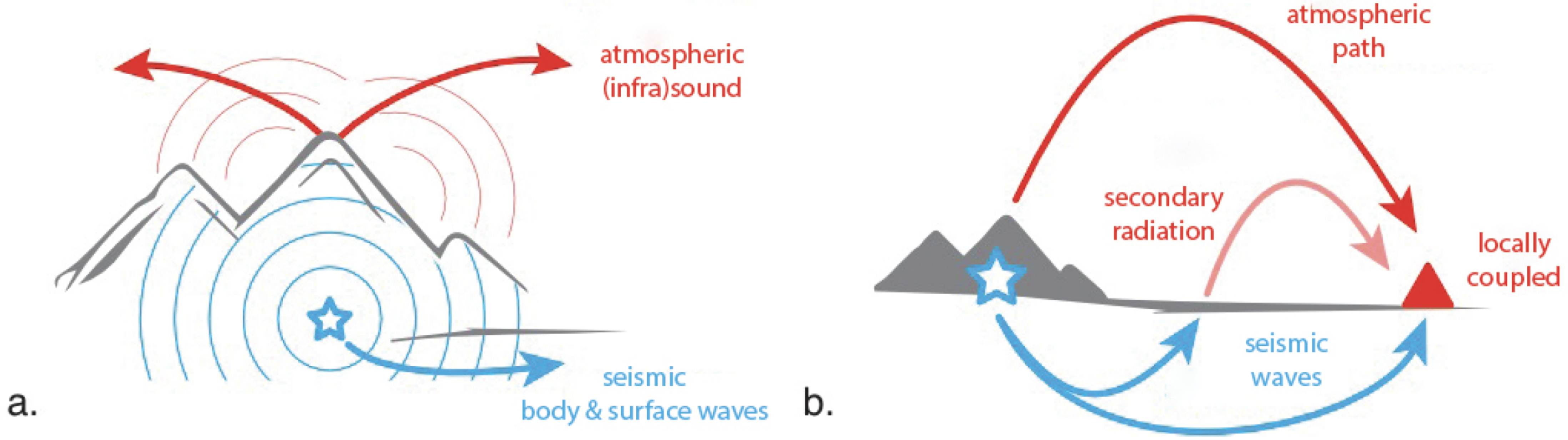

- Infrasound couples from the epicentral region, from distant topography and sedimentary basins as well as directly from below ('local infrasound'). Coupling is sensitive to hypocenter depth.
- The source depth is of particular interest for the estimation of yield but is poorly constrained from seismic data only. A seismo-acoustic analysis can provide additional constraints on this
- Characterizing the acoustic energy to determine source characteristics without having detailed knowledge of the local geology ('calibrating the test-site').

Detail waveform analysis

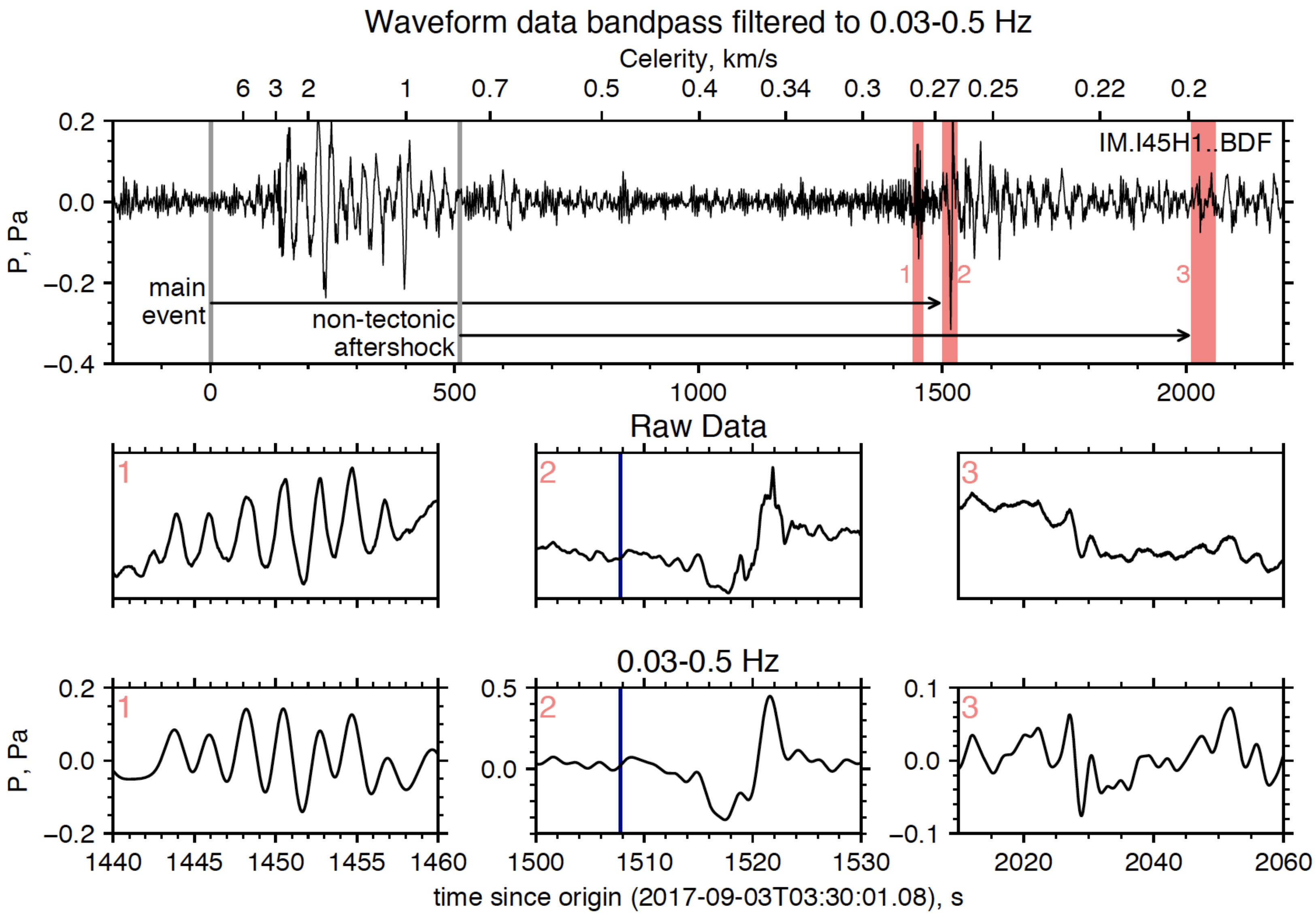

Assink et al., Seism. Res. Lett., 2018

Array processing

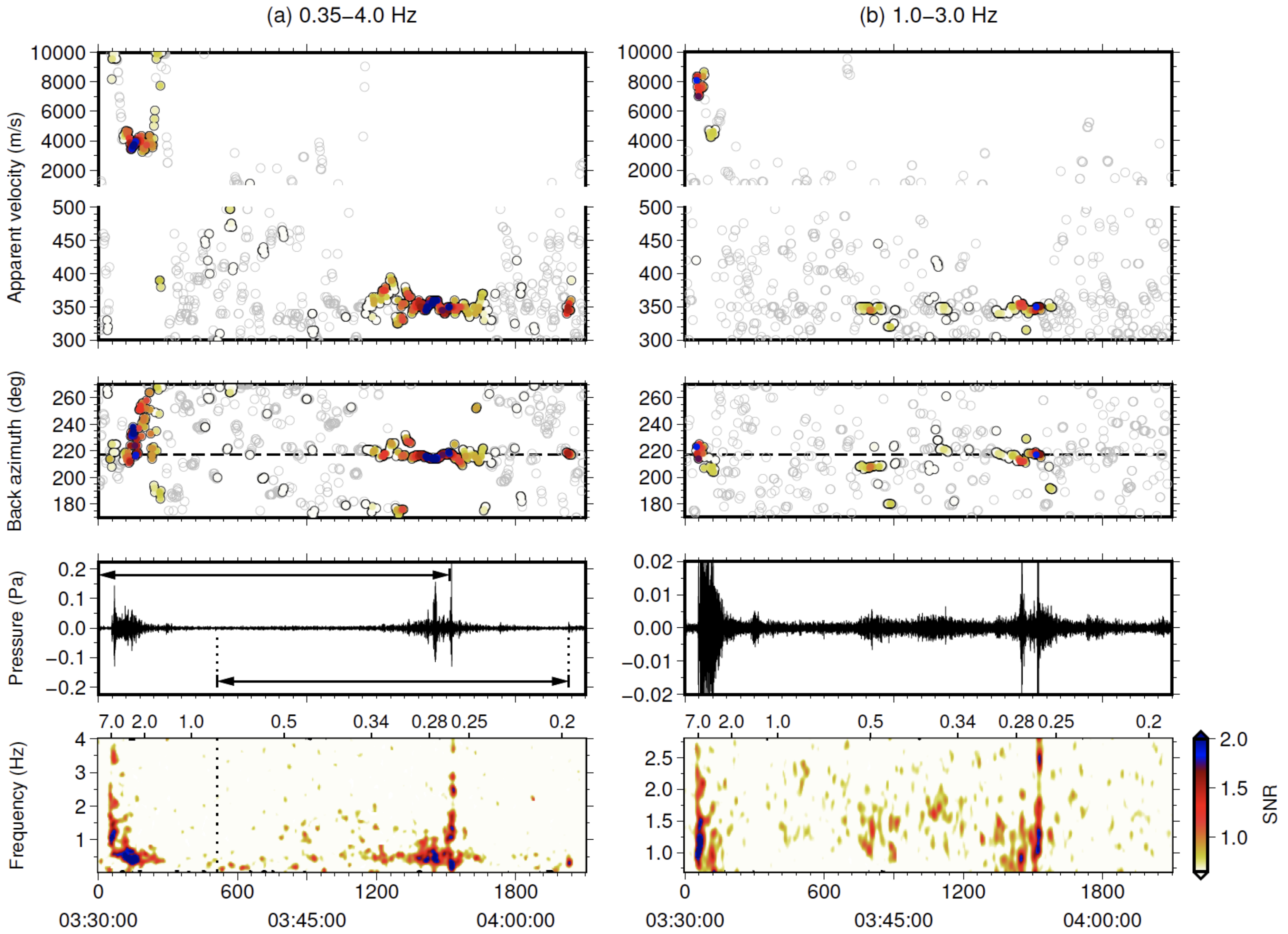

Seismic and acoustic signals separated in time and apparent velocity

Acoustic arrivals coming in **before** the expected acoustic arrival time

Several phases standing out in the emergent wavetrain

Assink et al., Seism. Res. Lett., 2018

Back projections of array processing

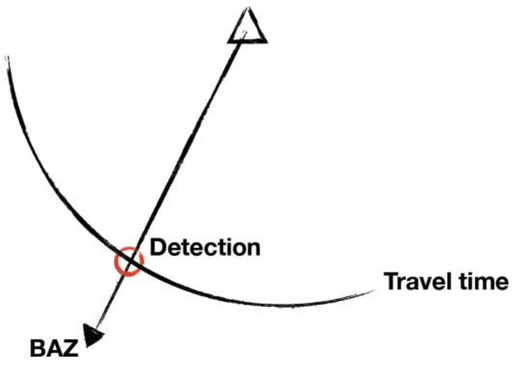

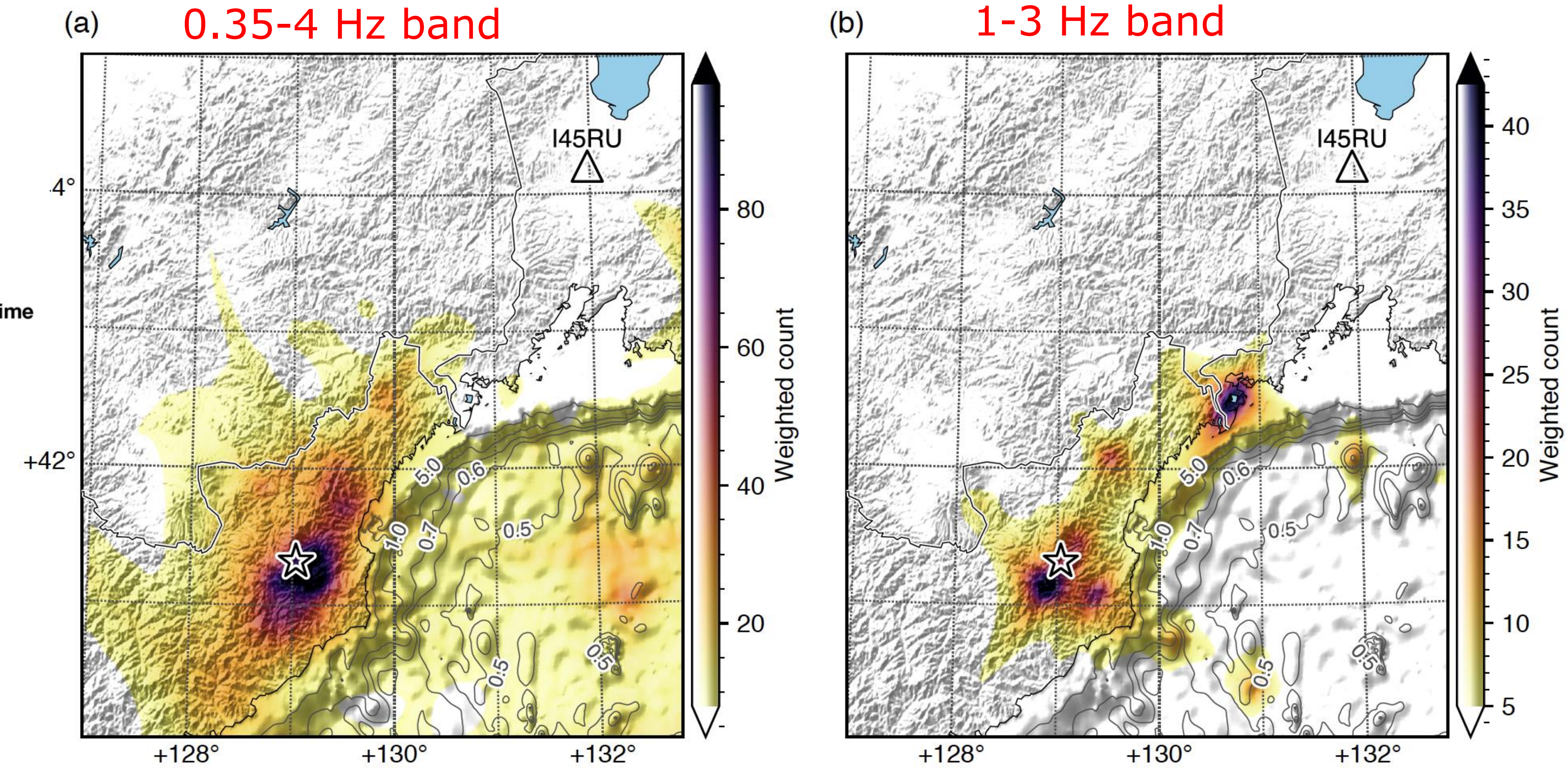

- Back projections show that seismic energy couples from the earth and sea into the atmosphere.
- The radiation of energy is frequency dependent
- This is consistent with earlier studies of coupled infrasound from (underwater) earthquakes

Assink et al., Seism. Res. Lett., 20

Towards Acoustic ShakeMaps: 2010 Haiti Mw 7 earthquake

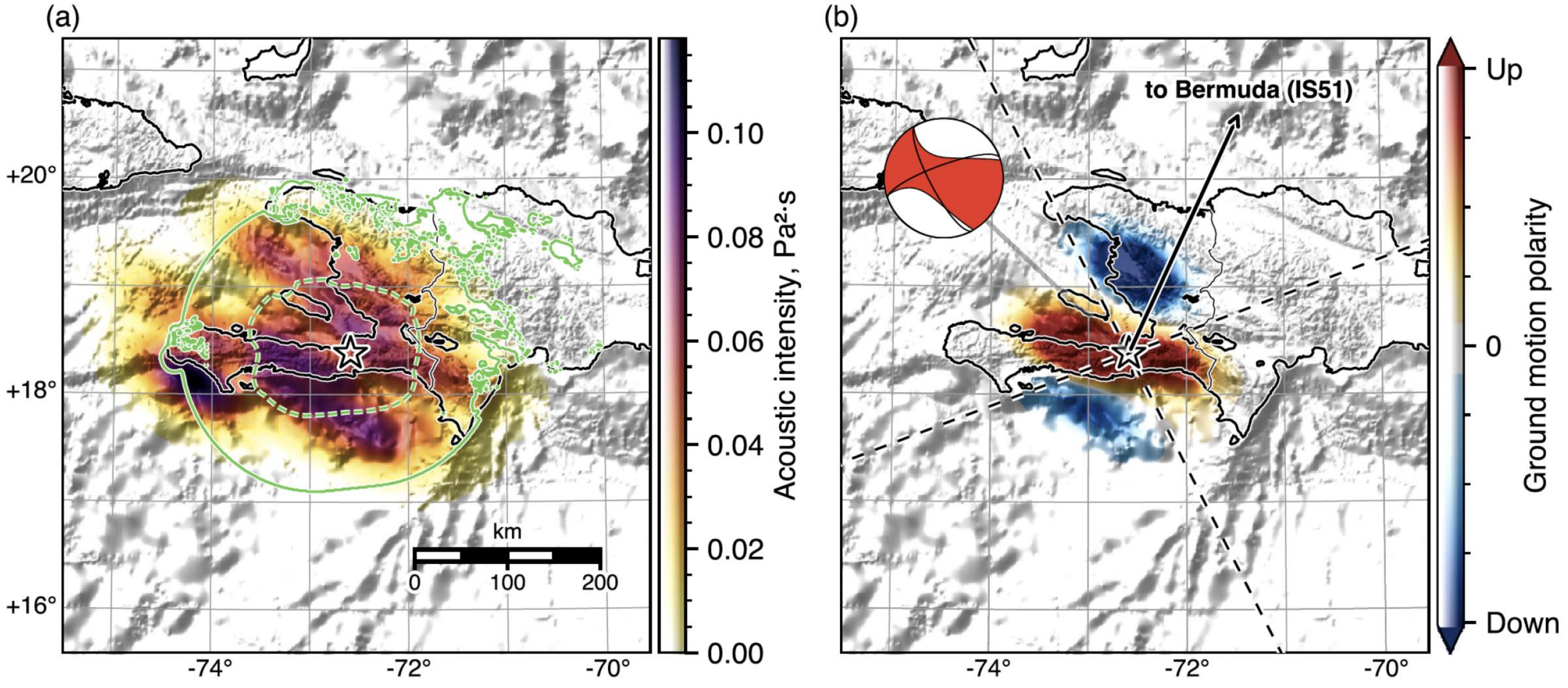

Back projections can help to estimate the intensity of the shaking and the source mechanism.

2021

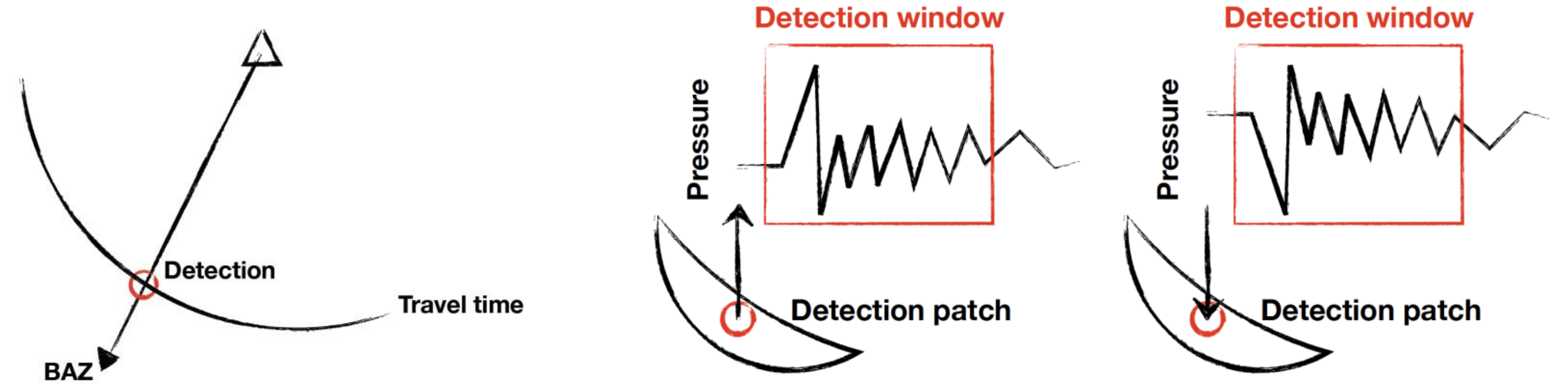

Microbaroms

Microbaroms are continuously detected as background acoustic noise

Knowledge of microbaroms

1. Understand infrasound noise background for verification work

2. Use for atmospheric remote sensing (*Donn-Rind, 1970s*)

3. Use for ocean-wave model validation?

High-resolution multi-source beamforming is a useful tool

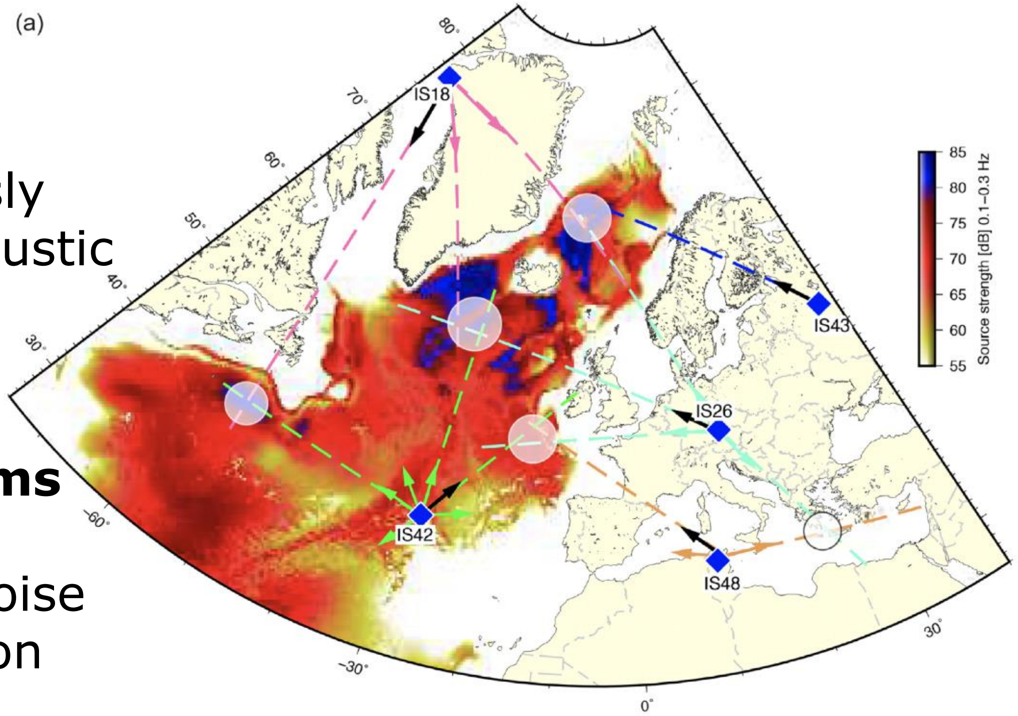

Campus & Christie, 2009

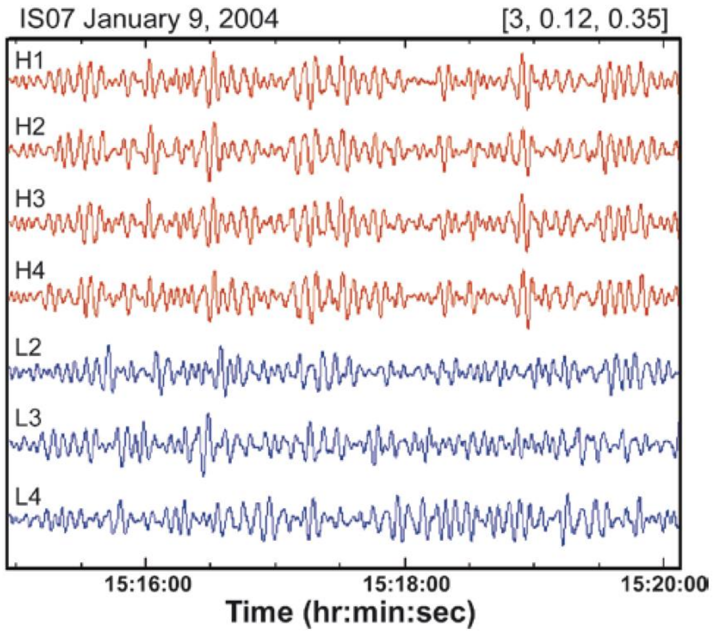

Ouden et al., GJI, 2020

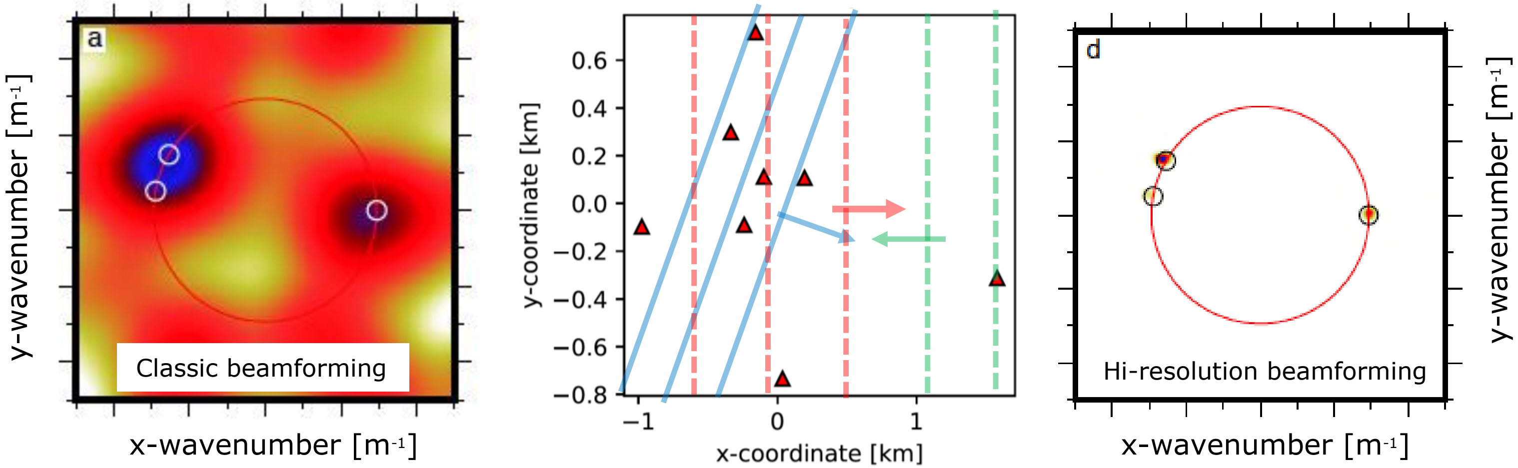

Microbaroms observations during a volcanic eruption

Ulawun volcano 2019,
IS40 (P.-New Guinea)

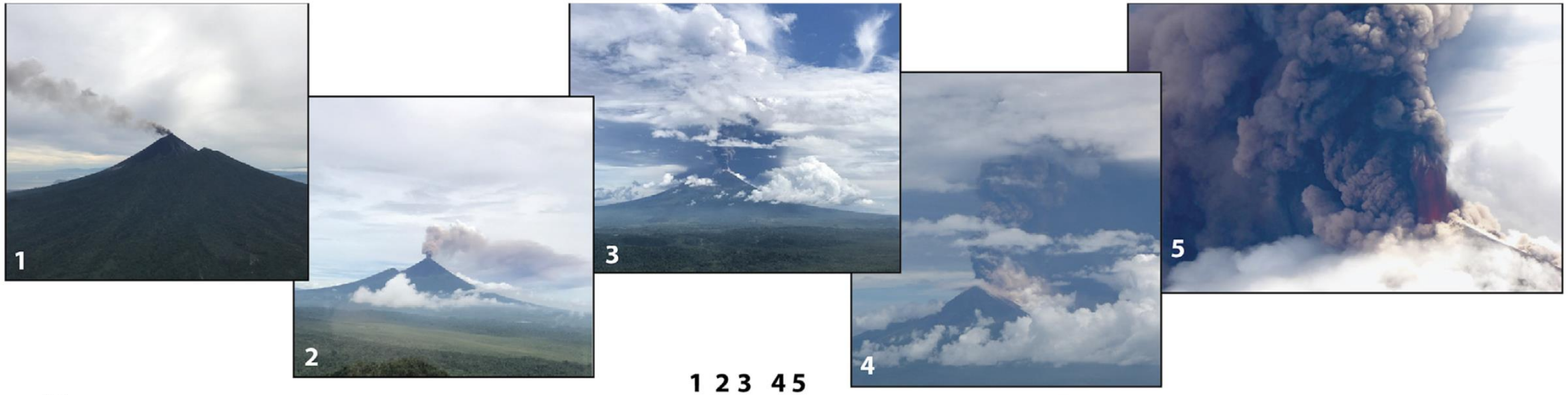

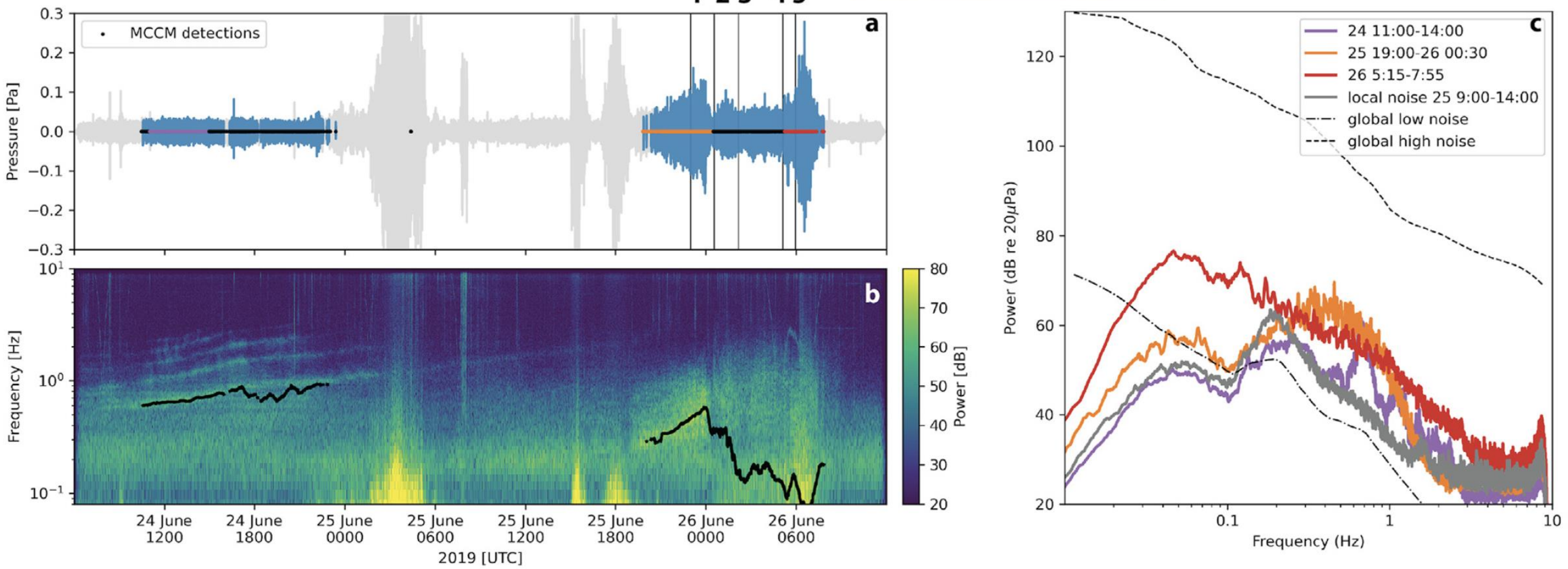

McKee et al, 2021

Microbaroms

Microbaroms are continuously detected as background acoustic noise

Knowledge of microbaroms

1. Understand infrasound noise background for verification work

2. Use for atmospheric remote sensing (*Donn-Rind, 1970s*)

3. Use for ocean-wave model validation?

High-resolution multi-source beamforming is a useful tool

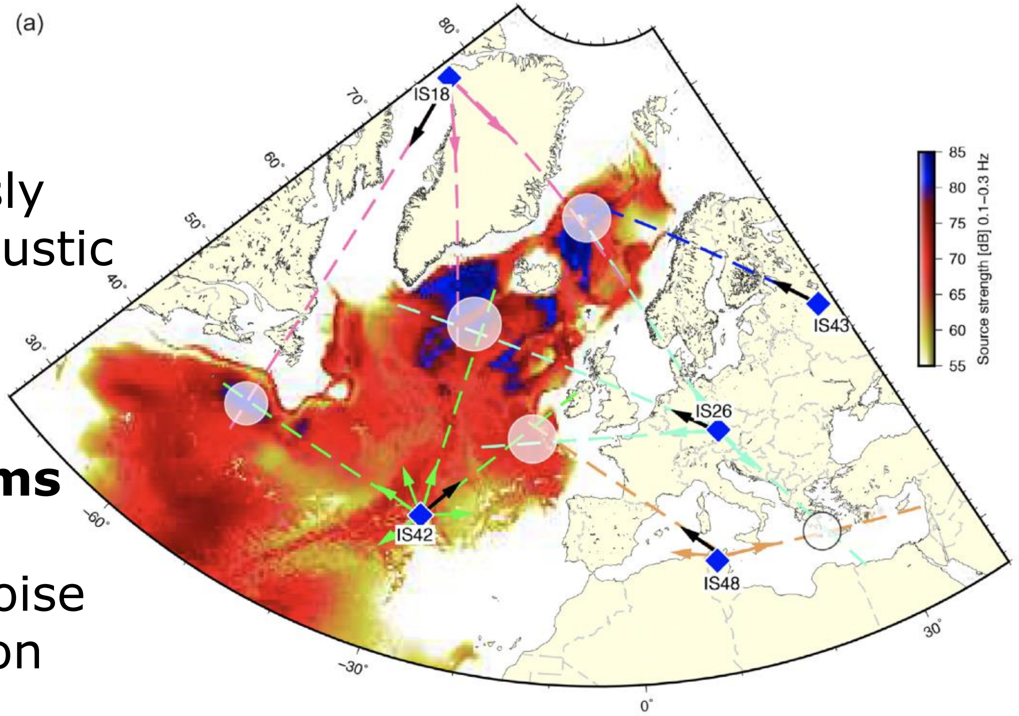

Campus & Christie, 2009

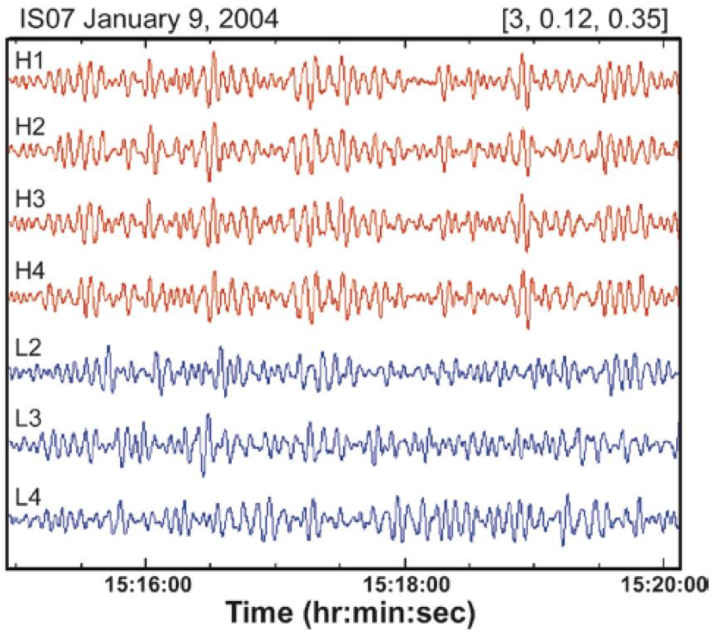

Ouden et al., GJI, 2020

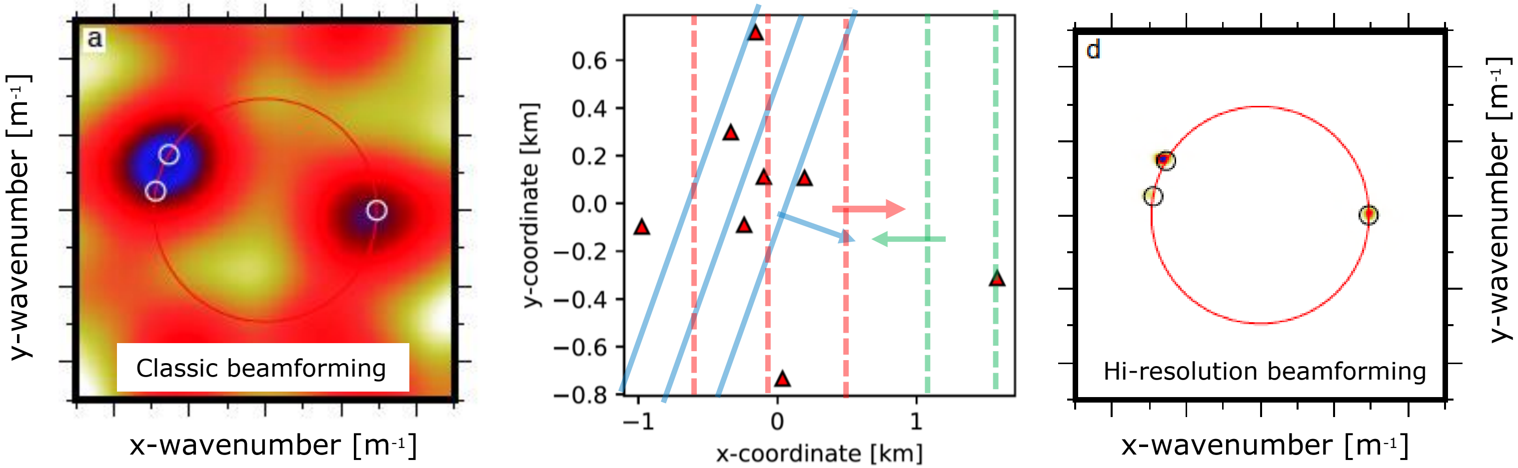

Take-off for a near-source measurement

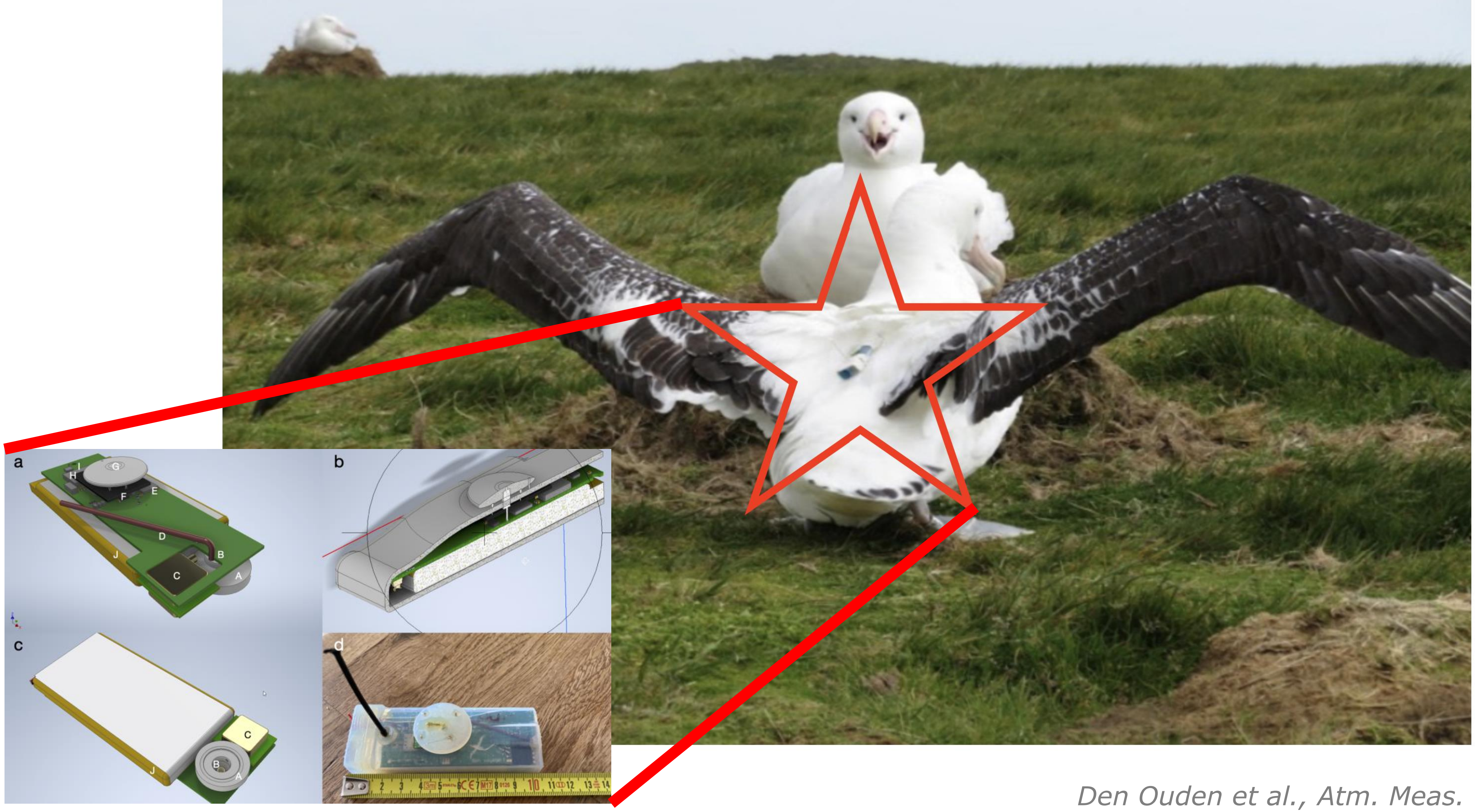

Den Ouden et al., Atm. Meas. Tech., 2021

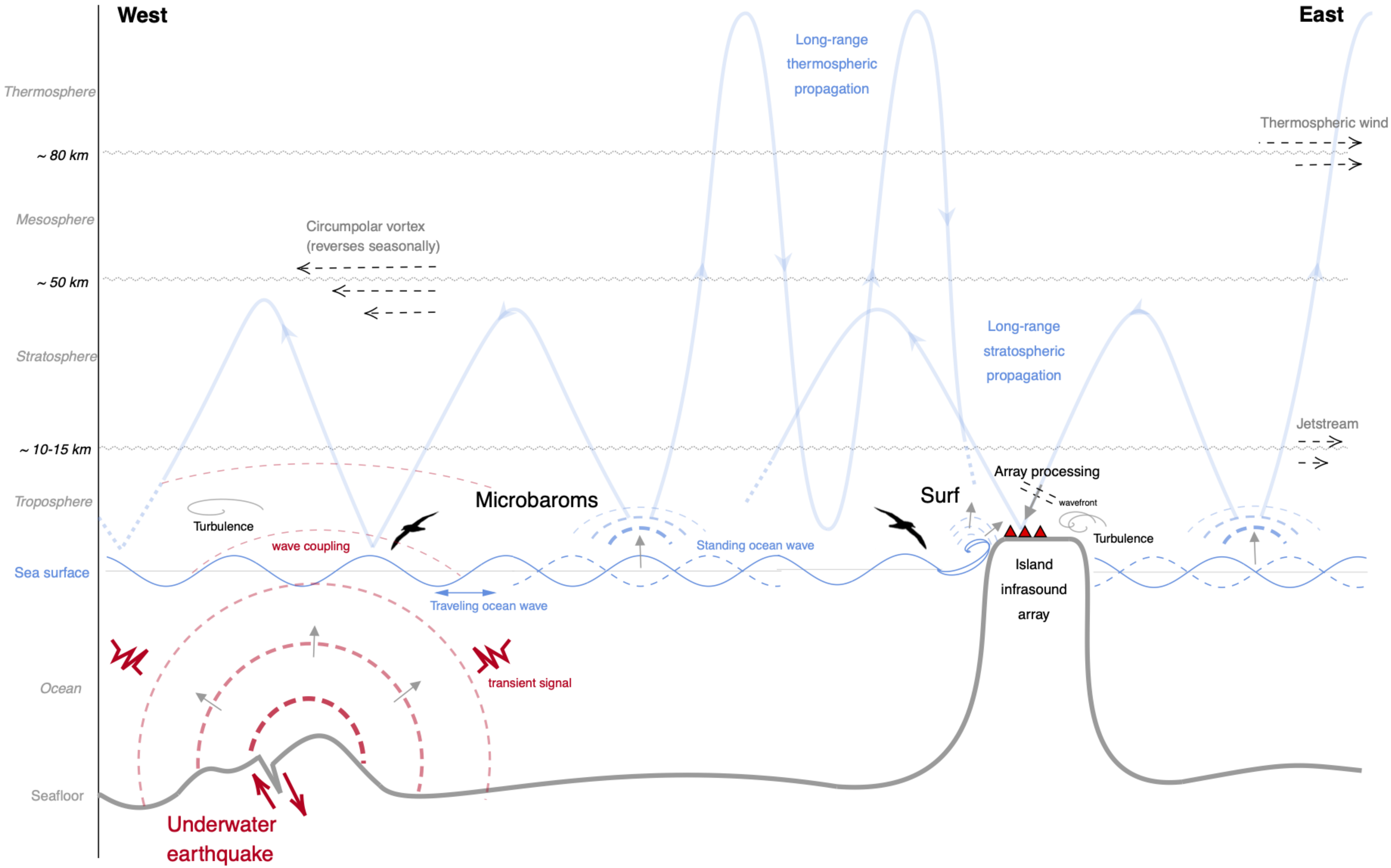
West
East
Thermosphere
~ 80 km
Mesosphere
~ 50 km
Stratosphere
~ 10-15 km
Troposphere
Sea surface
Ocean
Seafloor
Long-range thermospheric propagation
Thermospheric wind
Circumpolar vortex (reverses seasonally)
Long-range stratospheric propagation
Jetstream
Array processing
wavefront
Microbaroms
Surf
Turbulence
wave coupling
Standing ocean wave
Traveling ocean wave
Turbulence
Island infrasound array
transient signal
Underwater earthquake

Reconstruction of Soundscapes

(1) Grid construction

(2) Microbarom source model

(3) Long-range propagation

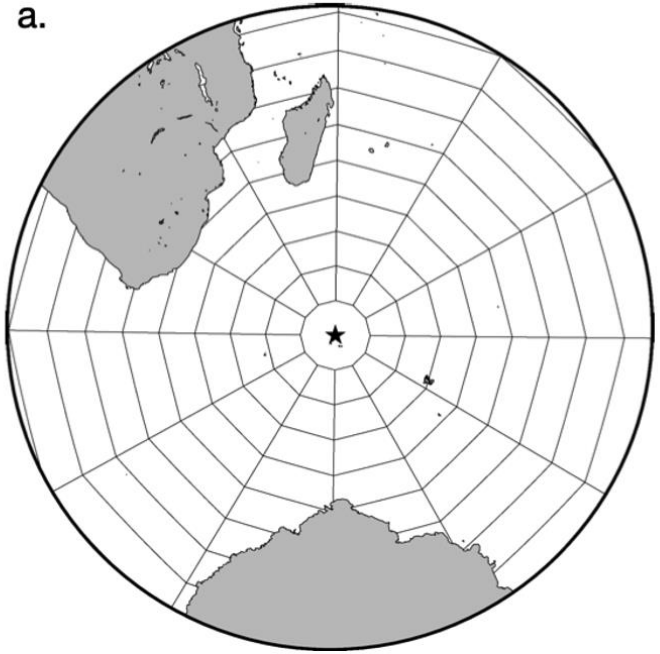

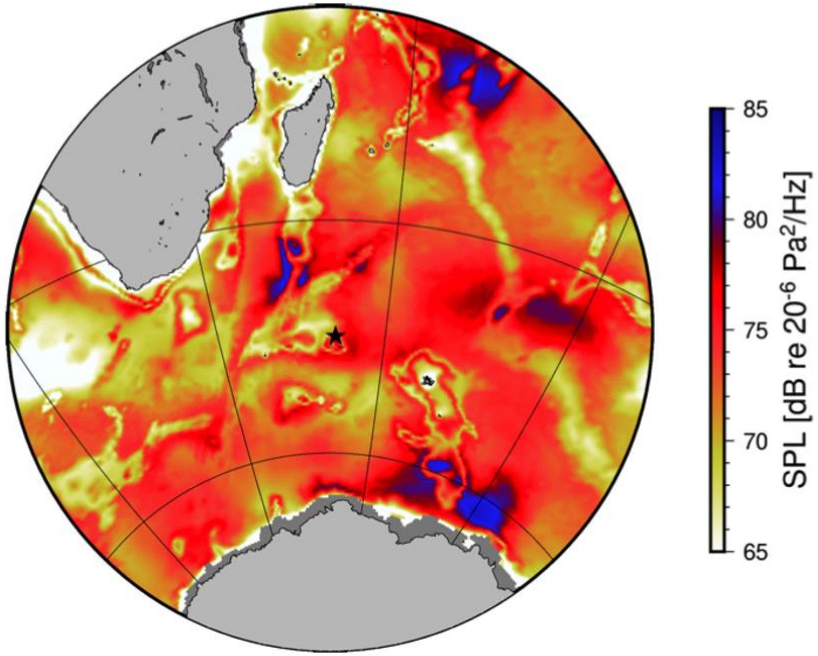

Waxler, 2007

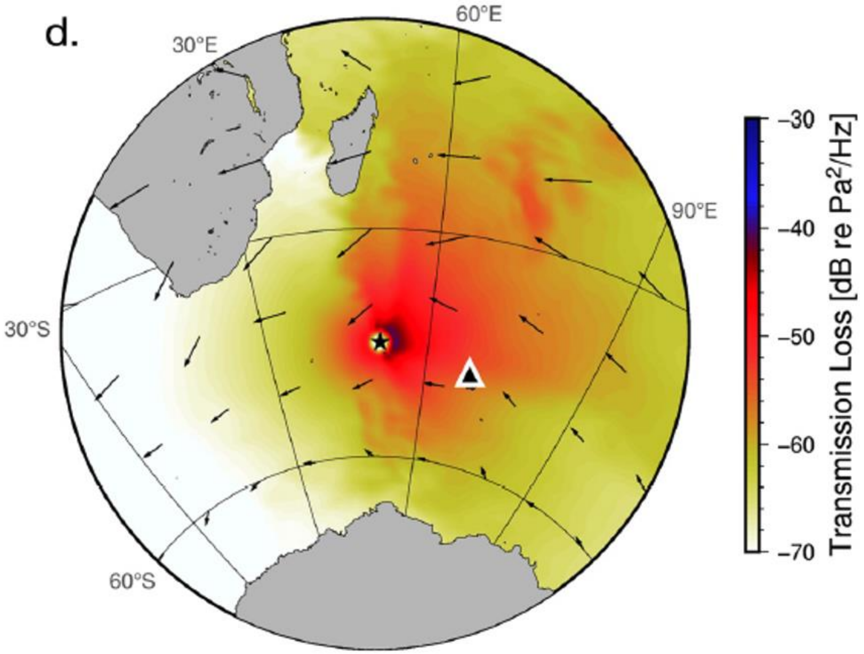

Le Pichon et al, 2011

Den Ouden et al., GRL, 2021

Reconstruction of soundscapes: the math

$$
\begin{aligned}
\mathcal{P}_{av}(f, t_{\text{obs}}, x_r) &= \sum_i \mathcal{P}_{av,i}(f, t_{\text{obs}}, x_r) \\
&= \underbrace{\iint_{S_r} \mathcal{P}_1(f, t_{\text{obs}}, x_r)\, dS_r}_{\text{Evanescent microbaroms}} \\
&+ \underbrace{\sum_i \iint_{S_i} \mathcal{P}_2(f, t_0(\tau), x_s) \times G_p(f, t_{\text{obs}} - \tau, x_s, x_r)\, dS_i}_{\text{Propagating microbaroms}}
\end{aligned}
$$

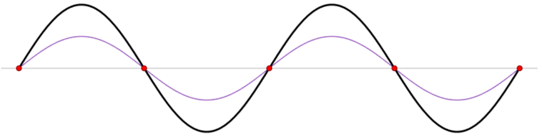

Ocean wave-wave interaction

Evanescent microbarom source term

$$\mathcal{P}_1(f_a) \sim \rho_a c_a^2 \frac{2\pi f_{p0}^2}{k_{p0} c_a} \frac{2\pi f_0 \overline{F}_w(f_w)}{c_a}$$

Hasselmann integral

$$\boxed{\mathcal{H}(f_w)} = \int_0^{2\pi} F(f_w, \phi_w) F(f_w, \phi_w - \pi)\, d\phi_w$$

Propagating microbarom source term

$$\mathcal{P}_2(f_a) = 4g^2 \pi^4 f_a^3 \underline{\mathcal{H}(f_w)} \frac{\rho_a^2}{c_a^2} \left(\frac{9g^2}{4\pi^2 c_a^2 f_a^2} + \frac{c_a^2}{c_w^2} \frac{A}{B} + \frac{3g}{2\pi c_w f_a} \frac{C}{B} \right)$$

Waxler & Gilbert, 2006; Waxler et al., 2007

Reconstruction of Soundscapes

(1) Grid construction

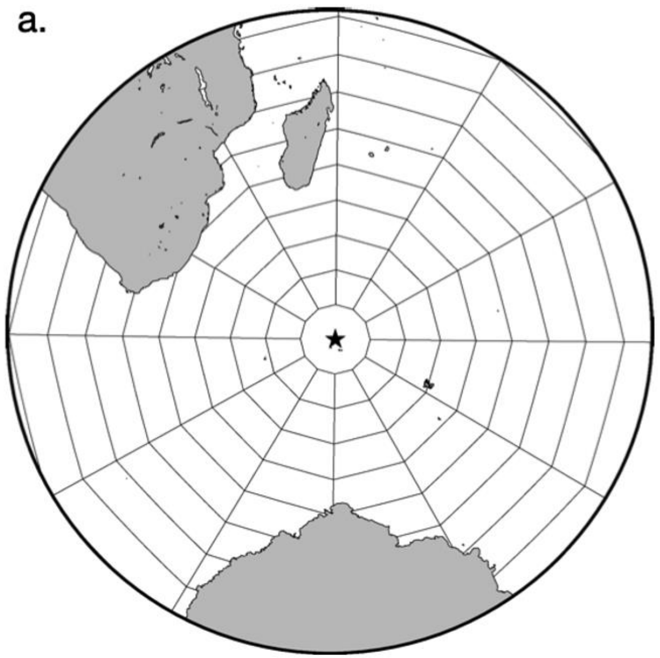

(2) Microbarom source model

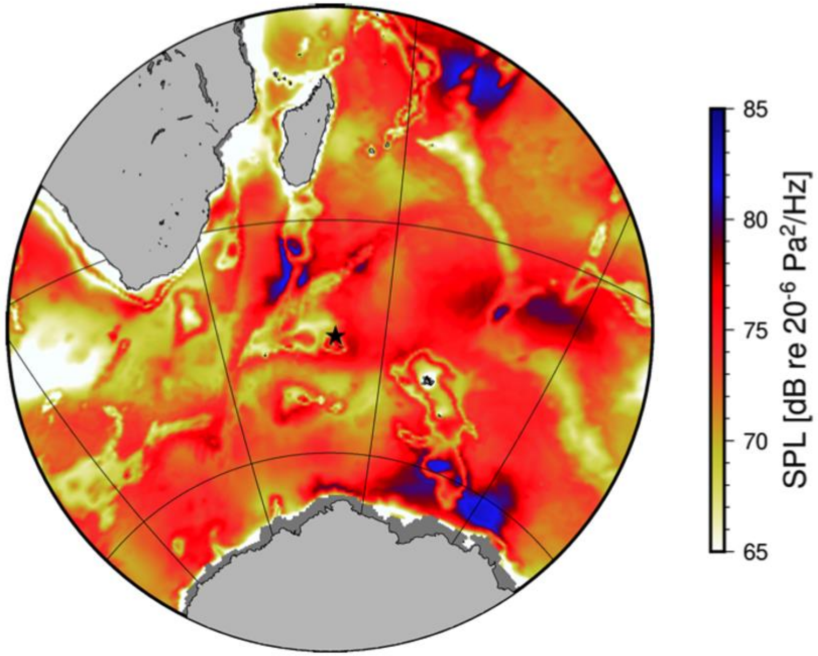

Waxler, 2007

(3) Long-range propagation

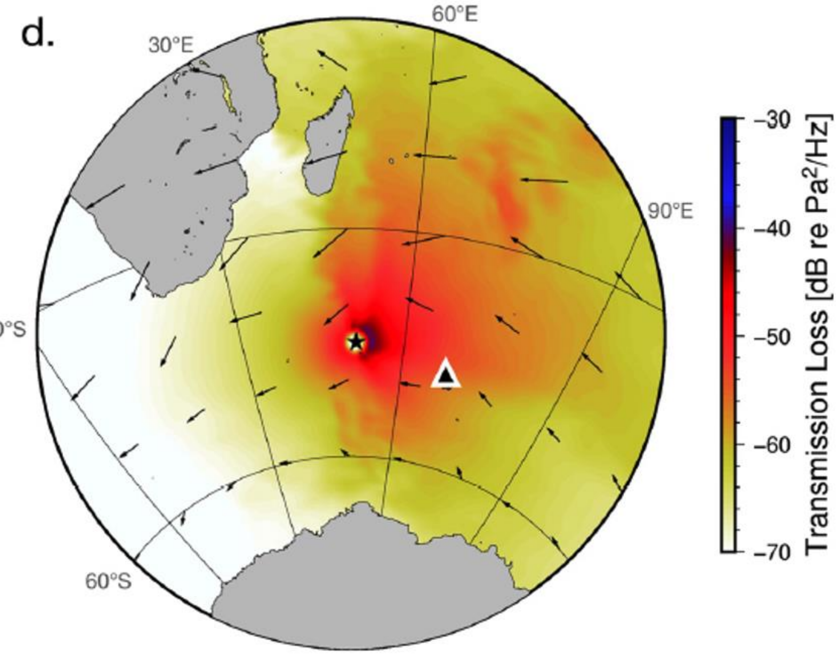

Le Pichon et al, 2011

Den Ouden et al., GRL, 2021

Models and observations at different sites

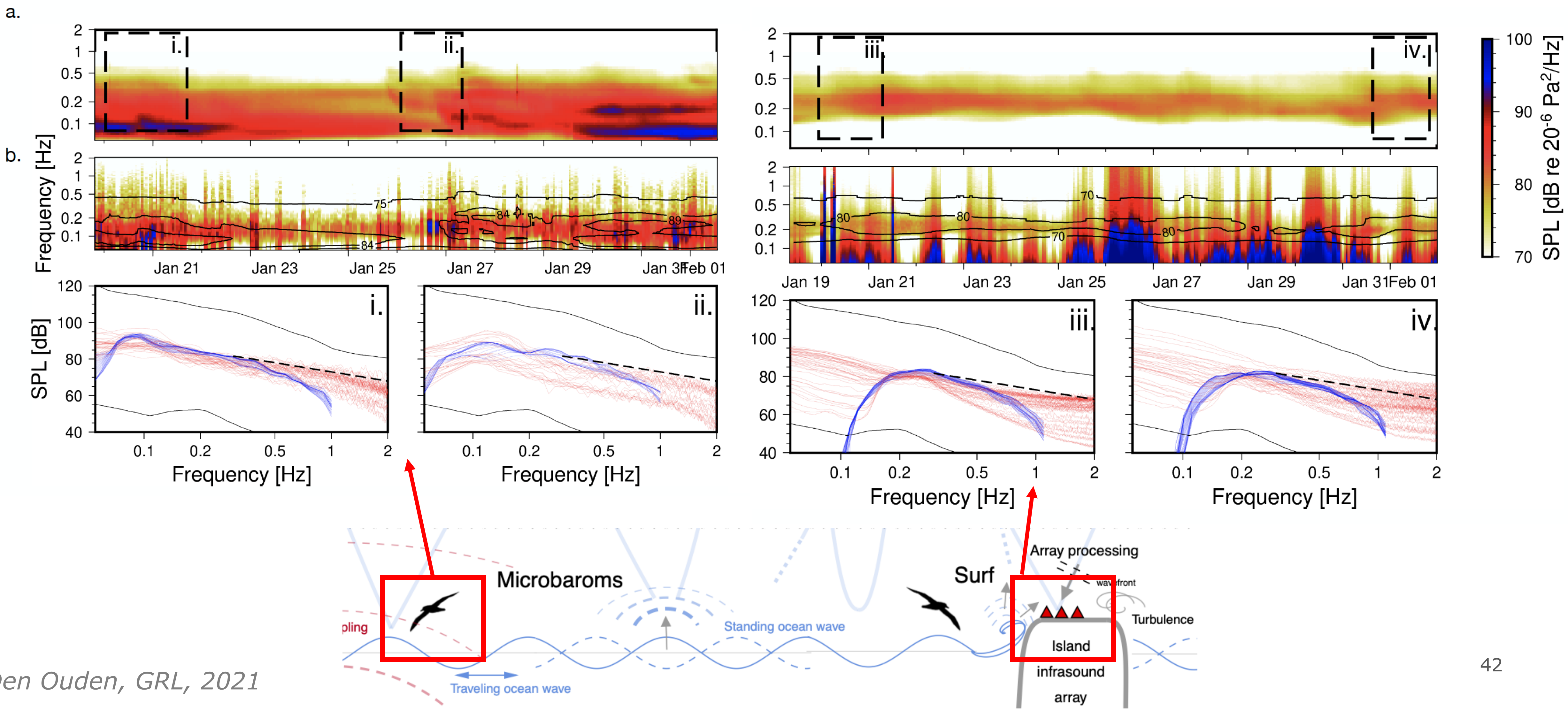

Den Ouden, GRL, 2021

Time-dependent soundscape for a moving receiver

Locations of wandering albatross

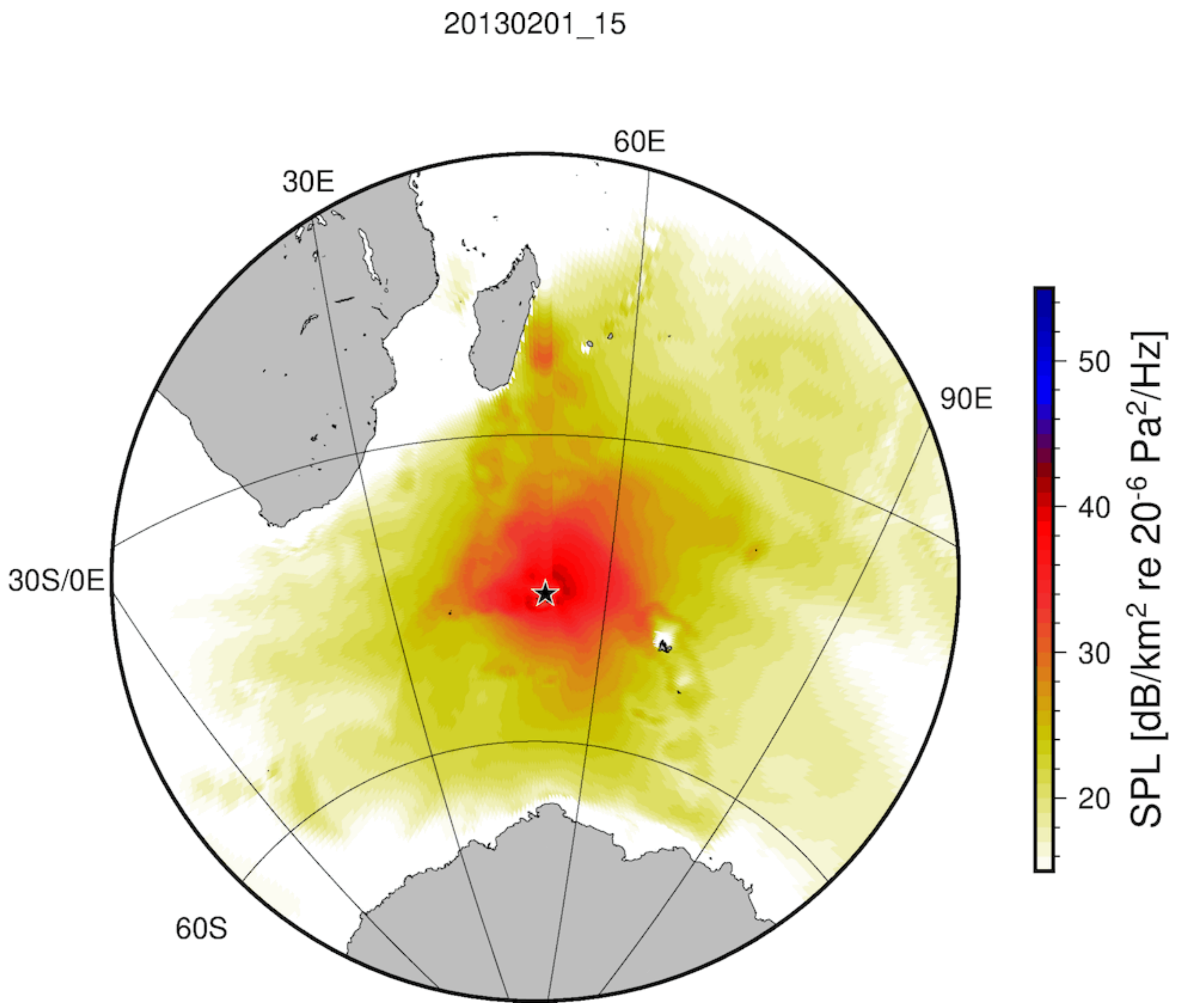

Den Ouden, 2022

Time-dependent soundscape for a static receiver

Station IS23 – Kerguelen Island

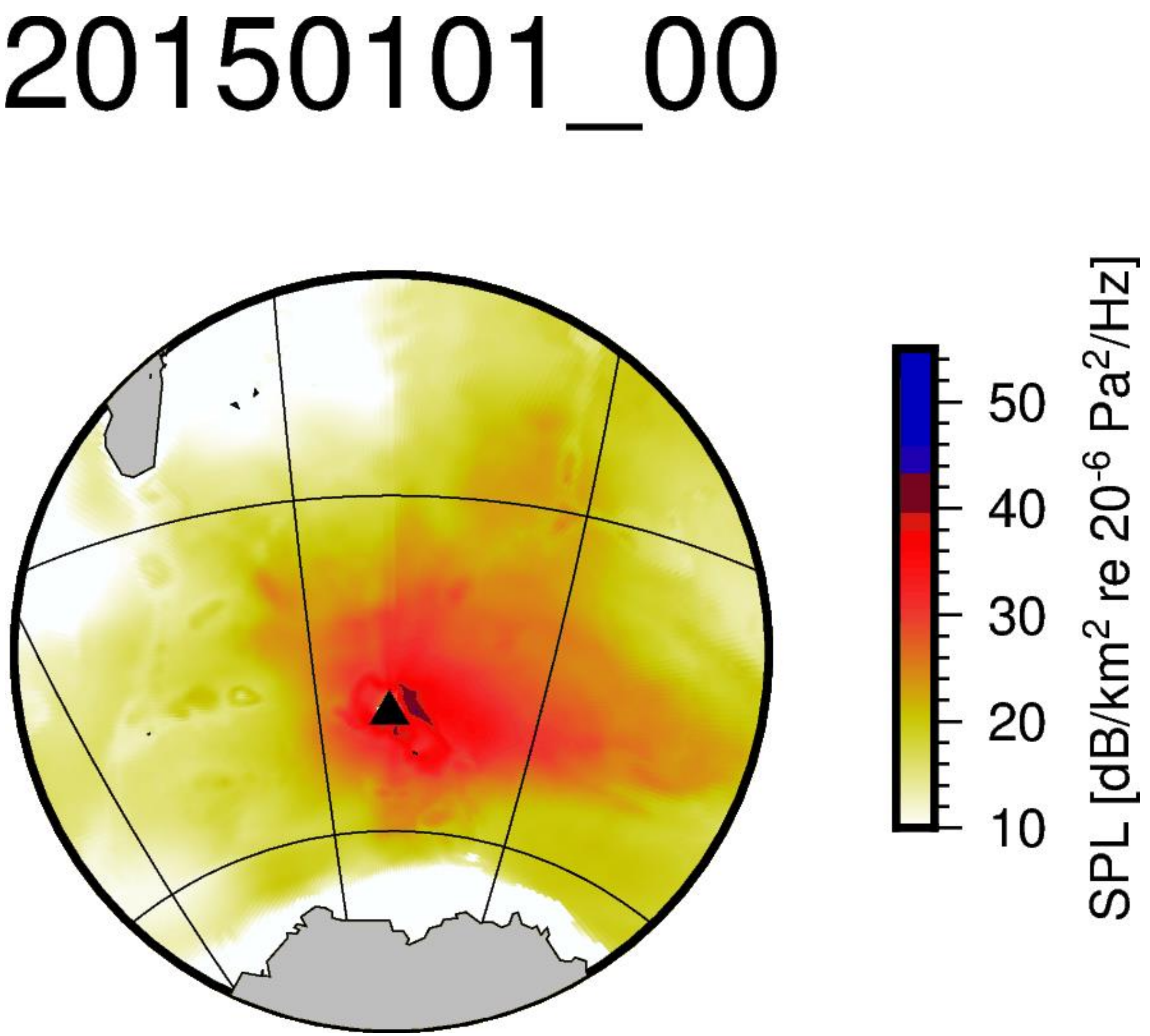

Den Ouden, 2022

A climatology of five year of microbaroms at Kerguelen

model

observations

difference

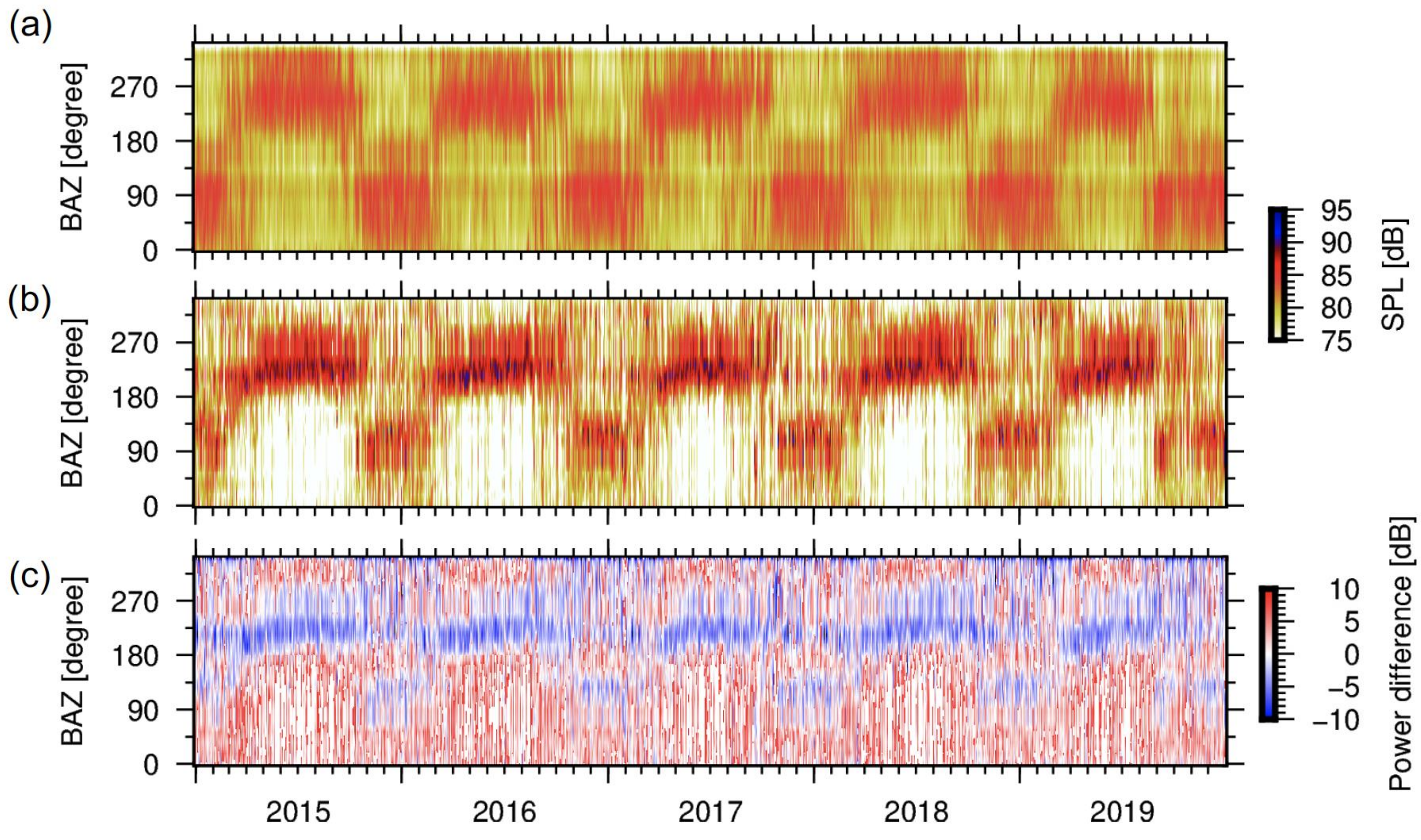

Den Ouden et al, 2022, GJI

A climatology of five year of microbaroms at Kerguelen

model

observations

difference

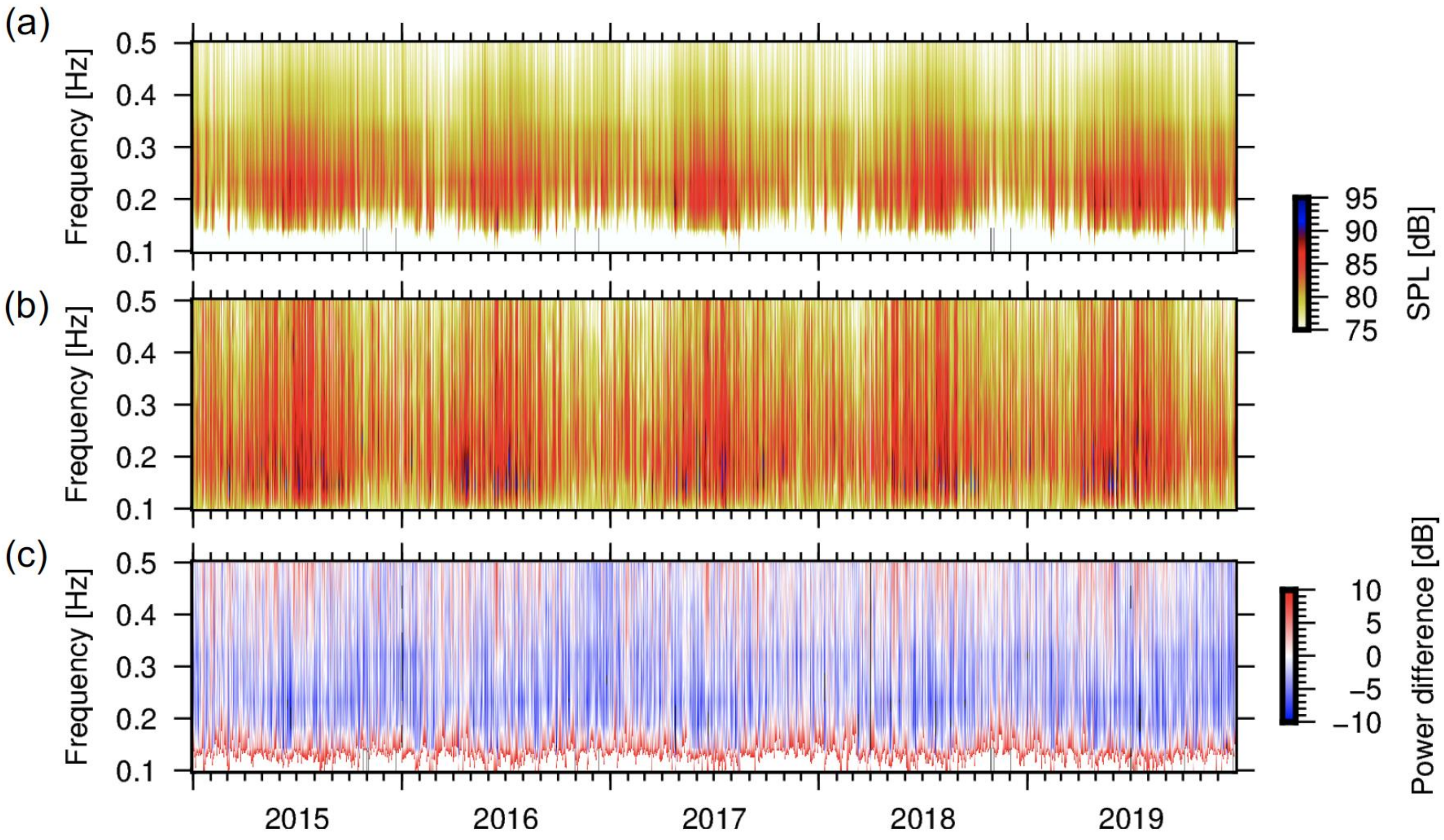

Den Ouden et al, 2022, GJI

The (infra)sound of climate change

- I18DK is part of International Monitoring System for CTBT verification
- I18DK is configured as an array of eight microbarometers
- Operational since 2004, now 19 years (18 summers) of infrasonic recordings

Infrasound sources around I18DK

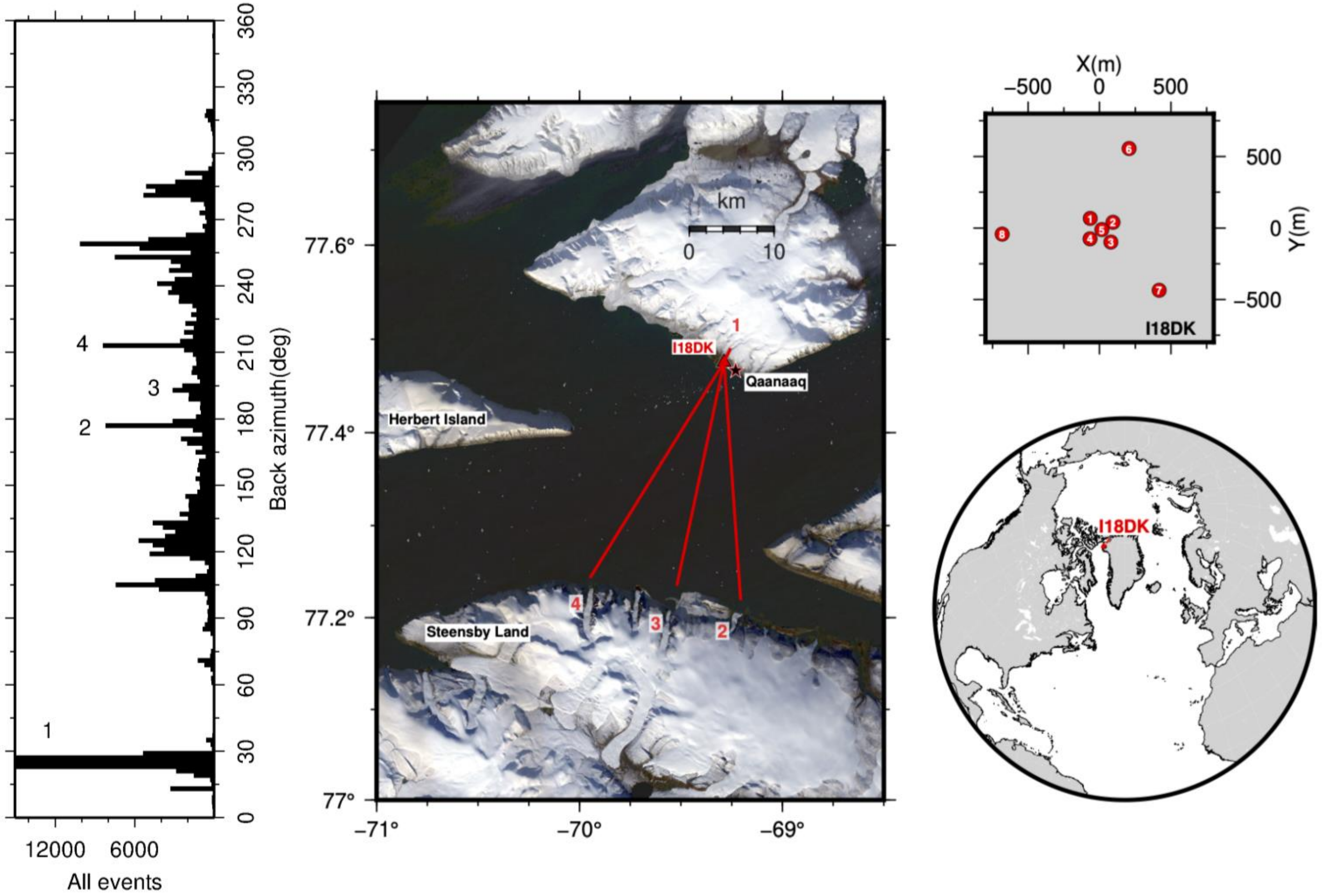

- 1, Land-terminating Qaanaaq glacier 1.5 km to North of I18DK
- 2-4, Three sea-terminating glaciers 30 km to the South

Evers et al., GRL, 2022 (in review)

Infrasound event detections for 18 summers

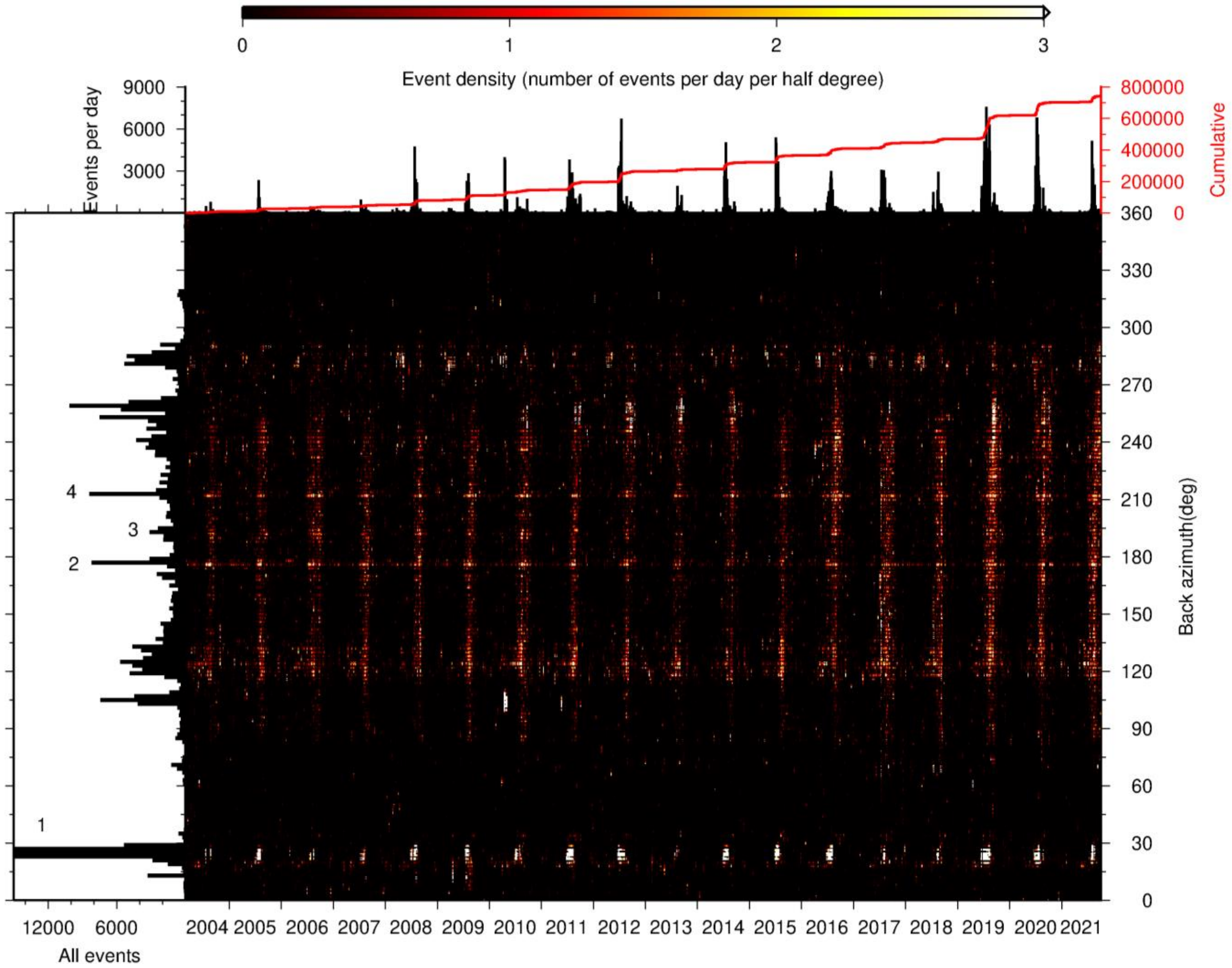

- Bright colors: many events, dark colors: few/no events
- Vertical bands: strong activity in summer, non in winter
- Horizontal bands: events appear from specific directions over the years
- Yearly variations in infrasonic activity

Evers et al., GRL, 2022 (in review)

Qaanaaq glacier: detections versus modeled discharge

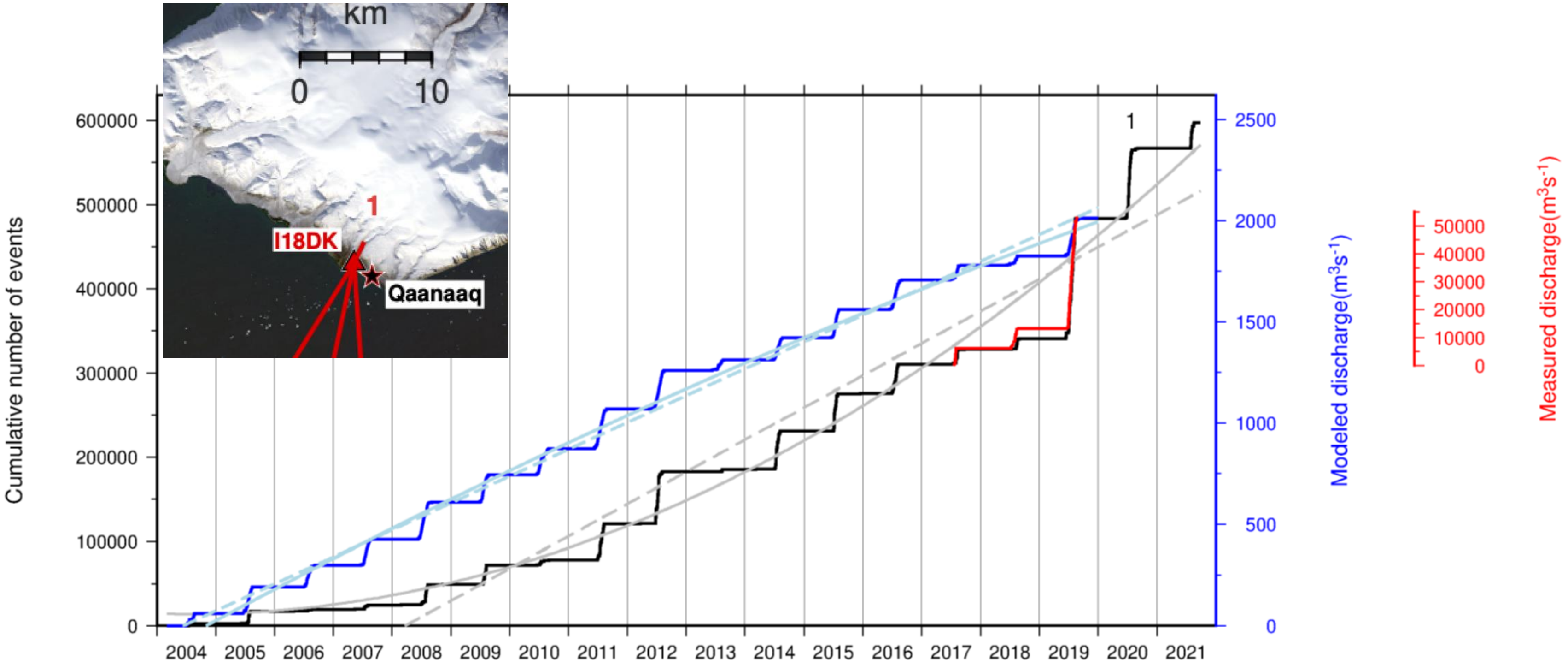

- Modeled discharge (blue): Mankoff et al. (2020), Earth System Science Data, 10.5194/essd-12-2811-2020
- Measured (red): Kondo et al. (2021), J. Glaciology, 10.1017/jog.2021.3

Podolskiy, Hokkaido University, Japan (July 2019)

Evers et al., GRL, 2022 (in review)

Qaanaaq glacier: driven by atmospheric temperature

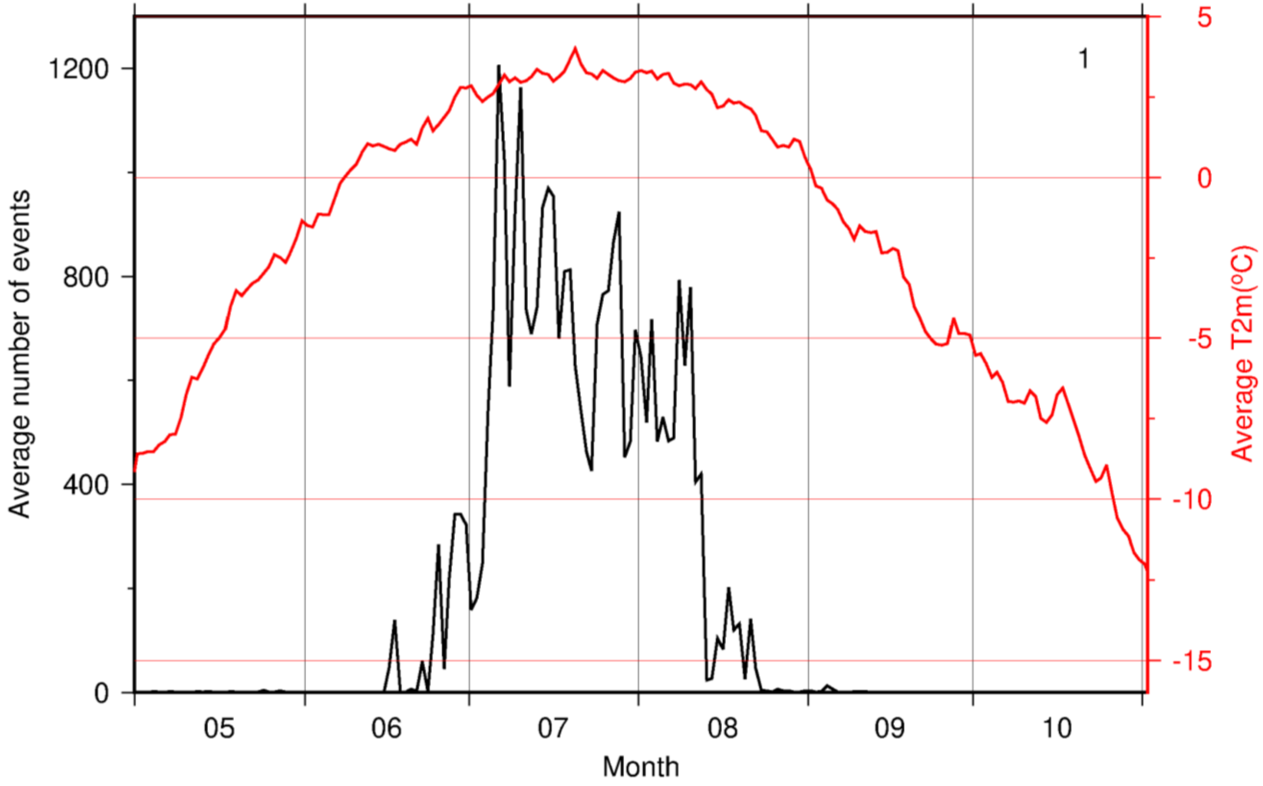

- Infrasonic event rate in phase with atmospheric temperature

Evers et al., GRL, 2022 (in review)

Sea-terminating glaciers: driven by seawater temperature

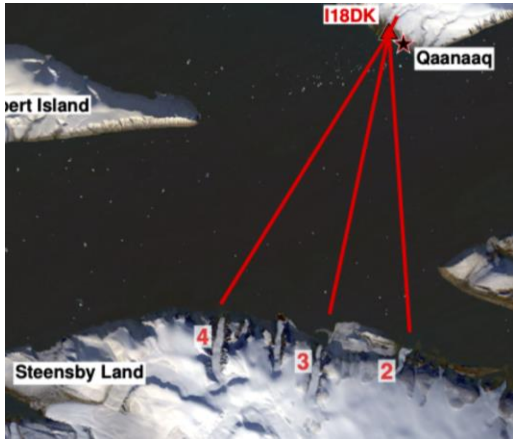

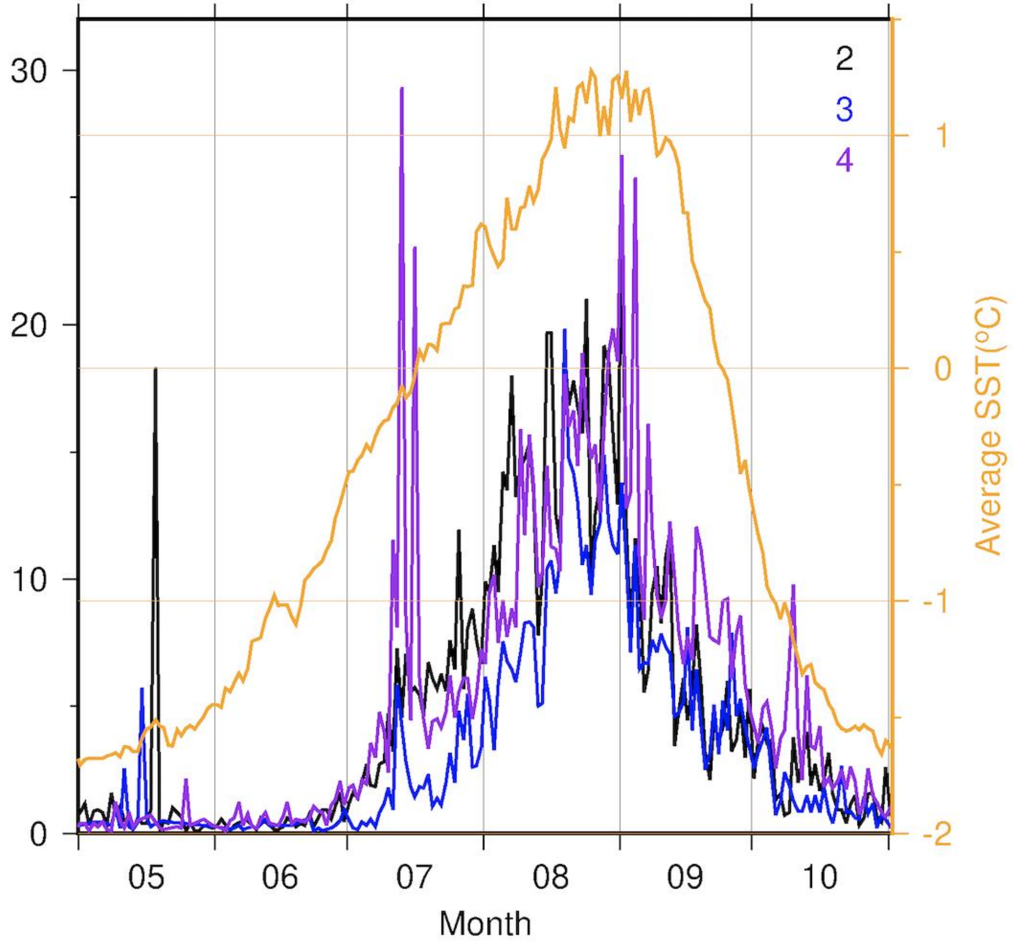

Evers et al., GRL, 2022 (in review)

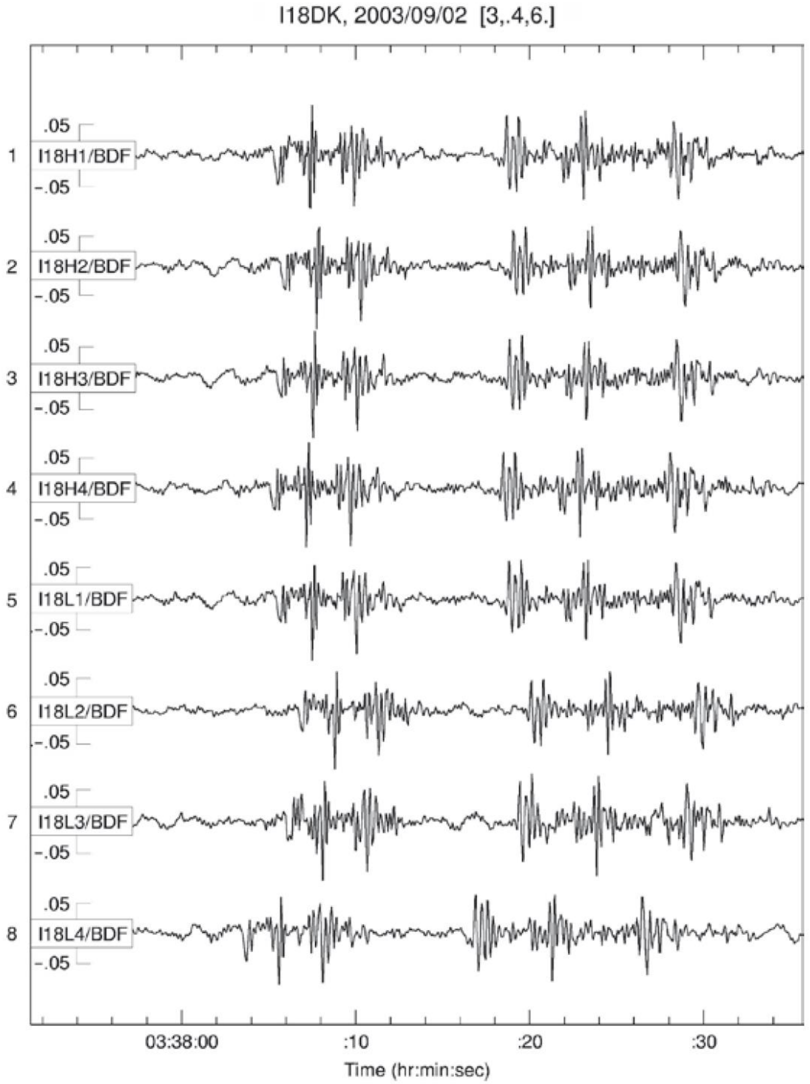

Campus & Christie, 2009

Arctic landslides in a warming climate

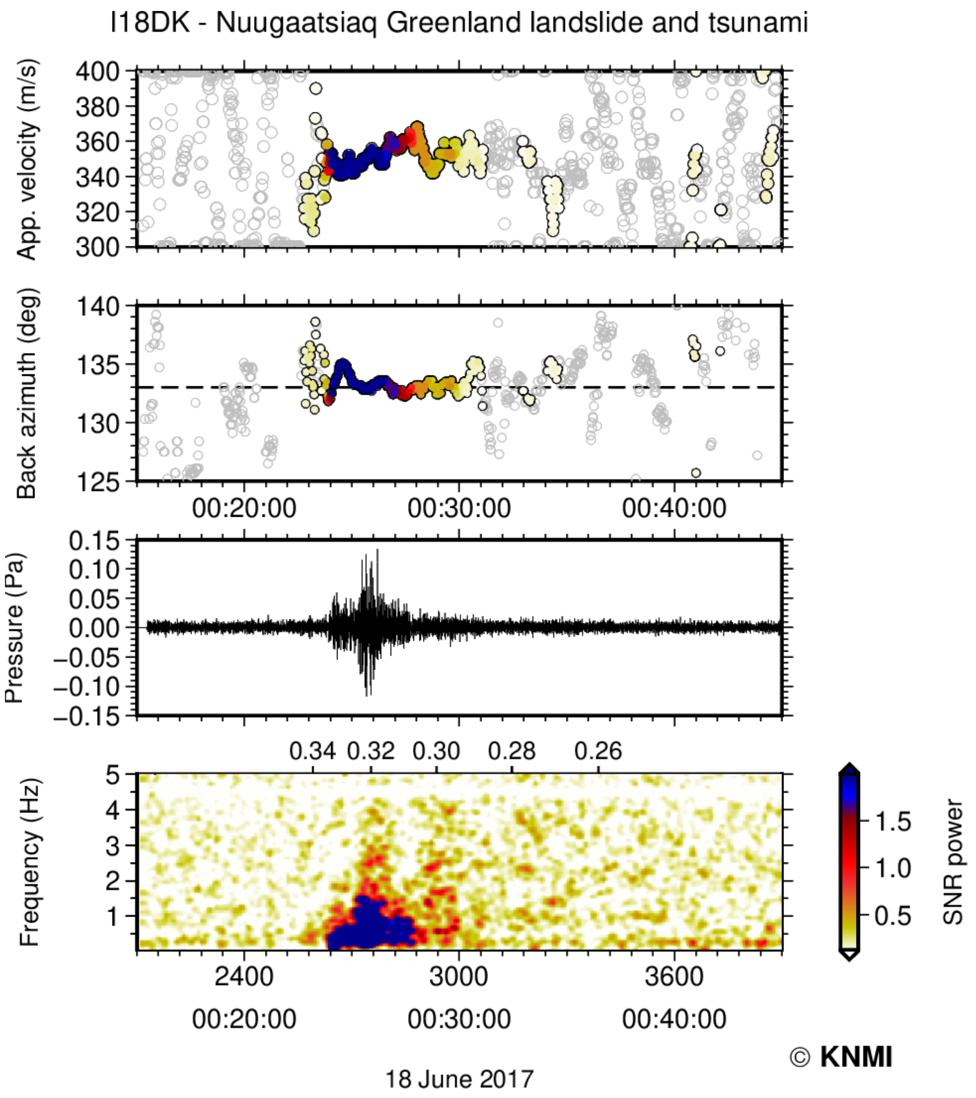

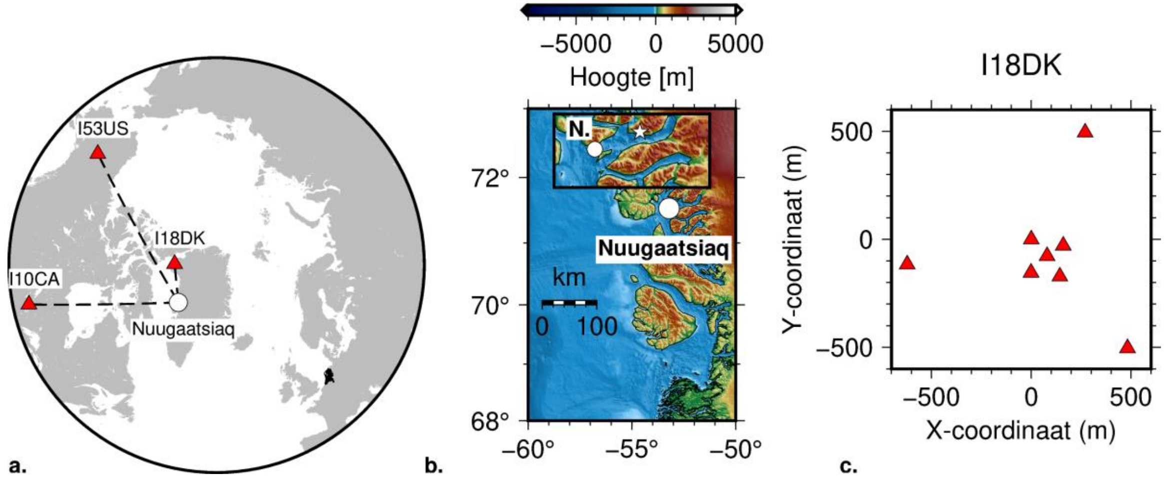

- A 100-m tall tsunami wave was triggered by a massive landslide in June 2017
- Seismo-acoustic measurements can help in understanding the landslide dynamics

Vincent van Gogh - Fishing in Spring, the Pont de Clichy (Asnières) (1887)

Linking wind and temperature to infrasound

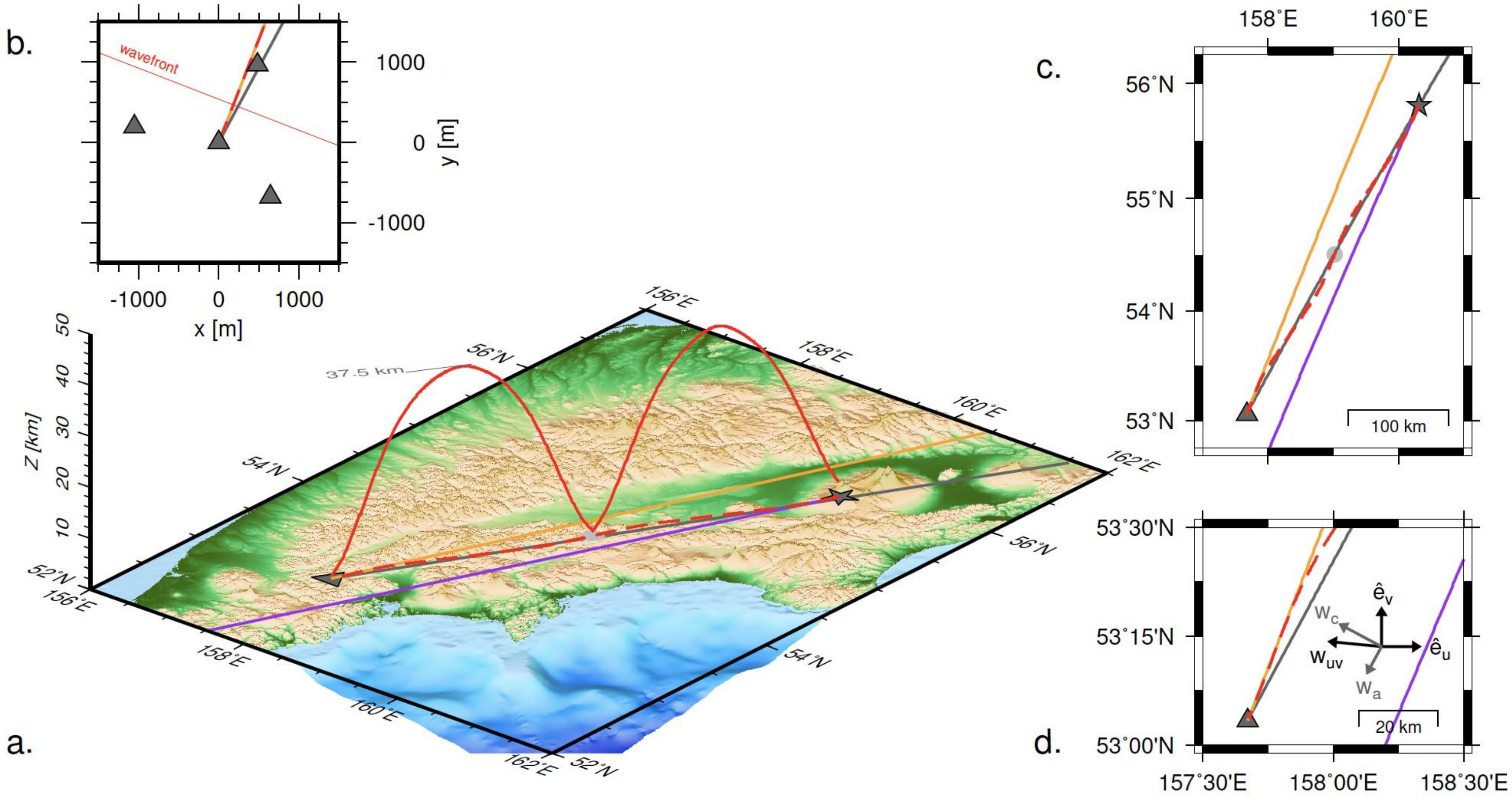

A set of infrasound observables exist that is sensitive to temperature and wind:

- Bearing deviation is determined by cross-track wind
- Trace velocity and traveltime: by temperature and along-track wind
- These quantities can be modeled with ray theory

Smets, Assink et al., JGR, 2016

Linking wind and temperature to infrasound

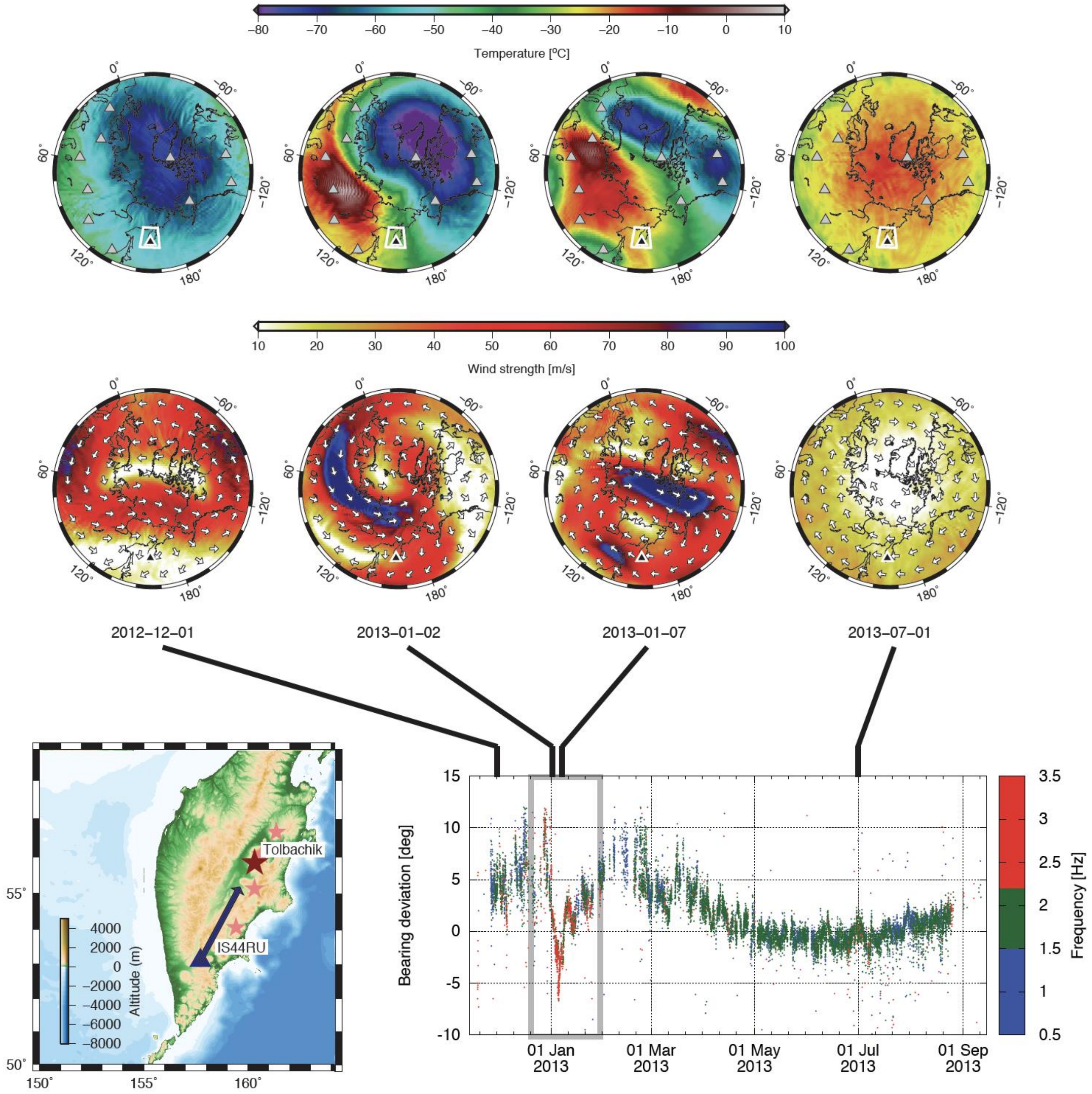

Smets, Assink et al., JGR, 2016

Bearing deviation - cross-track wind

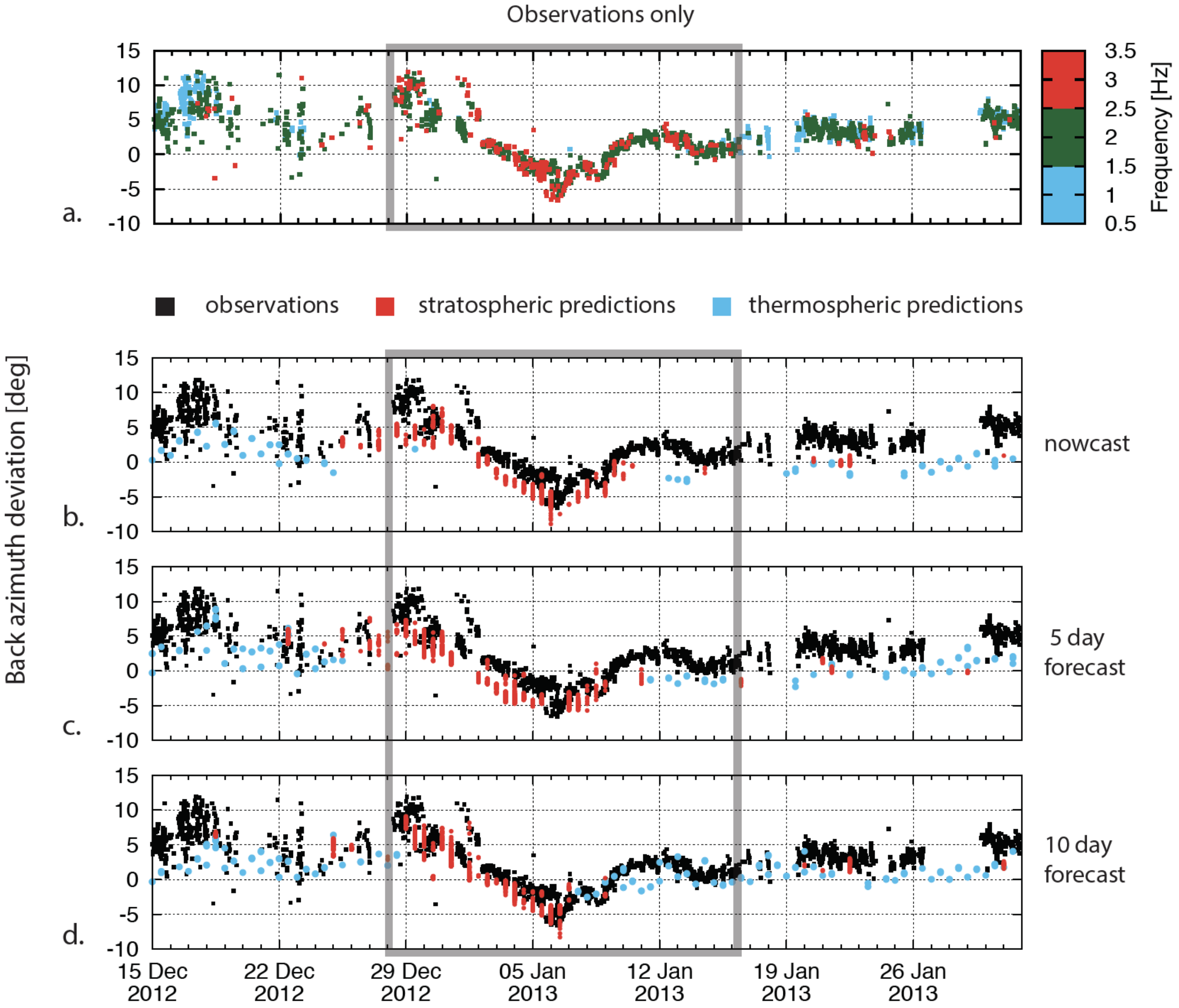

- Higher frequency and negative bearing deviation are indicator of SSW
- Differences between predicted SSW onset and recovery
- 10 day forecast skill drops when SSW observations are assimilated

Smets, Assink et al., JGR, 2016

Linking wind and temperature to infrasound

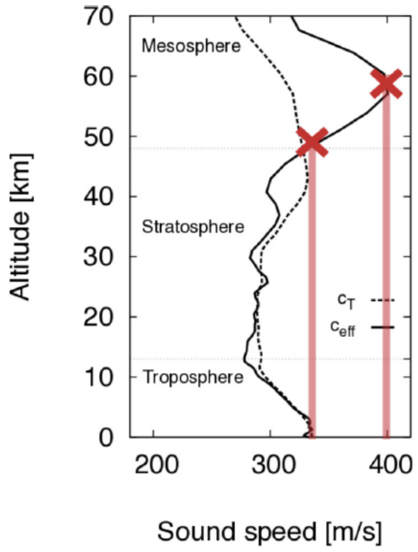

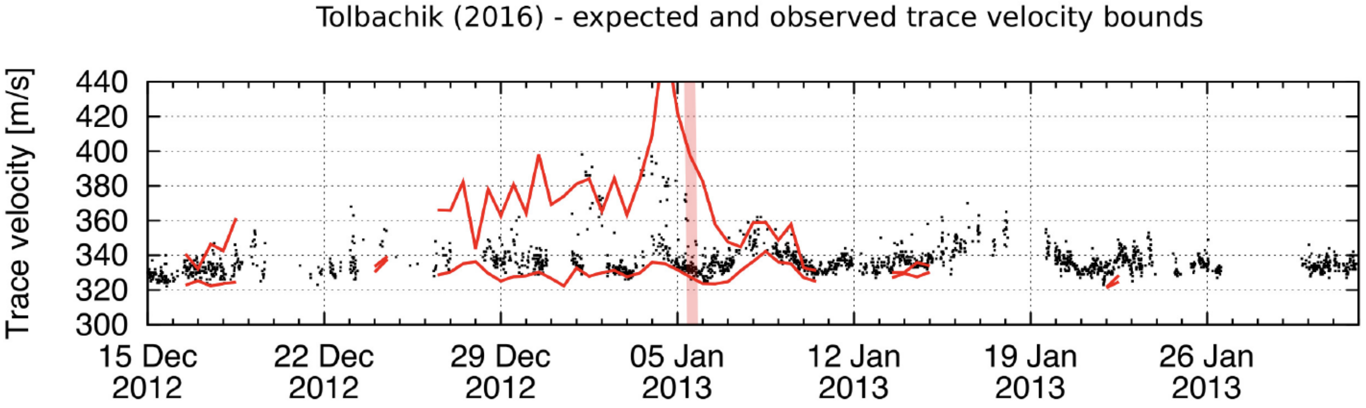

A set of infrasound observables exist that is sensitive to temperature and wind:

- Bearing deviation is determined by cross-track wind
- Trace velocity and traveltime: by temperature and along-track wind
- These quantities can be modeled with ray theory

Relevant atmospheric dynamics

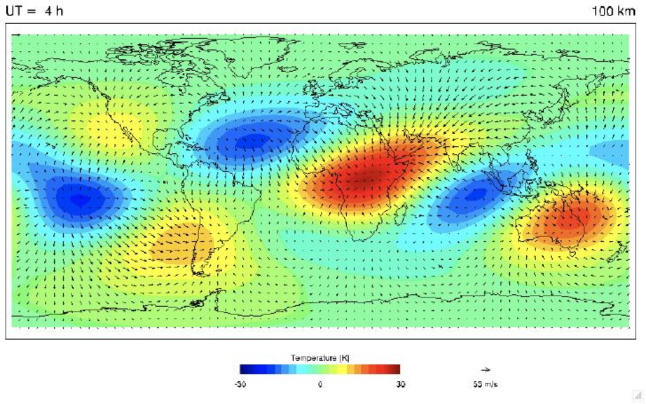

Atmospheric tides

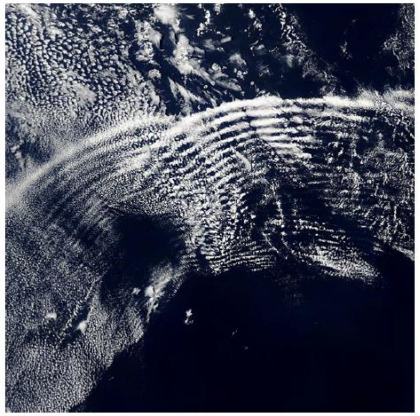

Gravity (buoyancy) waves

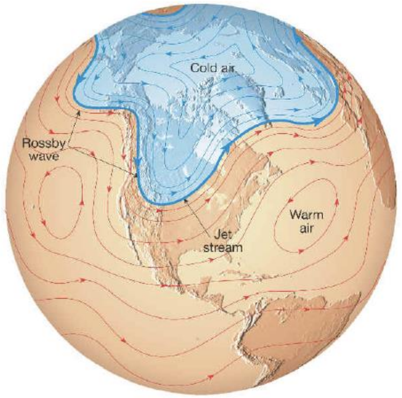

Planetary waves

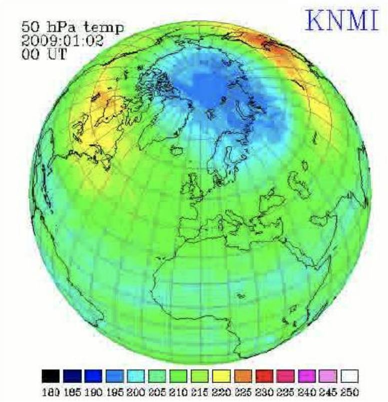

Sudden Stratospheric Warmings (SSWs)

Acoustic remote sensing in Ecuador: Tungurahua volcano

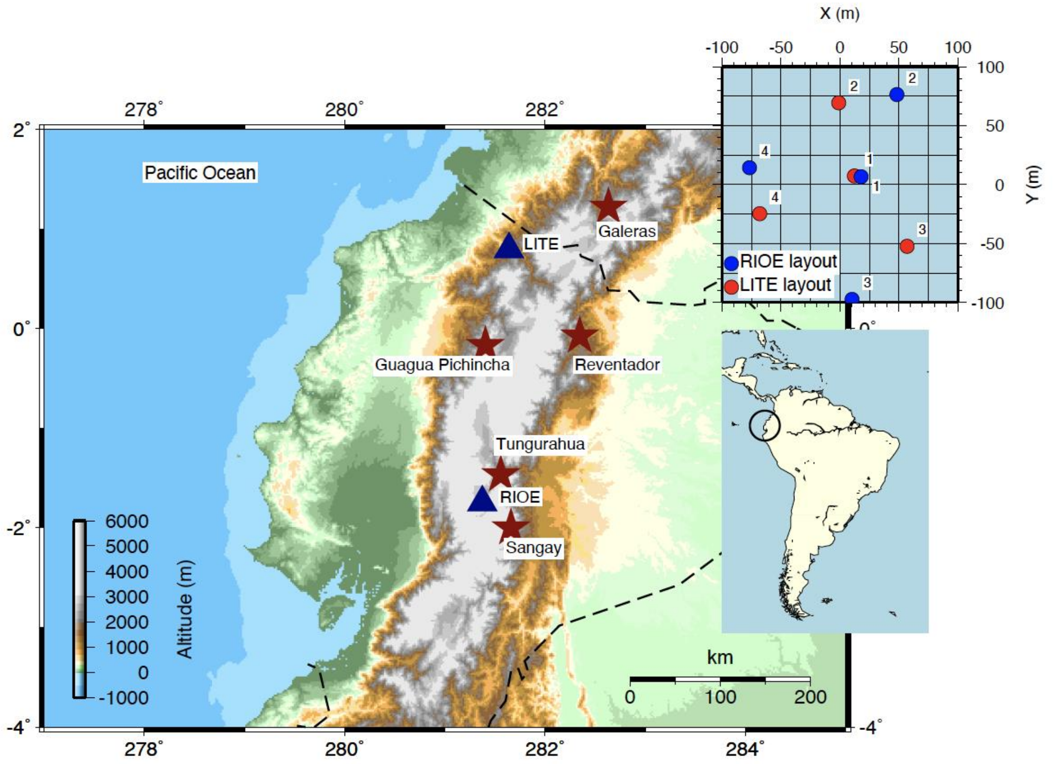

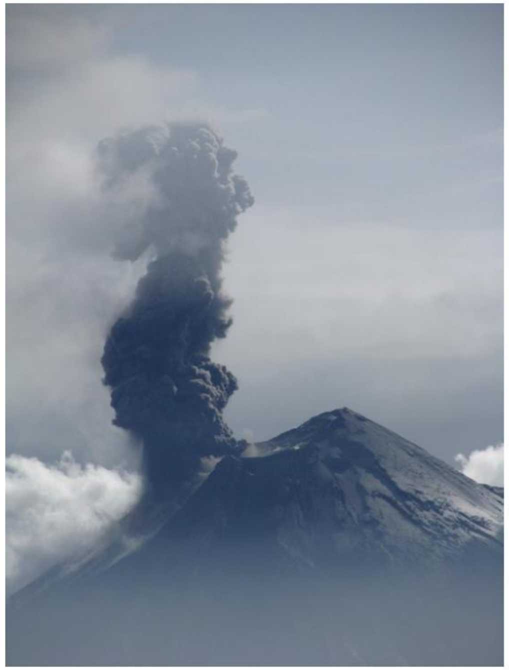

Use of Acoustic Surveillance for Hazardous Eruptions (ASHE) arrays
Study eruptions from Tungurahua volcano
Distances: 37 km (RIOE) and 251 km (LITE)

Tungurahua is an useful source: powerful, isolated low frequency transients

Assink et al., 2012, JGR-Atmospheres

Acoustic remote sensing in Ecuador: Tungurahua volcano

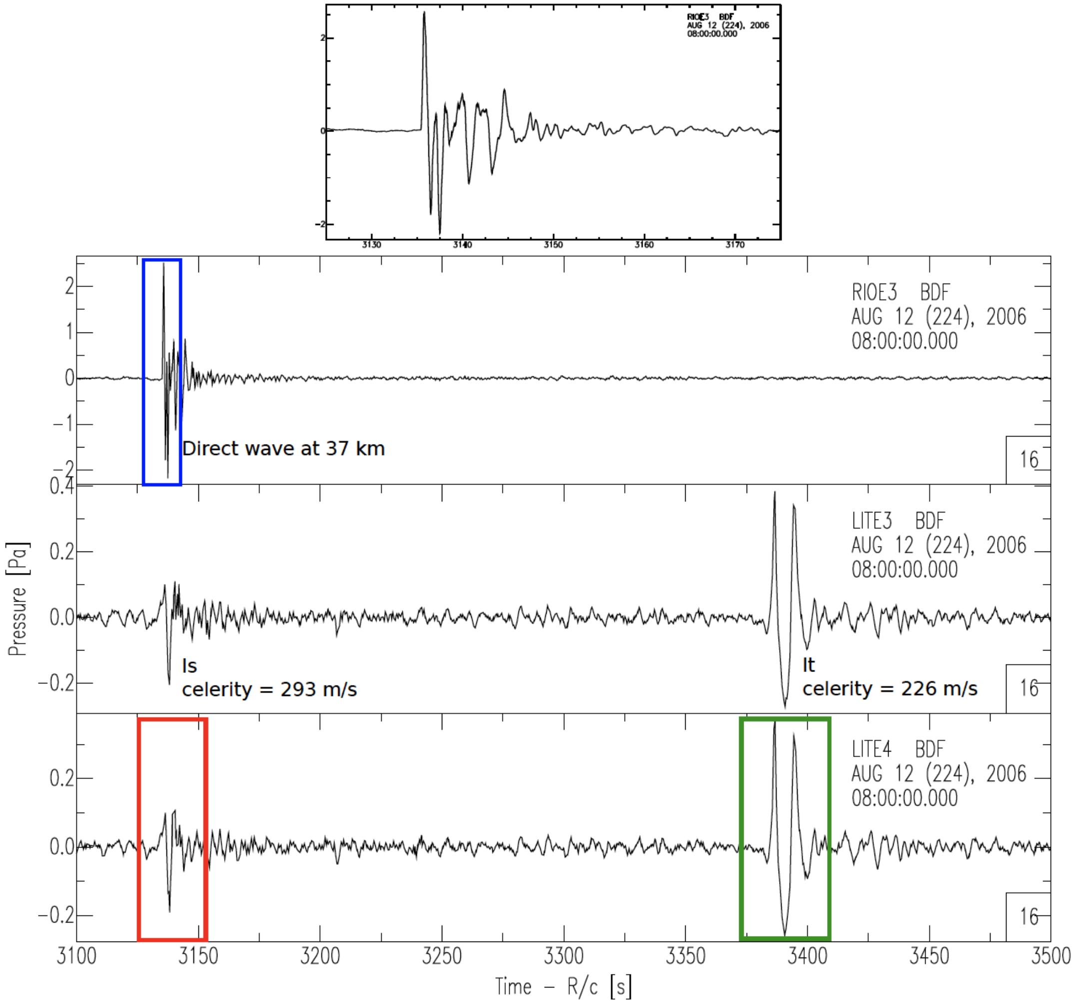

For many explosions, stratospherically and thermospherically ducted signals observed at 250 km distance.

Assink et al., 2012, JGR-Atmospheres

Acoustic remote sensing in Ecuador: Tungurahua volcano

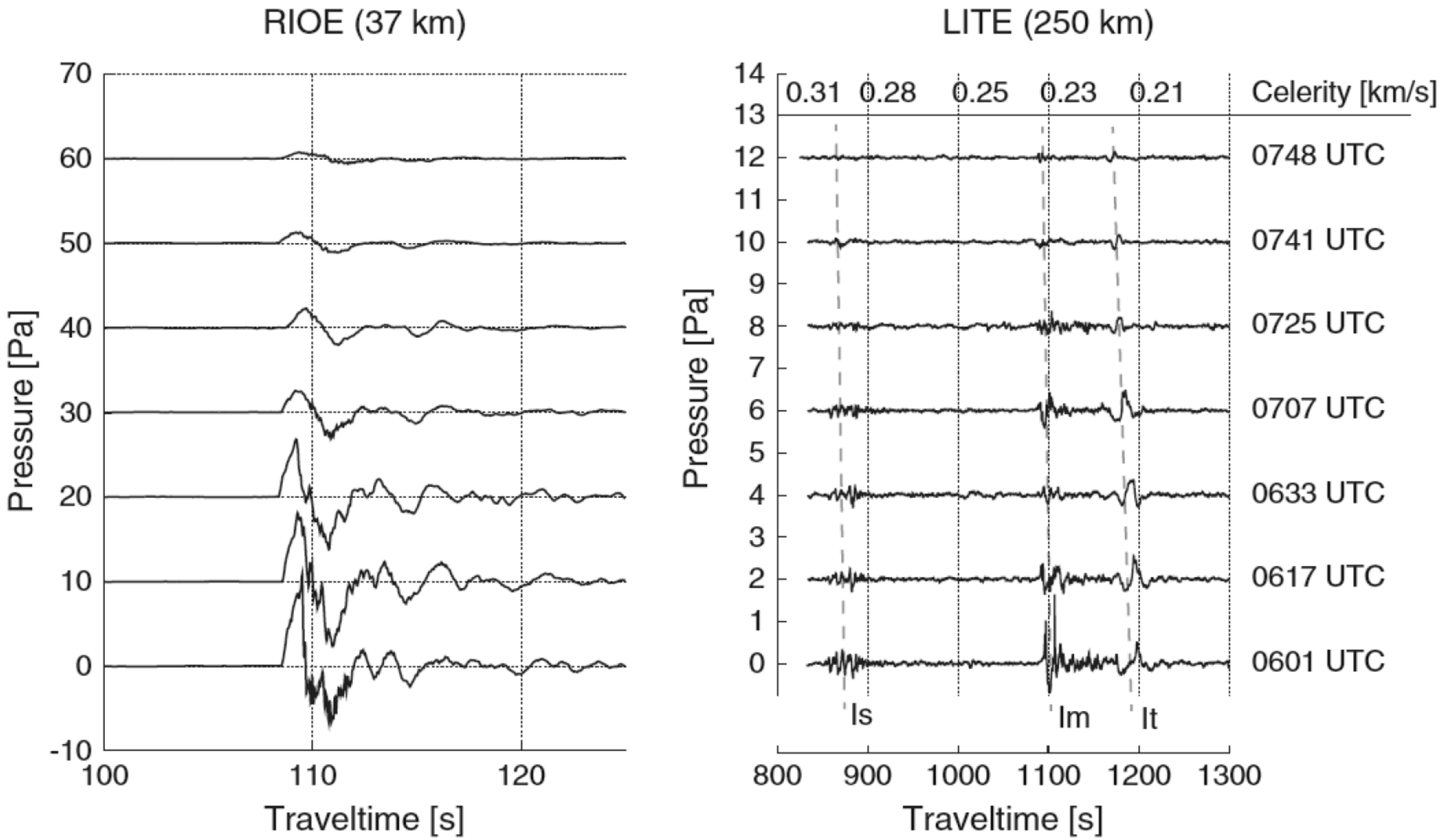

- Comparison of near & far field arrivals from Tungurahua volcano, Ecuador
- Sequence of 7 strato / meso / thermospheric arrivals within 2 hours time
- Sensitivity to large (tides) and small scale (gravity waves) perturbations
- Typical atmospheric specifications do not explain observations

Assink et al., 2013, JGR-Atmospheres

Acoustic remote sensing in Ecuador: Tungurahua volcano

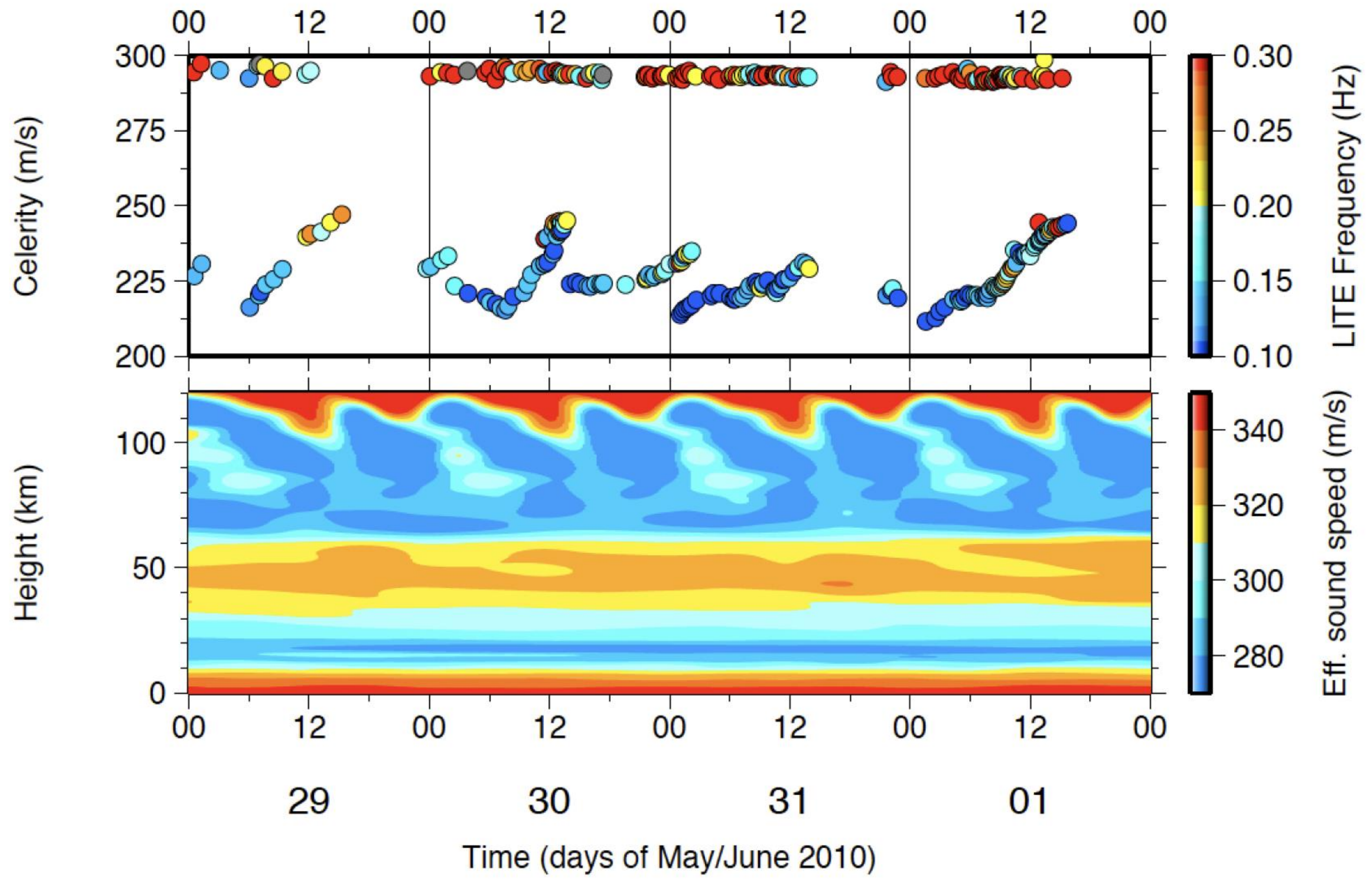

Misfit in travel time predictions and observations:

- (Near) constant stratospheric traveltime
- Diurnal variations of thermospheric travel time fluctuations
- Qualitative agreement with climatology (MSIS/HWM) at best

Inversion for large-scale atmospheric features

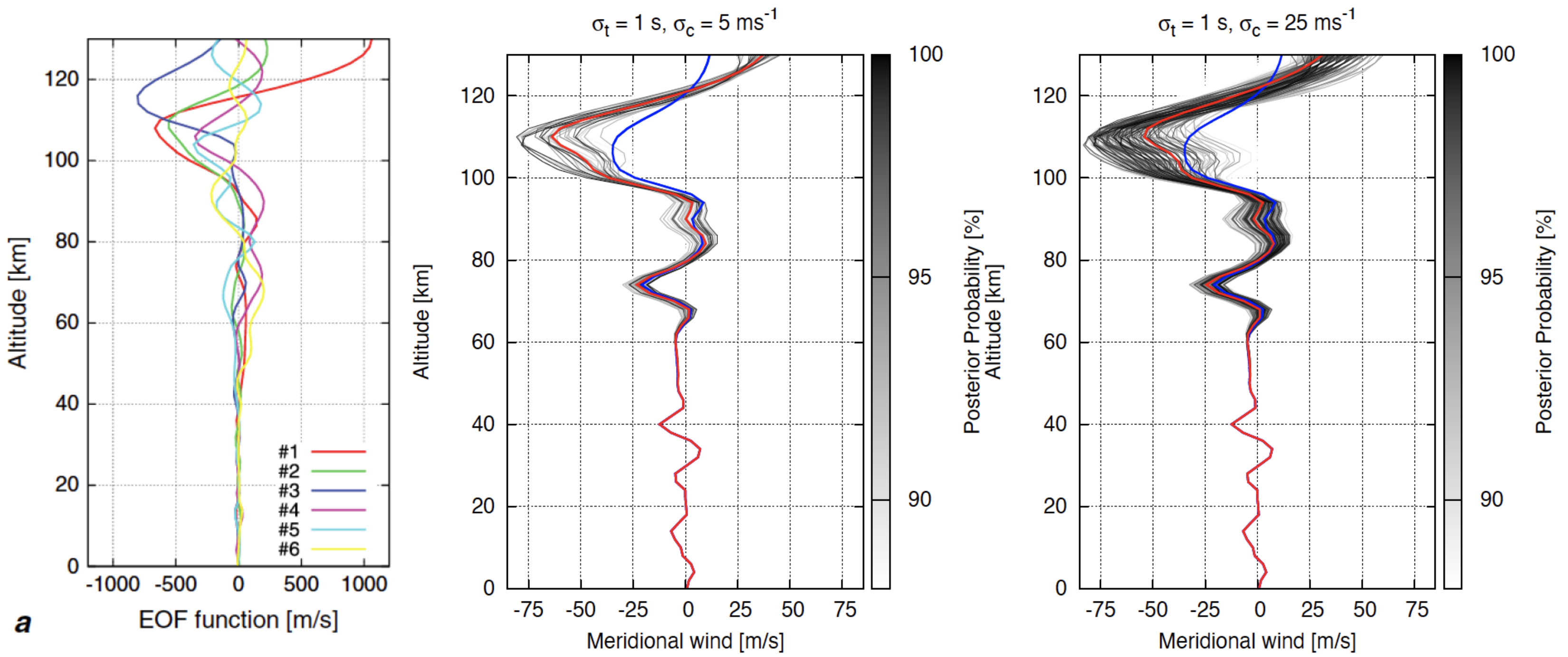

- A Bayesian approach is used to compute a posterior model $\sigma(\mathbf{m}|\mathbf{d}_{\text{obs.}})$ from likelihood L of a model and a priori likelihood ρ of the model $\mathbf{m}$
- Use of empirical orthogonal functions to parameterize wind profiles $\mathbf{m}$.
- Use of ray theory to compute eigenrays, leading to L.

$$\sigma(\mathbf{m}|\mathbf{d}_{\text{obs.}}) \propto \rho(\mathbf{m})\; L(\mathbf{m},\mathbf{d}) \tag{1}$$

- Formulation allows for incorporation of both model and data uncertainties

Assink et al., 2013, JGR-Atmospheres

Forward modeling using a updated profile

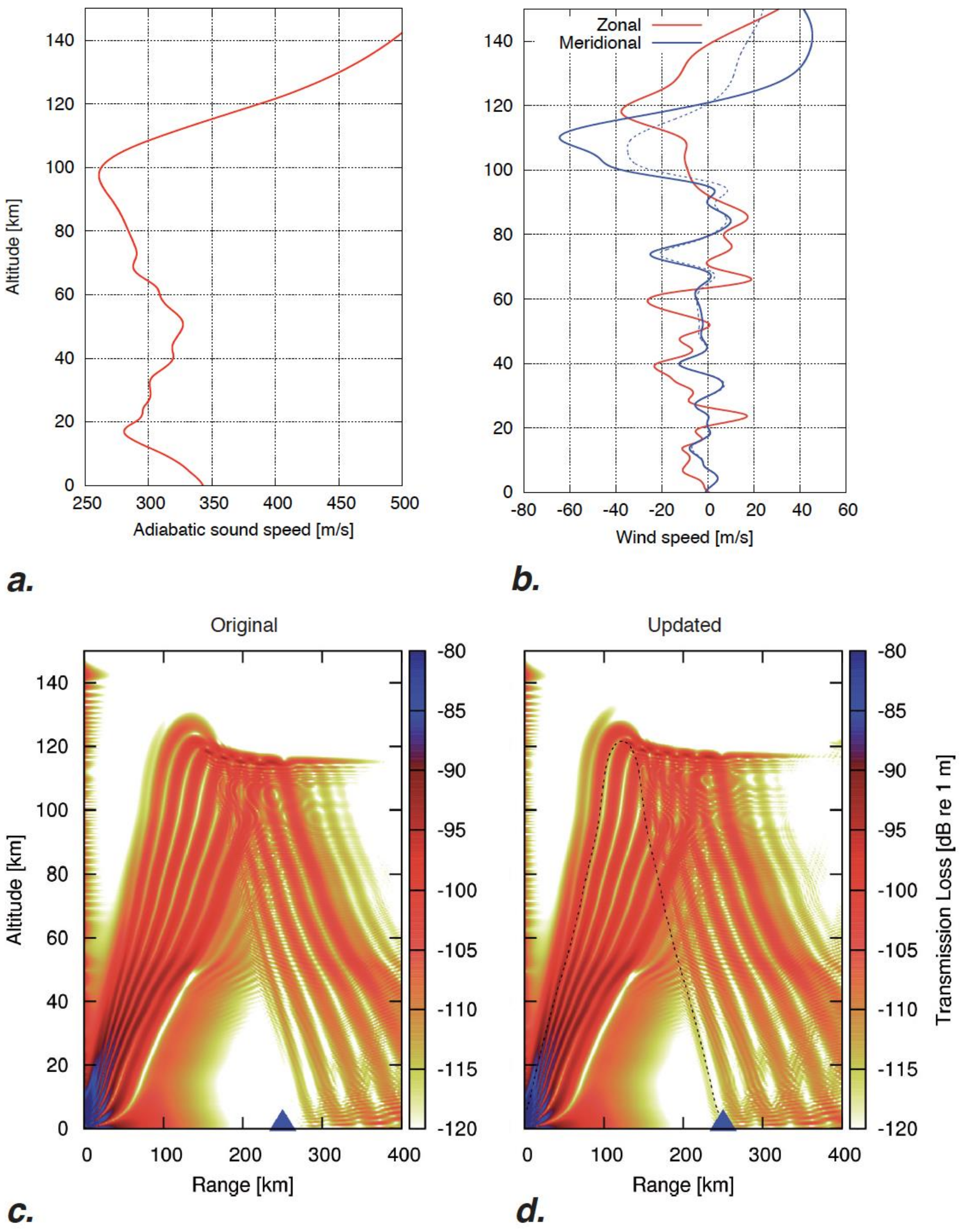

The updated profile is obtained using a 4-parameter search for the meridional winds, assuming a 5 ms^{-1} uncertainty in trace velocity and a 1 s uncertainty in travel time.

Application of non-linear raytracing to the updated profile

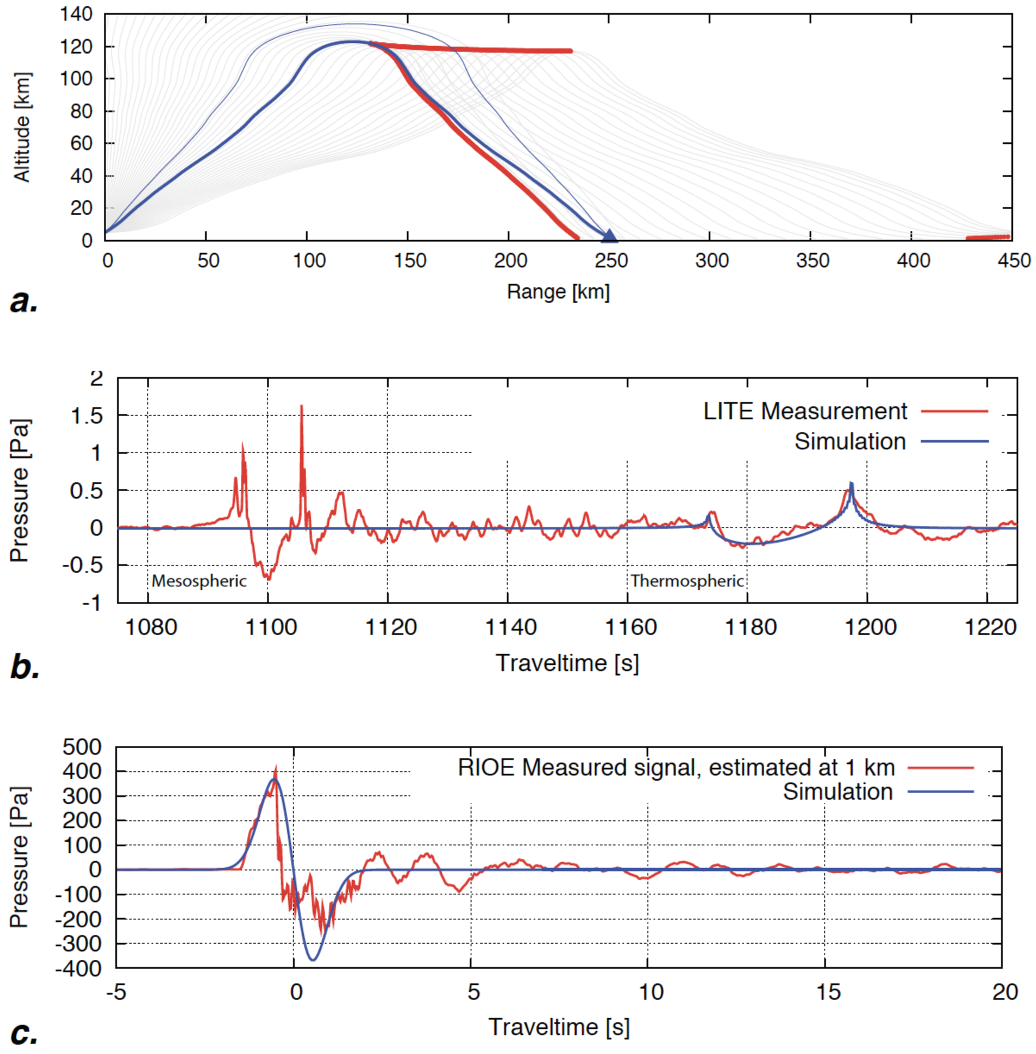

A non-linear ray tracing routine *(Lonzaga et al., 2012)* is used to model the thermospheric waveform between 1170 and 1200 seconds.

The associated prediction at 1 km corresponds reasonably with the signal at RIOE (37 km), corrected for spherical spreading

Note that the eigenray crosses a caustic of the 2nd order (180° phase shift)

Excellent agreement between simulations and observations

Inversion for small-scale atmospheric features

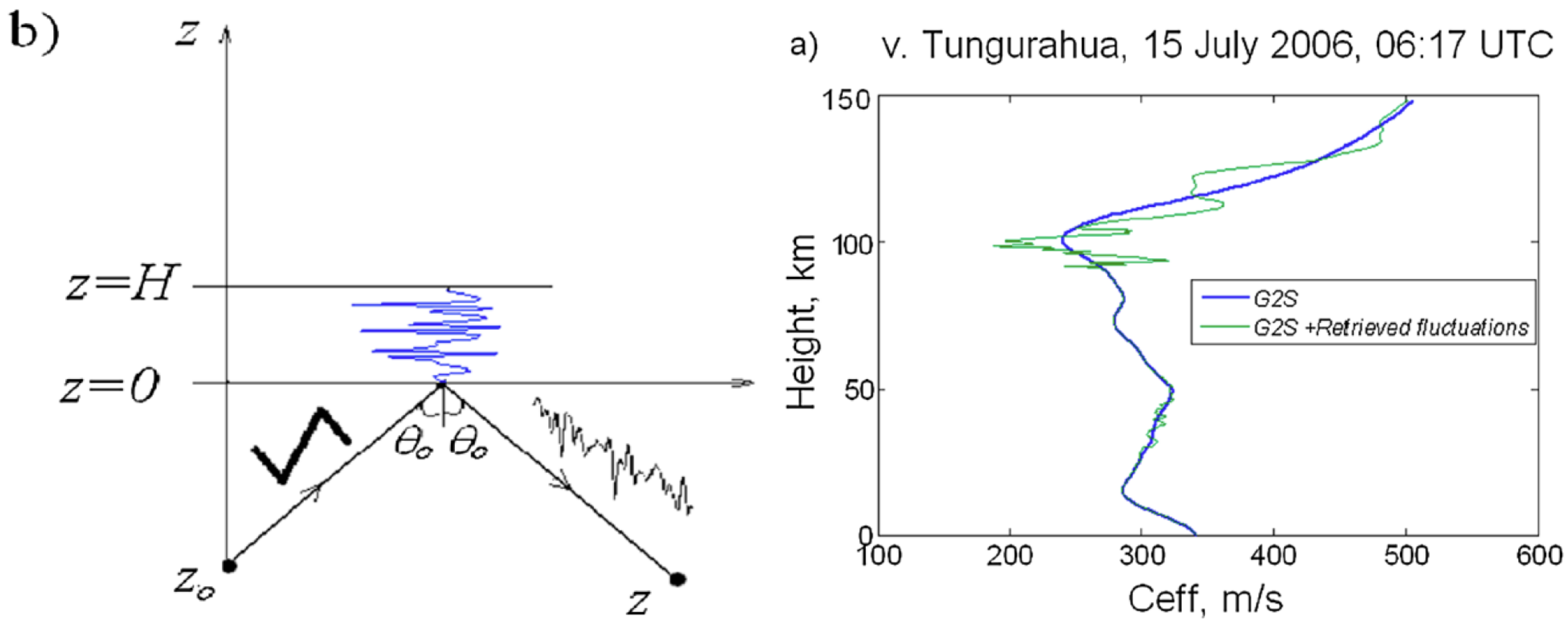

Technique to estimate atmospheric small-scale structure from scattering

Potential to use results to constrain large-scale gravity wave parameterizations

Chunchuzov, Kulichkov et al., 2015, JGR-Atmospheres

Inversion for small-scale atmospheric features

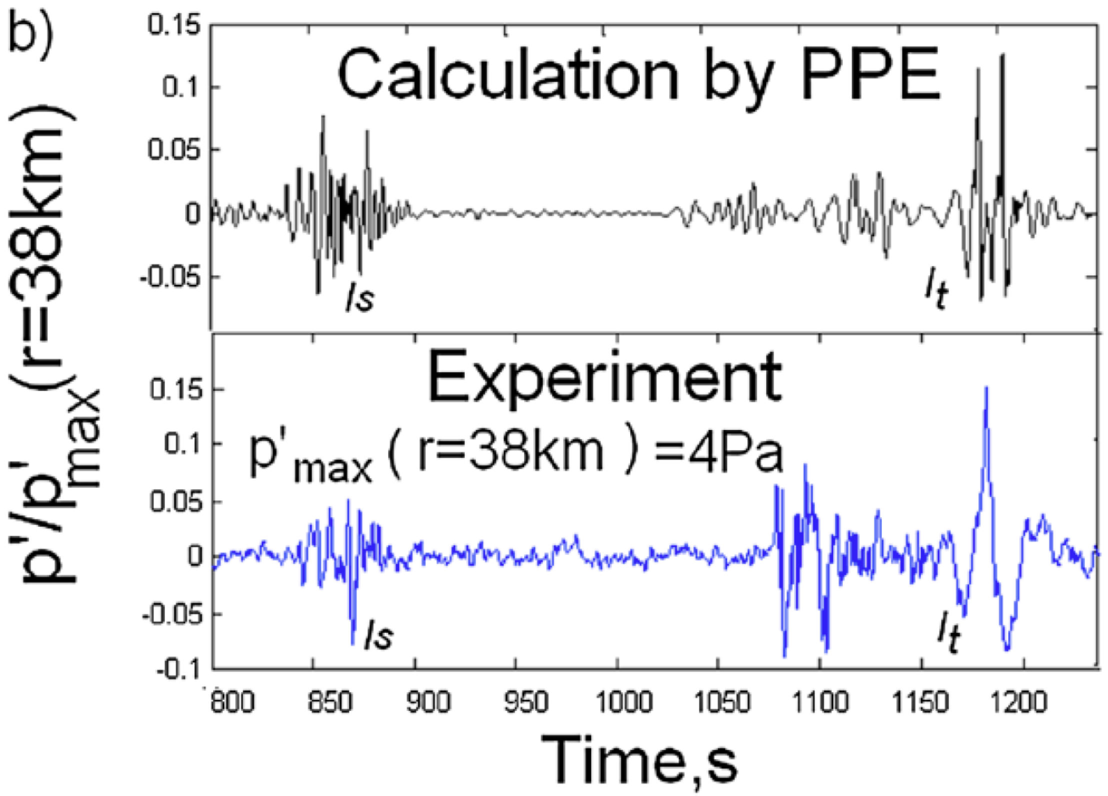

Technique to estimate atmospheric small-scale structure from scattering

Potential to use results to constrain large-scale gravity wave parameterizations

Chunchuzov, Kulichkov et al., 2015, JGR-Atmospheres